

Optimierung elektrochemischer Verfahren für die Herstellung von f-Element Dünnschichten für kernchemische Anwendungen

Dissertation

zur Erlangung des Grades
„Doktor der Naturwissenschaften“
im Promotionsfach Chemie
am Fachbereich Chemie, Pharmazie und Geowissenschaften
der Johannes Gutenberg-Universität
in Mainz

Ernst Artes
geb. in Kustanai, Kasachstan

JOHANNES GUTENBERG
UNIVERSITÄT MAINZ



Mainz, den 09. Februar 2026

1. Gutachter: Univ.-Prof. Dr. Christoph E. Düllmann
2. Gutachter: Univ.-Prof. Dr. Michael Block

Tag der mündlichen Prüfung: 24. April 2026

Ernst Artes
Department Chemie - Standort TRIGA
Fritz-Strassmann-Weg 2
55128 Mainz
erartes@uni-mainz.de

Diese Publikation ist unter der Lizenz Creative Commons Attribution-NoDerivatives 4.0 International (CC BY-ND 4.0) veröffentlicht. Das Urheberrecht liegt für die Publikation mit dem Titel "Influence of carbon dioxide and water concentration on terbium thin films produced by Molecular Plating" bei De Gruyter.

This publication is published under the Creative Commons Attribution-NoDerivatives 4.0 International (CC BY-ND 4.0) license. The copyright for the publication titled "Influence of carbon dioxide and water concentration on terbium thin films produced by Molecular Plating" is held by De Gruyter.

Declaration of academic integrity

I, Artes, Ernst, hereby declare that I have written the present dissertation entitled "Optimierung elektrochemischer Verfahren für die Herstellung von f-Element Dünnschichten für kernchemische Anwendungen" and have not used any sources or aids other than those specified (this also includes AI-based applications or tools). All literal or paraphrased quotations and citations are identified and referenced (this also applies to texts generated by generative AI, such as ChatGPT). I assure that I have not used any aids whose use has been explicitly excluded by the examiner. I have documented the AI tools used in the table "Nutzung von KI-Tools". By submitting this work, I assume responsibility for the entire product submitted. I am also responsible for any AI-generated content that I have included in my work. I have checked the accuracy of the (AI-generated) statements and content to the best of my knowledge and belief.

I am aware that any violation of the above points will have consequences under examination law and may, in particular, result in the doctoral thesis being graded as "failed." Enrollment may be revoked for up to two years if students cheat on examinations twice or more often (§ 69 Abs. 4 and 5 HochSchG).

Hiermit versichere ich, Artes, Ernst, dass ich die vorliegende Dissertation mit dem Titel "Optimierung elektrochemischer Verfahren für die Herstellung von f-Element Dünnschichten für kernchemische Anwendungen" selbständig verfasst und keine anderen als die angegebenen Quellen und Hilfsmittel (dazu zählen auch KI-basierte Anwendungen oder Werkzeuge) benutzt habe. Sämtliche wörtlichen oder sinngemäße Übernahmen und Zitate sind kenntlich gemacht und nachgewiesen (dies gilt auch für Texte, die durch generative KI, wie ChatGPT erzeugt wurden). Ich versichere, dass ich keine Hilfsmittel verwendet habe, deren Nutzung die Prüferin oder der Prüfer explizit ausgeschlossen hat.

In der Tabelle "Nutzung KI-Tools" habe ich die verwendeten KI-Tools dokumentiert.

Mit Abgabe der vorliegenden Leistung übernehme ich die Verantwortung für das eingereichte Gesamtprodukt. Ich verantworte damit auch jegliche KI-generierten Inhalte, die ich in meine Arbeit übernommen habe. Die Richtigkeit übernommener (KI-generierter) Aussagen und Inhalte habe ich nach bestem Wissen und Gewissen geprüft.

Mir ist bekannt, dass ein Verstoß gegen die genannten Punkte prüfungsrechtliche Konsequenzen hat und insbesondere dazu führen kann, dass die Promotionsleistung als mit "nicht bestanden" bewertet wird. Die Einschreibung kann für bis zu zwei Jahre widerrufen werden, wenn Studierende zweimal oder häufiger bei Prüfungsleistungen täuschen (§ 69 Abs. 4 und 5 HochSchG).

Table 1: Nutzung von KI-Tools

KI-Tool	Genutzt für	Warum	Wann
DeepL Translate	Übersetzung einzelner Ausdrücke ins Englische	Verbesserung des Ausdrucks	Beim Schreiben der Dissertation
ChatGPT	Präzisieren der selbstgeschriebenen Texte	Verbesserung der Lesbarkeit des eigenen Textes	Beim Schreiben der Dissertation

Worms, den 09.02.2026

Abstract

Zur Herstellung superschwerer Elemente werden Teilchenbeschleuniger eingesetzt, die schwere Ionen auf hohe Energien bringen und diese als Projektile auf sogenannte Targets richten. Diese Targets bestehen typischerweise aus Actiniddünnschichten. Die am häufigsten verwendete Methode zur Herstellung dieser Dünnschichten ist das sogenannte Molecular Plating (MP), ein elektrochemisches Verfahren zur Abscheidung von verschiedenen Elementen. Diese Technik wurde bereits 1963 von Parker und Falk eingeführt und ist somit über 60 Jahre alt. Trotz ihrer langen Anwendungsgeschichte ist der physikalisch-chemische Mechanismus hinter der Methode noch nicht vollständig verstanden.

In den letzten Jahrzehnten lag der Schwerpunkt bei der Charakterisierung der auf diese Weise hergestellten Dünnschichten vorwiegend auf optische Untersuchungen der Oberfläche und der Morphologie. In jüngerer Zeit verlagerte sich der Fokus jedoch zunehmend auf spektroskopische Untersuchungen, um ein tieferes Verständnis der chemischen Struktur der abgeschiedenen Schichten zu gewinnen.

Die Dünnschichten sollten für die Herstellung von superschweren Elementen möglichst wenig Fremdatome haben, um Nebenreaktionen möglichst zu vermeiden und eine hohe Stabilität aufweisen, damit diese nicht durch den Ionenstrahl zerstört werden.

Durch die zunehmende Leistungsfähigkeit moderner Teilchenbeschleuniger steigen auch die Anforderungen an die Stabilität der Targets. Die mittels MP hergestellten Targets stoßen hierbei an ihre Belastungsgrenzen, da die Teilchenbeschleuniger mit der Zeit immer leistungsfähiger werden und somit höhere Ionenströme liefern können. Darüber hinaus zeigen Simulationen, dass eine Erhöhung der Schichtdicke zu einer verbesserten Produktionsrate superschwerer Elemente führen kann. Diese Schichtdicken konnten jedoch nicht mit der Molecular Plating Technik erfolgreich hergestellt werden. Das führt zu einer Limitation der Produktionsrate durch die Dicke der Targets.

Daher ist es von zentraler Bedeutung, den Abscheidungsprozess von der Molecular Plating Methode sowie die dabei entstehenden chemischen Spezies besser zu verstehen. Auf Grundlage dieser Erkenntnisse können bisherige Methoden verbessert und Neue entwickelt werden, um stabilere und dickere Dünnschichten herzustellen.

Ziel dieser Arbeit ist es, das Verständnis des Molecular Plating-Prozesses zu vertiefen und auf dieser Basis die elektrochemische Abscheidung von f-Elementen

gezielt zu optimieren. Dabei werden moderne elektrochemische Methoden genutzt, um die Herstellung robusterer und dickerer Schichten zu ermöglichen. Die so erzeugten Dünnschichten werden spektroskopisch untersucht und als Targets in Ionenstrahlexperimenten getestet. Hierbei werden die Targets unterschiedlichen Ionenarten und Strahldosen ausgesetzt, um mögliche chemische Veränderungen infolge der Bestrahlung zu analysieren. Lanthanide wie Terbium und Thulium werden als Modelle für Actinide eingesetzt, da sie als leichtere Homologe ähnliche chemische Eigenschaften wie Americium und Curium aufweisen.

To synthesize superheavy elements, particle accelerators are used to accelerate heavy ions and direct them onto targets. These targets are typically composed of thin films made from actinide materials. The most commonly used method for producing these thin films is known as Molecular Plating (MP), an electrochemical deposition technique for various elements. This method was introduced in 1963 by Parker and Falk and has been in use for over 60 years. Despite its long history, the physicochemical mechanism of Molecular Plating is still not fully understood.

For many years, the characterization of the resulting thin films focused primarily on their morphological properties. However, in recent years, the focus has shifted toward spectroscopic studies to gain deeper insights into the chemical composition of the deposited films.

For the production of superheavy elements, the thin films should contain as few impurities as possible to minimize side reactions and should exhibit high stability to withstand the ion beam without being destroyed.

With the increasing power of modern particle accelerators, the demands on target stability have risen. Targets produced via MP are reaching their physical and chemical limits, as particle accelerators are becoming increasingly powerful over time and can therefore deliver higher ion currents. Moreover, the achievable film thickness with MP is inherently limited. Current simulations suggest that thicker films could significantly increase the production rate of superheavy elements — a goal that cannot be achieved using traditional MP techniques alone.

Therefore, a deeper understanding of the Molecular Plating process and the chemical species formed during deposition is essential. This knowledge is critical for developing more stable and thicker thin films.

The aim of this work is to advance the understanding of the Molecular Plating process and to improve the electrochemical deposition of f-elements based on these insights. Modern electrochemical techniques are employed to enable the fabrication of thicker and more stable thin films. These newly developed films are characterized using spectroscopic methods and tested as targets in ion beam experiments. In these tests, the targets are exposed to different ion species and beam doses to investigate possible chemical changes induced by irradiation. Lanthanides such as terbium and thulium are used as model systems for actinides, as they share similar chemical properties with actinides like americium and curium due to their homologous nature.

Contributions

This thesis is based on four publications, which are listed below. The author is the main author of three publications [1,2,4]. Furthermore, the author provided major contributions to the publication [3] in the form of method development, target production, target characterization, and active coauthor of the text block in Section II of the publication.

Publications

- [1] E. Artes, et al., The process of molecular plating and the characteristics of the produced thin films – What we have learned in 60 years and what is still unknown, EPJ Web of Conferences (2023) 03001.
- [2] E. Artes, et al., Influence of carbon dioxide and water concentration on terbium thin films produced by Molecular Plating, *Radiochimica Acta*, 113, 2025, pp. 779-789.
- [3] C.-C. Meyer, et al., Microscopic and spectroscopic analysis of ion-irradiated molecular-plated thin films for superheavy element production, *Nuclear Instruments and Methods in Physics Research Section A: Accelerators, Spectrometers, Detectors and Associated Equipment* (2025) 170361.
- [4] E. Artes, et al., Preparation of lanthanide thin films for ion beam experiments and post irradiation characterization, *Nuclear Instruments and Methods in Physics Research Section A: Accelerators, Spectrometers, Detectors and Associated Equipment* (2025) 170403.

Contents

Declaration of academic integrity	iii
Abstract	v
Contributions	ix
Contents	xi
1 Introduction	1
1.1 Scientific Background on Superheavy Elements	2
1.2 Production techniques for SHE	5
1.3 Targets for SHE production	7
1.3.1 Molecular Plating	8
1.3.2 Target geometry and substrate specifications	12
1.3.3 Ideal target thickness	14
1.3.4 Ion beam-induced changes of thin films	16
1.4 Characterization methods	19
1.4.1 Neutron activation analysis and gamma spectrometry	19
1.4.2 Scanning electron microscopy	22
1.4.3 Raman and infrared spectrometry	24
1.4.4 X-ray photoelectron spectroscopy	26
1.4.5 Ion-beam analysis	27
1.5 Outline of this work	29
1.6 References	30
2 Publication I: The process of molecular plating and the characteristics of the produced thin films – What we have learned in 60 years and what is still unknown	41
2.1 Own contributions	41
2.2 Publication	41
3 Publication II: Influence of carbon dioxide and water in production of lanthanide thin films made by molecular plating	47
3.1 Own contributions	47

3.2	Publication	47
4	Publication III: Microscopic and spectroscopic analysis of ion-irradiated molecular-plated thin films for superheavy element production	59
4.1	Own contributions	59
4.2	Publication	59
5	Publication IV: Preparation of lanthanide thin films for ion beam experiments and post irradiation characterization	75
5.1	Own contributions	75
5.2	Publication	75
6	Conclusion and Outlook	87
	List of Figures	89
	Acknowledgements	91

Chapter 1

Introduction

The aim of this thesis is to gain a deeper understanding of the mechanism behind the molecular plating technique and, based on this, to develop modern electrochemical deposition techniques for lanthanides and actinides. This new approach is intended to enable the production of thicker thin films with improved stability under ion beam irradiation compared to molecular plated thin films. Such advancements are essential for extending the usability of these films in nuclear physics applications.

The newly developed thin films are intended to be used as target materials for the production of the heaviest elements. In this context, their thickness and stability under irradiation are key factors for successful superheavy element synthesis.

This chapter provides a brief overview of the scientific background related to superheavy elements and the targets required for their production. Furthermore, the analytical techniques used in target development and their associated challenges are discussed.

1.1 Scientific Background on Superheavy Elements

The discovery of radioactivity by Henri Becquerel in 1898 laid the foundation for extensive research into nuclear phenomena [1]. A major breakthrough in this field was the discovery of nuclear fission in 1938 by Otto Hahn and Fritz Strassmann, which was later interpreted and explained by Lise Meitner and Otto Frisch in terms of physical principles. Shortly thereafter, in 1940, Edwin McMillan succeeded in synthesizing neptunium, the first transuranium element. [2, 3]

In the following years, additional transuranium elements — ranging from plutonium to fermium — were produced. Glenn T. Seaborg and Edwin McMillan were awarded the Nobel Prize in Chemistry for their identification of the actinide series as a group of heavy homologues to the lanthanides, and for correctly positioning uranium and the transuranium elements within this series [4].

Fermium (element 100) represents a critical limit in the traditional production pathway of heavier elements [4]. Up to this point, transuranium elements were typically synthesized through successive neutron capture reactions followed by β^- -decay. However, no known isotope of fermium undergoes β^- -decay to form element 101. Instead, fermium isotopes decay primarily via α -emission or spontaneous fission, effectively blocking further synthesis via neutron irradiation.

This obstacle was eventually overcome through the use of heavy-ion accelerators, which enabled the fusion of a heavy target nucleus with a lighter projectile nucleus. These fusion-evaporation reactions made it possible to synthesize elements beyond fermium, and thus extend the periodic table beyond atomic number 100. To date, this method has led to the discovery of elements up to oganesson ($Z = 118$) [5–7].

Element 104, rutherfordium, is generally regarded as the first superheavy element [8, 9]. This classification is based on its position in the periodic table: unlike the lighter transuranium elements, which are part of the actinide series, rutherfordium is assigned to group 4 of the d-block and is therefore considered a transition metal. This marks a conceptual shift in the synthesis of heavy elements, as it indicates the beginning of a new region of the periodic table beyond the actinides — the so-called superheavy element (SHE) region [8].

Superheavy elements exhibit unique nuclear and chemical properties due to the high number of protons in the nucleus [9, 10]. Their synthesis is only possible through fusion-evaporation reactions using heavy-ion accelerators. In these processes, a heavy target nucleus is bombarded with a lighter projectile ion at high kinetic energy, leading, in rare successful events, to the formation of a highly excited

compound nucleus. This nucleus may then de-excite by evaporating neutrons and form a new element.

Because the cross sections, which is indicative of the level of probability associated for the formation of superheavy elements, are extremely low — often in the picobarn or even femtobarn range (Figure 1.1) — only a few atoms of a given SHE can be produced, even during extended beam times. Furthermore, the resulting nuclei are typically highly unstable and decay within milliseconds to seconds via α -decay or spontaneous fission.

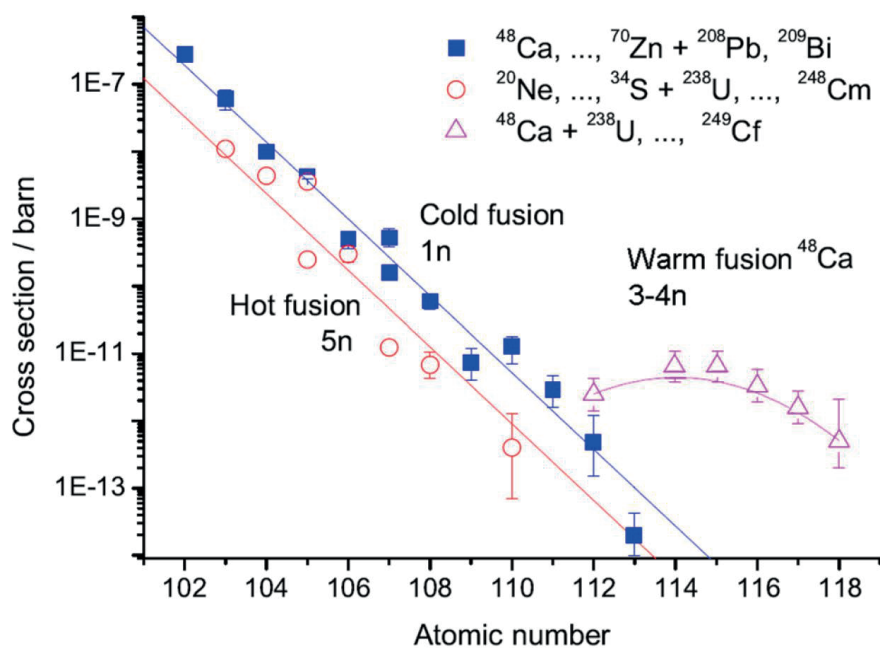


Figure 1.1: The cross section for the production of superheavy elements via different fusion routes [11]. The blue squares show the cold fusion reaction, the red circles the hot fusion reactions and the pink triangles the warm fusion reaction with ^{48}Ca as an ion beam and actinides as targets. The different production techniques for SHE are further explained in chapter 1.2

The stability of superheavy nuclei strongly depends on their neutron number, as additional neutrons enhance the nuclear binding via the strong force and help counteract the intense Coulomb repulsion between the many protons. Neutron-rich isotopes are therefore expected to be longer-lived and possibly approach the predicted “island of stability” (Figure 1.2). The island of stability is a term used to describe a region in the nuclide chart where isotopes have a significantly longer half-life than the surrounding isotopes. However, all currently synthesized SHE are relatively neutron-poor. This is mainly because the reactions used to produce

them involve stable or long-lived projectiles and targets, which inherently limit the neutron excess. Additionally, the fusion process typically results in highly excited compound nuclei that de-excite by evaporating neutrons, further reducing the final neutron number of the produced isotopes [12–15].

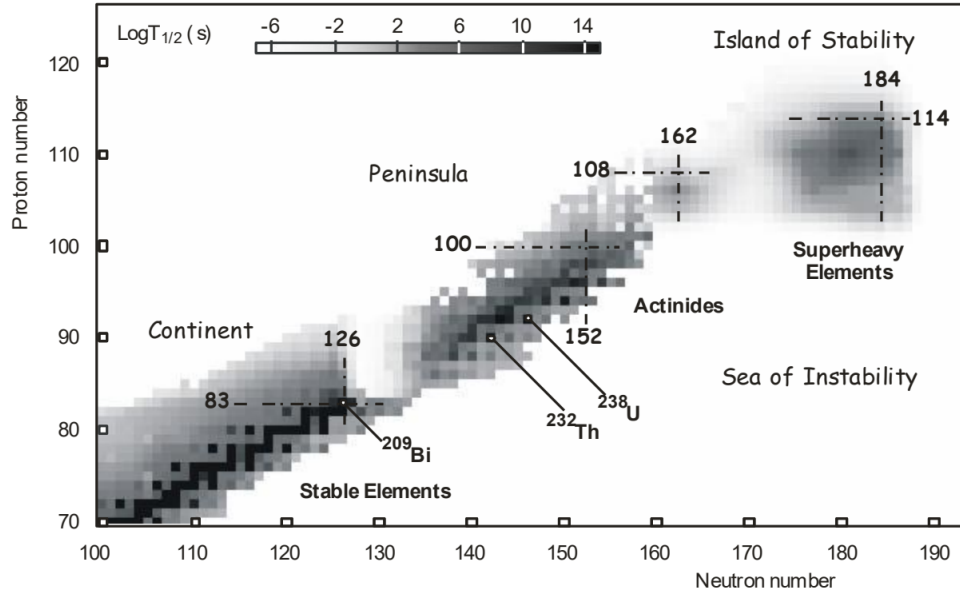


Figure 1.2: The nuclide chart with the estimated positions of the island of stability is shown there. The black boxes show stable elements. The stability of the isotopes are shown in steps of grey to white. Brighter grey tones show shorter half-lives [16].

Due to these short half-lives and the extremely low production rates, classical off-line chemical separation and analytical techniques are not feasible. Instead, all investigations — including identification, decay spectroscopy, and chemical characterization — must be performed in online experiments [9, 15, 17–19]. In these setups, the reaction products are separated from the primary beam and unwanted background in real time, typically via gas-filled recoil separators such as TASCA (Transactinide Separator and Chemistry Apparatus) at the GSI Helmholtzzentrum für Schwerionenforschung GmbH (GSI) or velocity filter such as SHIP (Separator for Heavy Ion reaction Products) at the GSI [20, 21], and are then directed to detection or chemical systems within fractions of a second.

These experimental challenges require highly efficient and selective systems for ion transport, detection, and data acquisition. As such, the production and study of superheavy elements represents a demanding and interdisciplinary field in modern nuclear science, combining aspects of nuclear physics, radiochemistry, accelerator technology, and advanced instrumentation.

1.2 Production techniques for SHE

The production of elements with atomic numbers of 101 or higher requires the use of particle accelerators [12–15]. Only accelerated ions can attain kinetic energies sufficient to overcome the Coulomb barrier of a target nucleus, enabling the two nuclei to approach closely enough for nuclear fusion to occur. However, the kinetic energy of the projectile must be carefully optimized. If it is too low, fusion cannot take place due to electrostatic repulsion. If it is too high, the resulting excitation energy may instead lead to undesired side reactions such as spallation or prompt fission of the target nucleus, preventing the formation of a compound nucleus [13, 22].

Even under optimal conditions, the probability of forming a compound nucleus is extremely low due to competing processes such as quasifission. If successful, the fusion of the two nuclei results in the formation of a compound nucleus that initially contains all protons and neutrons from both the projectile and the target. This nucleus is typically created in a highly excited state and must dissipate its excess energy in order to reach ground state. De-excitation can occur either through immediate fission or through the emission of one or more neutrons, often accompanied by gamma radiation. The number of neutrons emitted depends primarily on the excitation energy of the compound nucleus, which is determined by the choice of projectile and target as well as the kinetic energy of the collision [23, 24].

Different fusion strategies have been developed to control the excitation energy and optimize the formation and survival of superheavy nuclei. Among these, cold fusion and hot fusion represent the two most widely used approaches [23–25].

In cold fusion reactions aimed at the synthesis of superheavy elements (SHE), the compound nucleus is formed with relatively low excitation energy, typically leading to the evaporation of only a single neutron. This is shown in (Figure 1.3 a)). This low excitation energy is achieved by selecting projectile–target combinations composed of isotopes with high binding energy per nucleon.

Target elements are typically ^{208}Pb or ^{209}Bi , because they have a magic or doubly-magic nucleus. Just as electrons in an atom occupy discrete energy levels, protons and neutrons within a nucleus also have discrete energy levels. In the nuclear shell model, these quantized levels can lead to shell closures, which result in exceptionally stable nuclei. ^{209}Bi has with $Z = 83$, $N = 126$ a closed neutron shell and is a magical nucleus and ^{208}Pb has with $Z = 82$, $N = 126$ a closed proton and neutron shell and is therefore doubly-magic [26].

Suitable projectiles include medium-mass, neutron-rich, and stable isotopes such

as ^{58}Fe , ^{64}Ni , and ^{70}Zn . These combinations enhance the likelihood of forming a neutron-rich compound nucleus, which is crucial for improving the survival probability of the evaporation residue.

Hot fusion reactions involve the formation of compound nuclei with much higher excitation energies, typically requiring the evaporation of four to five neutrons to reach the ground state, which is shown in Figure 1.3 b). In these reactions, actinide elements such as uranium, plutonium, americium, curium, berkelium, or californium ($Z = 92\text{--}98$) serve as targets. Light ions such as ^{16}O , ^{20}Ne , or ^{24}Mg are used as projectiles.

Although more neutrons are lost during de-excitation, the actinide targets provide significantly higher initial neutron numbers compared to those used in cold fusion. As a result, the final evaporation residues in hot fusion are generally more neutron-rich and thus exhibit longer half-lives. This increased stability allows for more detailed investigations, including laser spectroscopy of the SHE [27, 28] or even the study of chemical properties in some cases [19, 29]. However, a major drawback of hot fusion is that the reaction cross sections for forming a given SHE are typically an order of magnitude lower than those observed in cold fusion for the same element (See Figure 1.1).

A special case is the use of ^{48}Ca with $Z = 20$ and $N = 28$ as a projectile. ^{48}Ca is a doubly magic nucleus and represents the most neutron-rich stable calcium isotope. Though its natural abundance is only about 0.2 %, it can be enriched. Enriched ^{48}Ca is used as a source and accelerated to form high-intensity ion beams. When actinide targets are irradiated with ^{48}Ca the fusion reaction is called warm fusion [30]. In the warm fusion, the compound nucleus evaporates only three to four neutrons — fewer than in hot fusion — while maintaining higher reaction cross sections (See Figure 1.1). Thus, this approach effectively combines the advantages of both cold and hot fusion. The neutron loss is reduced while maintaining an enhanced formation probabilities (See Figure 1.3 c)). The ^{48}Ca -based fusion technique has been essential in the discovery of the heaviest known elements, from flerovium ($Z = 114$) to oganesson ($Z = 118$), whose synthesis was previously unfeasible due to prohibitively low cross sections using other projectile-target combinations [30–33].

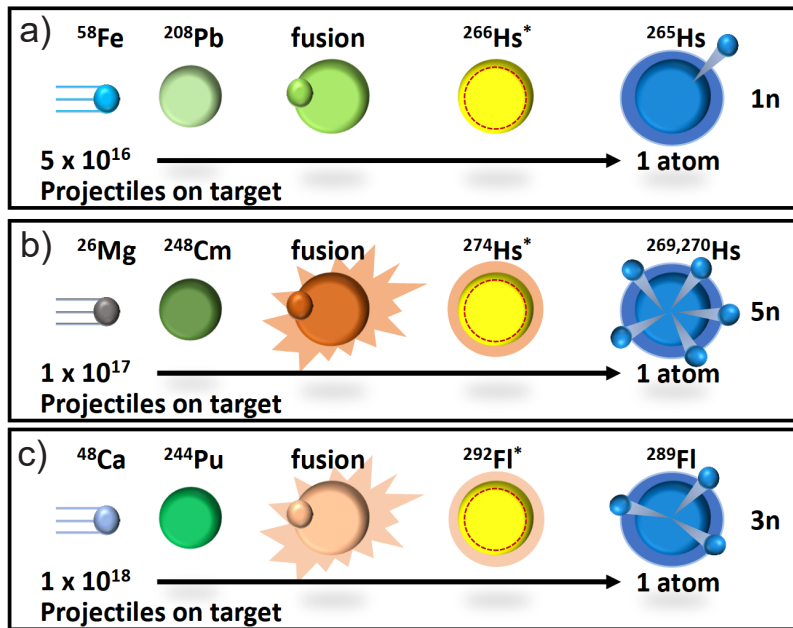


Figure 1.3: The different fusion reaction paths for the production of superheavy elements. The cold fusion reaction is shown in a), the hot fusion reaction in b) and the warm fusion reaction in c) [23].

1.3 Targets for SHE production

Targets are crucial components for fusion experiments at particle accelerators, as they provide the stationary reaction partner necessary for the formation of compound nuclei [34]. The choice of target material depends on the specific objectives of the experiment and on key experimental parameters, such as the type and energy of the ion beam [35, 36]. As accelerator technology advances and experimental setups become more sophisticated, the strains placed on targets continue to increase, requiring continuous development in target design and production techniques [34, 37].

The ideal target would be self-supporting, maintaining stability without requiring any supplementary backing material. It should also be elementally pure and monoisotopic in order to minimize competing nuclear reactions and reduce background signals in the detection system. Furthermore, it must possess an optimal thickness tailored to the excitation function of the reaction and to the intensity of the ion beam, maximizing the probability of the desired nuclear reaction while maintaining structural integrity under irradiation.

In practice, however, such ideal targets are rarely feasible due to various material and technical constraints. In many cases, there is insufficient material to produce self-supporting foils of the desired thickness. Some elements are chemi-

cally reactive, toxic, or so radioactive, making them difficult to isolate and handle in pure elemental form. Other isotopes, such as ^{248}Cm or ^{249}Bk , are extremely rare and available only in limited quantities, complicating the preparation of bulk material or elemental layers [38]. For this reason, most targets are a combination of a carrier foil, as a backing, made of titanium for example, and a thin layer of the target material on the backing [35, 37, 38].

To conserve material and because separation is not feasible for rare isotopes, it is often necessary to forgo the use of monoisotopic samples and instead work with isotopic mixtures, despite the potential for reduced selectivity in reaction channels. Limited availability may also prevent the fabrication of targets with optimal thickness, resulting in thinner targets, than would be considered optimal, that compromise reaction yield [35–38].

Consequently, actinide targets used in superheavy element experiments are typically deposited onto thin metallic backings that provide mechanical support and thermal stability. The target material is not applied in elemental form on the backing but rather in chemically stable compounds, due to limitations in available deposition techniques. Additionally, experimental observations have shown that under intense beam irradiation and in the presence of residual oxygen in the reaction chamber, even initially pure metallic targets tend to oxidize. This oxidation is thermodynamically favored and leads to the formation of the most stable chemical species, usually oxides, which dominate under beam-induced chemical reactions [35, 37].

To fabricate thin films, various methods are available, each with specific advantages and disadvantages. One key requirement is that the target material must adhere sufficiently well to the backing to withstand the stress induced by the ion beam. Furthermore, the resulting thin film should exhibit a highly homogeneous surface and an even distribution of the target material across the entire area. Since actinide targets used for the production of superheavy elements consist of rare isotopes that are available only in limited quantities and are therefore highly valuable, the chosen deposition technique must ensure a high yield and reliably reproducible results. Among the available methods, molecular plating has proven to best fulfill these requirements [37].

1.3.1 Molecular Plating

Electrodeposition of actinides was reported as early as 1959 [39], but the method was later refined in 1962 by Parker and Falk, who introduced it as molecular plating [40]. Since then, molecular plating became the standard technique for producing actinide thin films for various applications, such as sources for alpha-particles

[41] or recoil ions [42], as standards for calibration [43], or as targets for various experiments involving irradiation neutron beams [44, 45] or ion beams [46, 47]. In MP, actinides are dissolved in diluted acids such as nitric or hydrochloric acid. Afterwards, the desired amount of actinides is further diluted in organic solvents. Typically alcohols such as isopropanol and isobutanol are used for this technique [40, 43, 48]. A current density of $1-3 \frac{\text{mA}}{\text{cm}^2}$ is applied to the solution. This leads to voltages of several hundreds to thousand volts. The deposition takes 1-5 h, depending on the size and geometry of the target [46, 48]. After the deposition the remaining solution is pulled out via a pipette and the cell is dismantled. The thin film on the substrate is put to the side to let the thin film dry. The cell is cleaned and could be reused. For each radioactive isotope a separate cell is produced to prevent cross contamination with other isotopes.

The shape and size of the deposition cells can vary and, theoretically, can be adjusted to meet the desired geometry of the target [38, 46, 48]. The cell consists of a cathode, typically made of titanium, which is connected to the substrate, and an anode, which serves as the counter electrode and is commonly composed of platinum or palladium. Unlike other electrochemical setups, there are no additional electrodes, such as a reference electrode. Instead, current and voltage are measured between the anode and cathode [40, 48].

In the standard configuration, the cathode and substrate are positioned at the bottom of the cell, while the electrolyte solution is poured over them. The anode is often in the form of a wire or a wire shaped into a flat spiral to increase surface area, and it is submerged within the electrolyte solution [49]. Other shapes of the anode are also possible like nets [50]. A Scheme of a plating cell is shown in Figure 1.4 a).

Alternative designs were developed for different sizes and shapes of the desired targets. For TASCAs the cell features a side-mounted configuration, where both the anode and cathode are positioned on the sides of the cell. In this arrangement, the cell has an opening at the top to allow for the introduction of the electrolyte solution. In this case, the anode typically mirrors the shape of the cathode (see Figure 1.4 b)).

In MP the deposition yield is typically around 80-90 % achieving layer thicknesses of up to $800 \frac{\mu\text{g}}{\text{cm}^2}$ and the thin films are macroscopically homogeneous. Additionally, they are robust, surviving even ion beam irradiation in experiments e.g. superheavy element productions [37, 46, 48].

The thin films exhibit a uniform distribution of the target material. However, microscopic analysis reveals internal variations. The films are not continuous but

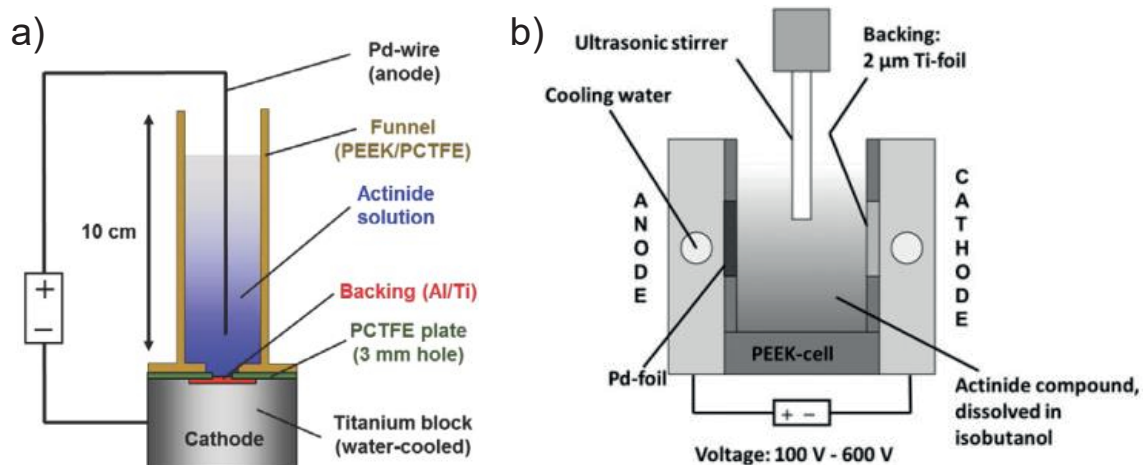


Figure 1.4: Schematic drawing of the different cells used for molecular plating. In a) a small cell with the description of the single parts for circular shaped targets is shown [49]. In b) a cell for TASCA targets with the description of the single parts is shown [38].

composed of cracks and tiles. These tiles differ in size and possess uneven surfaces. Due to their resemblance to dried mud, this phenomenon is referred to as "mud cracking". This phenomenon is shown in Figure 1.5.

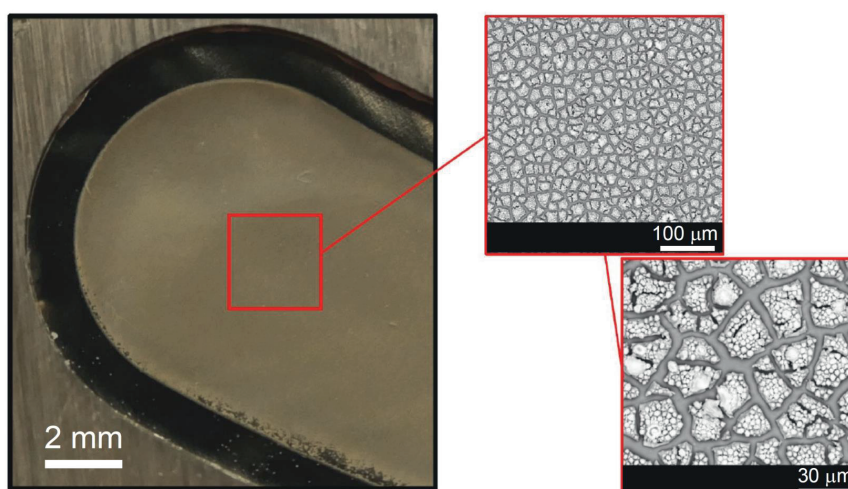


Figure 1.5: A picture of a molecular plated thin film in TASCA geometry in different magnifications. On the left a photo is shown and on the right the pictures were taken with a scanning electron microscope. $500 \frac{\mu\text{g}}{\text{cm}^2}$ of ^{147}Sm was deposited [34].

The exact mechanism of crack formation is not yet fully understood [48, 51–54]. Vascon et al. [48] concluded that the solvent used during deposition plays a key role. While moist films showed few or no cracks, distinct patterns appeared after

drying, suggesting that solvent evaporation is a major factor. Volatile solvents expand as gas and induce tensile stress that ruptures the film, whereas solvents with lower vapor pressures evaporate more slowly, reducing crack formation.

Thus, solvent selection is a crucial parameter influencing mud cracking. Other factors may also contribute and should be investigated further. Since mud cracking is believed to reduce the mechanical stability of thin films [43], understanding this phenomenon is essential for improving the performance and durability of target materials exposed to ion beams in superheavy element research.

Although molecular plating has been known for over 60 years and is well-established for target production, many aspects of the process remain poorly understood. Early hypotheses, such as those proposed by Parker and Falk [40], suggested that actinides were deposited in the form of their original salts, with the presence of nitrates and chlorides in the thin films. However, subsequent experiments [54?] have disproved this assumption, confirming the absence of these compounds and demonstrating that the deposition mechanism is fundamentally different.

In 1959, three years prior to the introduction of the molecular plating technique, Hansen proposed a potential mechanism for the electrodeposition of actinides from organic solvents. He suggested that the process involved hydroxide precipitation, a concept that aligns with the later findings of molecular plating. Unlike conventional electrochemical deposition, molecular plating primarily operates through hydroxide precipitation. Water plays a crucial role in this process, serving as the primary source of hydroxides. At the cathode, water molecules are reduced, leading to the formation of hydroxides and hydrogen gas. The increase in local pH at the cathode, due to hydroxide production, induces the precipitation of the target material [48, 51, 54, 55]. It is assumed that the hydrogen gas produced during this process escapes from the system. The resulting thin films primarily consist of hydroxides and oxides of the actinides, reflecting the nature of the precipitation process.

Spectroscopic analyses by Vascon et al. [48] further revealed that the thin films produced by molecular plating also contain organic compounds. Vascon suggested that these compounds originate from the solvent, which undergoes partial decomposition during the process.

Even today, the process is not fully understood, as indicated by the uncertainty surrounding the reason why the layer thickness is limited to approximately $800 \frac{\mu\text{g}}{\text{cm}^2}$ [46].

1.3.2 Target geometry and substrate specifications

In ion beam experiments, the specific design requirements of targets vary depending on the experimental setup. The target geometry is largely determined by the type of separator used for the production of superheavy elements. Even within a single research institution, such as GSI, targets fabricated for one separator system (e.g., TASCA) cannot necessarily be used in another, such as SHIP.

Despite these differences, all targets share one essential feature: they are constructed so that multiple target segments form a rotating wheel such as shown in Figure 1.6 [14, 34, 38]. Continuous rotation distributes the heat load over a larger surface area, thereby allowing for longer irradiation periods and a substantially higher production rate of superheavy elements without the need for cooling breaks [37, 56].



Figure 1.6: ^{249}Bk deposited with the molecular plating technique. The wheel is made of four target segments prepared individually [38].

In the irradiation process for the production of SHE the beam passes first the backing of the target, before it hits the target material. This way the produced SHE would not have to pass the backing material and would be stopped inside the backing material (Figure 1.7). Since not only the target layer but also the backing foil is exposed to the ion beam, the properties of the backing material are equally important. It must be electrically conductive for the production of the targets through MP, sufficiently thin to minimize energy loss of the beam, yet mechanically stable enough for handling and operation under experimental conditions. High

thermal stability and low thermal expansion are essential to prevent melting or cracking during irradiation. Moreover, the backing should minimally decelerate the ion beam and possess a low atomic number to reduce unwanted reaction products between the beam and the backing material. Such reactions can produce alpha-emitting isotopes, increasing the background in the alpha spectra and thus complicating the identification of alpha decays from superheavy elements [34, 37].

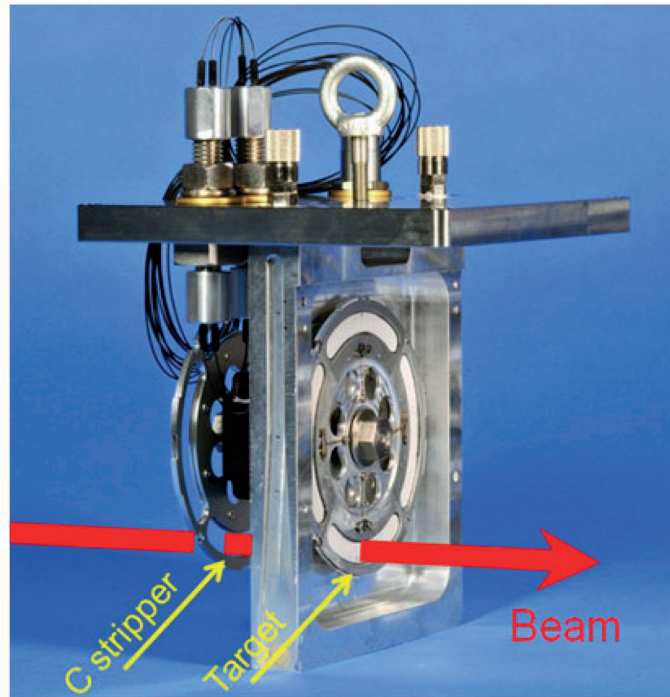


Figure 1.7: The path of the ion beam through a target wheel at TASCA. The ion beam passes first a stripper foil. Afterwards it goes through the backing material of the target, before it passes the target layer itself [57].

Taking all these requirements into account, titanium is predominantly used as a backing material. It can be rolled to thicknesses below $3\ \mu\text{m}$ while maintaining mechanical and thermal stability during both deposition and irradiation. Titanium also has a high melting point, low thermal expansion, and, with an atomic number of 22, does not form undesirable reaction products that emit alpha radiation during SHE production [34, 37].

Nevertheless, carbon exhibits even more favorable physical properties and would theoretically be a superior backing material. However, the fabrication and handling of thin carbon foils remain challenging, particularly during the target preparation process [34, 37]. Further research and technical development are therefore required to enable the reliable production of carbon-backed targets.

1.3.3 Ideal target thickness

In the synthesis of superheavy elements, the optimal thickness of the target material is constrained by two primary factors. The first limitation arises from the range of projectile energies over which superheavy elements can be successfully produced [58]. As the projectile beam passes through the target, it loses energy through interactions with the target atoms, leading to a gradual decrease in the projectile's effective energy. Since the successful formation of superheavy elements occurs only within a narrow window of projectile energies near the fusion barrier, excessive target thickness can cause the beam energy to lose energy which reduces the production rate of superheavy elements [37, 58, 59].

The second limiting factor is the recoil range of produced SHE within the target material. After formation, the produced SHE must recoil out of the target to be detected by the separator. If the target is too thick, these nuclei lose too much energy through collisions with target atoms and may stop within the target layer, preventing their detection and identification [58].

In cold-fusion reactions, where the excitation energy of the compound nucleus is relatively low, the primary factor limiting target thickness is the energy loss of the incident beam [59]. Maintaining the beam energy within the narrow range that favors residue formation is critical. In contrast, for hot-fusion reactions—where higher excitation energies lead to larger recoil energy dissipation—the principal limitation arises from the relatively low recoil velocities of the produced SHE. In this case, overly thick targets cause significant slowing of the residues, thereby reducing their transmission efficiency through the separator and overall detection probability [37].

The energy loss of the ion beam in a target occurs primarily due to scattering effects, which increase both with target thickness and with decreasing beam energy [58]. The magnitude of the energy loss depends on several factors: the type of ion used in the beam, its initial kinetic energy, and the atomic composition and density of the target material. The energy loss of a specific ion with a given energy in a particular target material can be calculated using established stopping power models. By performing such calculations over a defined path length—corresponding to the target thickness—one can determine the optimal target thickness for a given reaction [60].

The ideal target thickness is determined by the full width at half maximum (FWHM) of the excitation function for the production of superheavy elements. In cold fusion reactions, the FWHM of the excitation function is typically around 5 MeV (see Figure 1.8 a)). This corresponds to an optimal target thickness of approximately

$500 \frac{\mu\text{g}}{\text{cm}^2}$, which matches the commonly used target thicknesses in such experiments. In contrast, in hot fusion reactions, such as those involving ^{48}Ca projectiles and actinide targets, the FWHM exceeds 10 MeV (see Figure 1.8 b)). Considering the energy loss of ^{48}Ca ions in actinide targets, theoretical calculations suggest that target thicknesses up to about $1500 \frac{\mu\text{g}}{\text{cm}^2}$ could be employed to enhance the production rate of superheavy elements [37, 59].

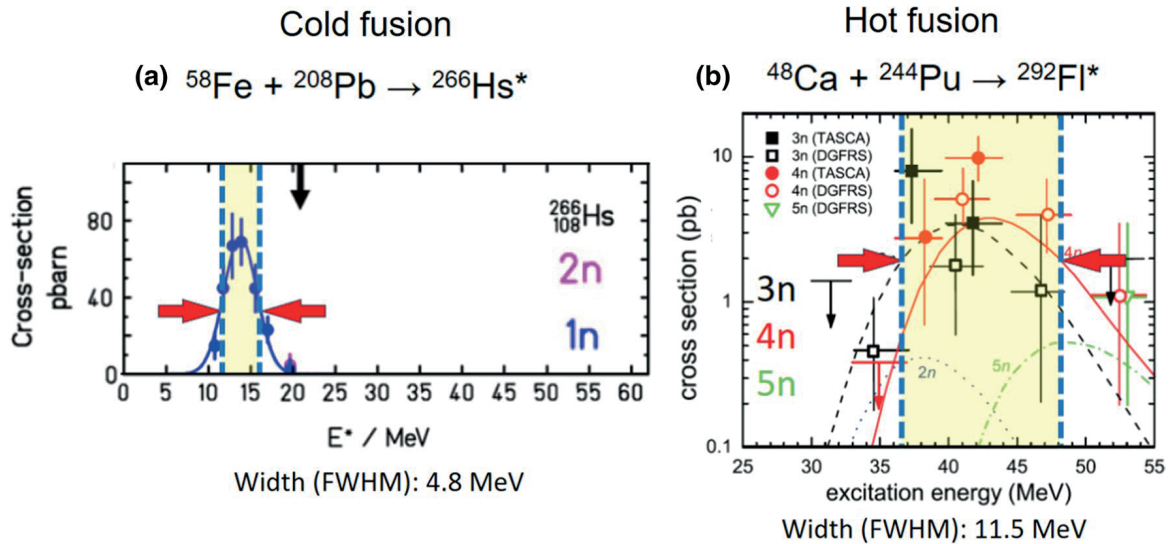


Figure 1.8: The excitation function for the production of the compound nucleus ^{266}Hs from the cold fusion reaction of ^{58}Fe on ^{208}Pb (a) and for the production of the compound nucleus ^{292}Fl from the hot fusion reaction of ^{48}Ca on ^{244}Pu (b) [37].

However, with increasing target thickness, the scattering angle of the ions, and therefore consequently of the produced SHE, also increases [58]. As the beam penetrates deeper into the target, multiple scattering causes deviations from the incident beam direction, meaning that not all residues are emitted perpendicular to the target surface. Since not every separator for superheavy element research possesses a sufficiently large angular acceptance, some of these residues may fall outside the angle acceptance window and thus remain undetected. Newer separators were constructed with increased acceptance windows. [37, 61–63].

Despite these theoretical considerations, actinide targets with such large thicknesses cannot currently be produced using available techniques. With molecular plating, targets can be reliably fabricated only up to just below $800 \frac{\mu\text{g}}{\text{cm}^2}$ [46]. However, above approximately $500 \frac{\mu\text{g}}{\text{cm}^2}$, both the error rate and film quality begin to deteriorate significantly, which is why thicker actinide targets have not yet been realized [37, 46, 58]. This limitation is especially critical when working with valuable isotopes such as ^{248}Cm , where high reliability and long-term stability of the

targets are essential [38]. For certain isotopes, such as ^{249}Bk , the available material is insufficient to produce targets of such thickness. Moreover, handling large quantities of actinide material, which are typically strong alpha emitters, is technically challenging and poses contamination and incorporation risks.

Nevertheless, research is ongoing to develop reliable methods for fabricating targets with layer thicknesses up to $1500 \frac{\mu\text{g}}{\text{cm}^2}$. These efforts focus on advancing electrochemical deposition techniques similar to molecular plating, incorporating concepts from modern electrochemistry to improve film homogeneity, adhesion, and reproducibility [64].

1.3.4 Ion beam-induced changes of thin films

When a target is irradiated with an ion beam, the ions lose energy as they pass through the target material. The amount of energy deposited depends on several factors: the energy and atomic number of the projectile ions, as well as the isotopic composition, density, and thickness of the target. This deposited energy induces both physical and chemical changes in the target material.

From a chemical perspective, the localized energy deposition can initiate various reactions within the target. The specific reactions depend on the chemical composition of the target. If the target contains organic compounds, these can decompose under irradiation, releasing gases such as CO_2 from the thin film [55]. In addition, residual oxygen within the target chamber or within the material itself may react with the target elements, leading to the formation of stable oxides. Since oxides are typically the most thermodynamically stable chemical state, further chemical reactions are generally suppressed once oxidation has occurred [37, 55].

The ion beam also leads to local heating of the target. To distribute the thermal energy evenly and prevent localized damage, the target is often designed to rotate during irradiation [34, 37, 38, 57]. Without such motion, continuous exposure of a single area to the ion beam would result in target degradation or even destruction [34, 46, 57]. Unlike conventional heating processes, such as furnace heating, ion-beam-induced heating occurs rapidly and locally, followed by almost equally rapid cooling. This transient and localized thermal excitation is described by the thermal spike model [65], in which the temperature in the irradiated region rises and falls sharply, creating only short-lived temperature peaks. Consequently, physical and chemical processes under these conditions can differ from those observed under slow and homogeneous heating [55, 66].

After irradiation, optical changes of the target surface can be observed (See Figure

1.9) . Before irradiation, molecular plated targets often exhibit characteristic mud cracking [34, 66]. Following irradiation, however, this surface structure can change: the tiles may shrink, leading to wider cracks [55], or alternatively, the thin film may appear to smooth out as if it had “melted” [66].

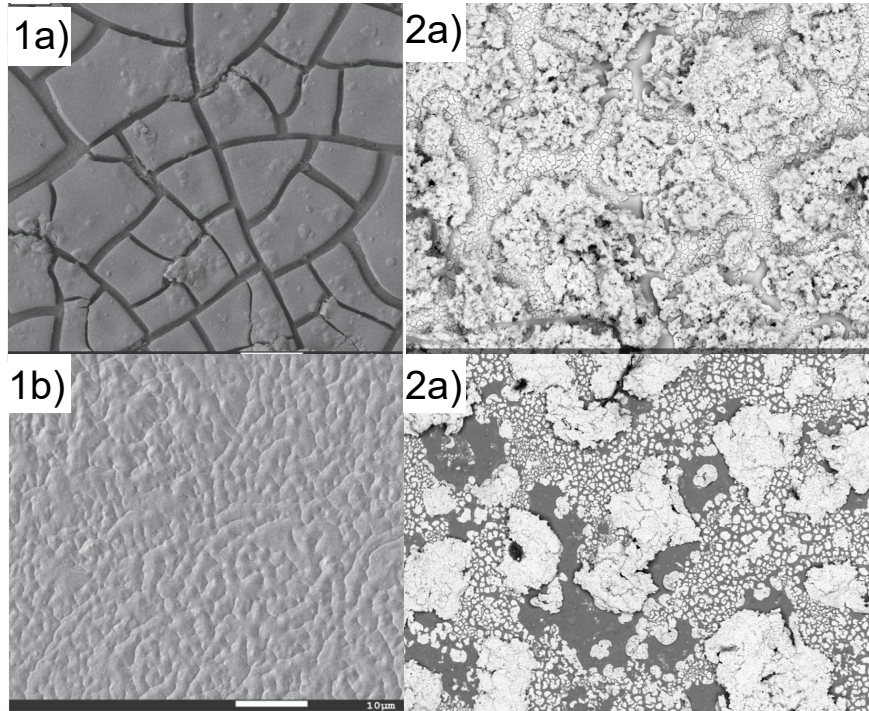


Figure 1.9: Electroplated thin films analyzed with a scanning electron microscope before and after irradiation. 1 shows a molecular plated ^{160}Gd -target a) before irradiation and b) after irradiation with ^{45}Sc and ^{50}Ti -beam with a total fluence of $3.2 \cdot 10^{14} \frac{\text{ions}}{\text{cm}^2}$ and an energy of 3.8 to $4.7 \frac{\text{MeV}}{\text{u}}$ [66]. 2 shows a thulium thin film produced by the triflate method a) before irradiation and b) after the irradiation with a ^{48}Ca -beam with a fluence of $3.9 \cdot 10^{14} \frac{\text{ions}}{\text{cm}^2}$ and an energy of $6.0 \frac{\text{MeV}}{\text{u}}$ [64]

The specific outcome depends on both the target composition and the nature of the ion beam, though the underlying mechanisms remain not fully understood. Although it may appear that the target material is lost during irradiation, alpha spectra of the irradiated targets indicate that their activity remains constant. The peaks in the alpha spectra become narrower, while the integral remains unchanged (See Figure 1.10). This demonstrates that not only is the material preserved after irradiation, but also that the alpha particles lose less energy when exiting the thin layer. Prolonged irradiation may also cause diffusion of target material into the backing substrate [67, 68].

These surface modifications occur early during irradiation and are believed to

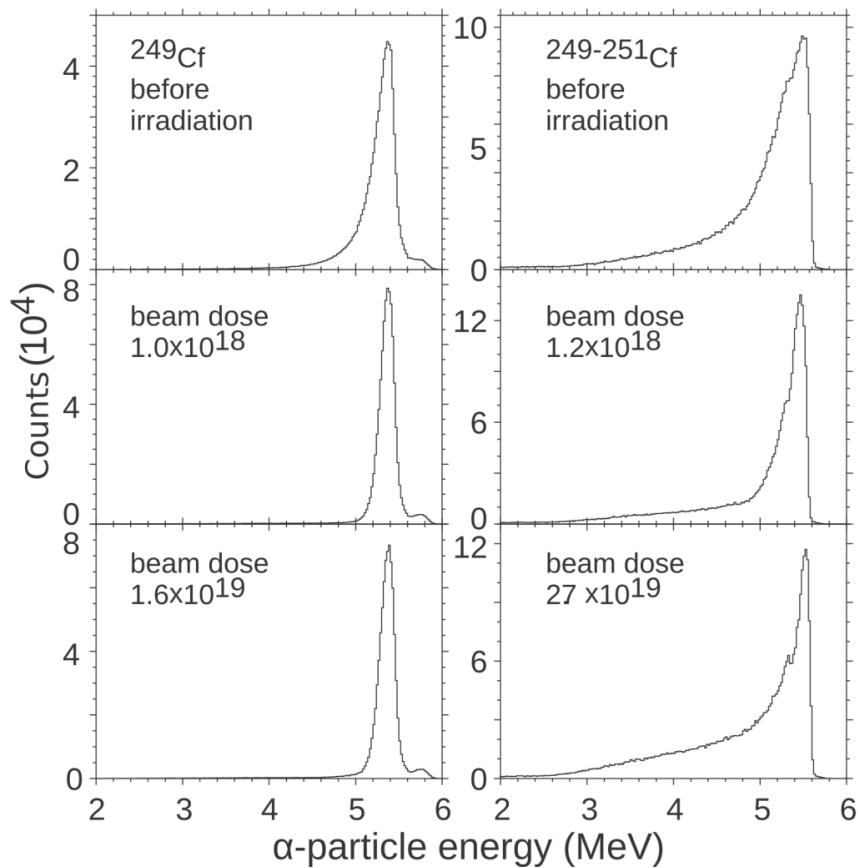


Figure 1.10: α -spectra measured from the ^{249}Cf (left panel) and mixed-Cf (right panel) at DGFRS (Dubna Gas-Filled Recoil Separator) before and after irradiation with ^{48}Ca in different doses [67].

contribute to a stabilization of the thin film. This initial conditioning process is commonly referred to as baking-in [34, 37]. During the baking-in process, the target is exposed to a reduced beam intensity, allowing the material to reach a thermodynamically stable chemical state—typically through the formation of oxides or other stable compounds [34, 55]. Once this stabilization phase is complete, the target can withstand full beam power without further structural degradation of the thin film.

1.4 Characterization methods

In this work, various methods were applied to characterize the fabricated thin films. The yields of the depositions were investigated using neutron activation analysis (NAA) in combination with γ -spectroscopy. To study the homogeneity and morphology of the thin films scanning electron microscopy (SEM) was used. The chemical composition of the thin films was analyzed through Raman and infrared (IR) spectroscopy. Additionally, X-ray photoelectron spectroscopy (XPS), elastic recoil detection analysis (ERDA), and Rutherford backscattering spectrometry (RBS) were applied in combination with proton-induced X-ray emission (PIXE). This section focuses on the theoretical and technical aspects of each of these methods.

1.4.1 Neutron activation analysis and gamma spectrometry

In neutron activation analysis (NAA), a sample is exposed to neutrons to induce nuclear reactions. By neutron capture processes, many nuclides can be transformed into relative short-living isotopes with characteristic γ -lines. Because these isotopes produce characteristic γ -ray signatures, the elemental and isotopic composition of the sample can be identified [69]. As free neutrons are unstable and decay to protons via β^- -decay, they cannot be stored. Instead, they must be constantly produced via neutron sources. The TRIGA Mark II reactor in Mainz, for example, serves as a neutron source, which produces neutrons via the nuclear fission of ^{235}U [70]. These neutrons have high kinetic energies at the moment of release and are therefore called fast neutrons. For NAA, however, so-called thermal neutrons are typically required, which have a lower kinetic energy. Hydrogen is used as a moderator to moderate the neutrons to the desired energy. In the case of the TRIGA reactor, this hydrogen is enclosed in a zirconium hydride matrix.

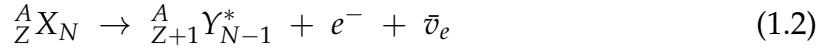
The TRIGA Mark II reactor in Mainz has a thermal output of 100 kW in continuous mode, which corresponds to a thermal neutron flux of $4.2 \times 10^{12} \frac{1}{\text{cm}^2 \text{s}}$ for this reactor. It can also be operated in pulsed mode. This increases the thermal power to 250 MW for 30 ms, whereby a thermal neutron flux of $1 \times 10^{16} \frac{1}{\text{cm}^2 \text{s}}$ is achieved [70].

The neutron is captured by an atom, causing the neutron number N and the mass number A to increase by 1, while the proton number Z remains constant.

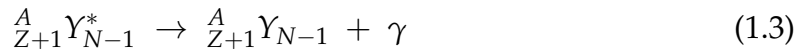


The isotope produced in this way is often unstable and decays due to the excess neutron via β^- -decay. As a result of this process, the mass number remains

constant, the neutron number decreases by 1, and the proton number in the atom increases by 1, resulting in an element with a higher atomic number.



Following this process, the atomic nucleus often transitions to an excited state. To reach the ground state, the nucleus emits energy in the form of γ radiation, which can then be detected, enabling qualitative and quantitative elemental analysis of an unknown sample.



The activity of a specific element A after activation with neutrons can be calculated as a function of the irradiation time t .

$$A(t) = \sigma \Phi N_0 [1 - \exp(-\lambda t)] \quad (1.4)$$

$$\lambda = \frac{\ln(2)}{t_{\frac{1}{2}}}$$

N_0 is the number of irradiated nuclei of an isotope. The number of irradiated nuclei depend on the abundance of the specific isotope in the sample, the atomic mass of the isotope and the overall mass of the sample. σ is the neutron capture cross section of the irradiated isotope. Typically thermal neutrons are used for irradiation and therefore the neutron capture cross section for thermal neutrons are typically used. Φ is the neutron flux of the neutron source. Since σ is constant, Φ should be known and can be considered constant for small samples, and N_0 could be seen as constant for short irradiation times, t is the only variable in equation 1.4.

This formula shows, that NAA can be used as an absolute method for quantitative analysis of samples, if the neutron-flux and the cross-section are known with sufficient precision. Alternatively, a standard can be used for quantitative measurements. By choosing a standard with the same geometry and well-defined mass of the analyzed nuclide, analysis will become easier, since geometric effects can be reduced from the equations. The mass of the sample m_x can then easily be

calculated by the γ activity of the sample A_x and the γ -activity of the standard A_{St} and the mass of the standard m_{St} :

$$m_x = m_{St} \frac{A_x}{A_{St}} \quad (1.5)$$

The precision of this instrumental activation analysis can be further enhanced, by a chemical separation of the nuclide of interest and the rest of the sample, before or after the activation.

The γ -rays are typically measured with a scintillation or semiconductor detector. Scintillation counters operate on the principle that high-energy γ -radiation interacts with a scintillator, typically an inorganic crystal, such as thallium-doped NaI or an organic polymer. The incoming radiation excites the material, which then emits visible light as it de-excites. This light is converted into an electrical signal by the photocathode of a photomultiplier via the photoelectric effect. The intensity of this signal depends on the number and energy of the incoming γ -photons, allowing scintillation counters to record γ -spectra. A key advantage of these detectors is their high detection efficiency, making them particularly suitable for quantitative measurements. However, their energy resolution is lower than that of semiconductor detectors, limiting their ability to perform multi-element analysis.

Semiconductor detectors are made of a semiconductor material, with high-purity germanium detectors (HPGe) being the most commonly used type. In these detectors, an electric voltage is applied, and when ionizing radiation strikes the detector, electrons are excited from the valence band to the conduction band, generating a measurable electrical pulse. Unlike scintillation counters, semiconductor detectors offer better energy resolution, making them particularly well-suited for γ -spectroscopy. However, they require cooling to function properly: HPGe detectors must be cooled with liquid nitrogen during operation to prevent high leakage currents, which would otherwise render measurements impossible.

In both types of detectors, the generated electrical signal is relatively weak and must be amplified. The amplified signal is initially in analog form and is then converted into a digital signal using an analog-to-digital converter (ADC). This digital signal is stored in a multi-channel analyzer (MCA), resulting in a spectrum where the counts are plotted against the channel number.

To obtain an energy spectrum, an energy calibration of the channels is required. This is achieved using a multi-element standard with well-defined γ -energies. By corre-

lating each channel with a specific energy, a calibrated γ -spectrum can be generated.

1.4.2 Scanning electron microscopy

Scanning electron microscopy (SEM) is a microscopy technique that provides resolutions ranging from micrometers to nanometers. Unlike light microscopy, it does not use visible light for imaging but accelerated electrons [71]. This is due to the wave-like properties of electrons, which can be used for microscopy. These properties can be described using the de Broglie equation. The wavelength of an electron, λ , can be determined by dividing the Planck constant h by the momentum of the electron p .

$$\lambda = \frac{h}{p} \quad (1.6)$$

Since the electrons in SEM are accelerated to several keV, they have a shorter wavelength, than visible light. This increases the resolution limit of the microscope. This effect is described by Abbe's law [72]. The law defines the minimum distance two points must have in order to be perceived as separate objects. It relates the resolution d of a microscope to the numerical aperture NA, which is a device-specific value that also considers the quality of the objective lens, and the wavelength λ .

$$d = \frac{\lambda}{2\text{NA}} \quad (1.7)$$

A SEM uses a cathode to generate electrons via the thermionic emission effect [71], which are then accelerated toward the sample. Electromagnetic lenses, consisting of anodes, focus the electron beam onto the sample.

When the electron beam interacts with the sample, various interactions occur, leading to the emission of secondary electrons (SE), backscattered electrons (BSE), and X-rays. SE and BSE can be detected using specialized electron detectors, such as a scintillation counter.

Secondary electrons (SE) are generated when primary electrons eject electrons from the sample. Due to their low energy (< 50 eV), they originate only from the uppermost layers of the sample. The SE detector is positioned at an angle to the electron beam to capture these electrons efficiently. SE mainly provide information from the near-surface region and therefore allow for detailed imaging of the sam-

ple's topography.

Backscattered electrons (BSE) are primary electrons that have been elastically scattered by atomic nuclei in the sample with an angle of almost 180° [73, 74]. They have higher energy than SE and can be deflected from deeper layers. The probability of backscattering depends on the atomic number of the elements in the sample: the higher the atomic number, the more likely electrons are to be backscattered [73, 74]. This creates a contrast in BSE imaging, where regions with elements of higher atomic numbers appear brighter than those with lower atomic numbers. The BSE detector is positioned parallel to the sample surface to efficiently capture the backscattered electrons.

In addition to electron detection, emitted X-rays can also be analyzed. These X-rays are generated by the interaction between the electron beam and the sample. The emission of secondary electrons from the sample creates vacancies in the inner electron shells, which are subsequently filled by outer electrons. This process releases energy in the form of X-rays. These X-rays can be detected using a semiconductor detector. Energy-dispersive X-ray spectroscopy (EDX) utilizes this radiation for elemental analysis [73, 75]. The energy of the emitted X-rays depend on the atomic number of the respective element, the elemental composition of the sample can be determined, using the equation of Moseley's law [73, 75].

$$E = h \cdot f_R \cdot Z_{\text{eff}}^2 \left(\frac{1}{n_1^2} - \frac{1}{n_2^2} \right) \quad (1.8)$$

In this equation, E represents the energy of the X-rays, h is the Planck constant and f_R the adjusted Rydberg frequency. The effective atomic number is denoted by Z_{eff} . The variables n_1 and n_2 refer to the principal quantum numbers of the electronic states, where n_1 corresponds to the inner electron shell and n_2 to the outer electron shell.

To analyze not just a single point but a larger area of the sample, the electron beam is scanned in a raster pattern across the surface, thus the name Scanning Electron Microscopy. This is achieved by deflecting the beam using electromagnetic lenses, allowing for high-resolution imaging over extended areas.

A schematic representation of an electron microscope is shown in Figure 1.11.

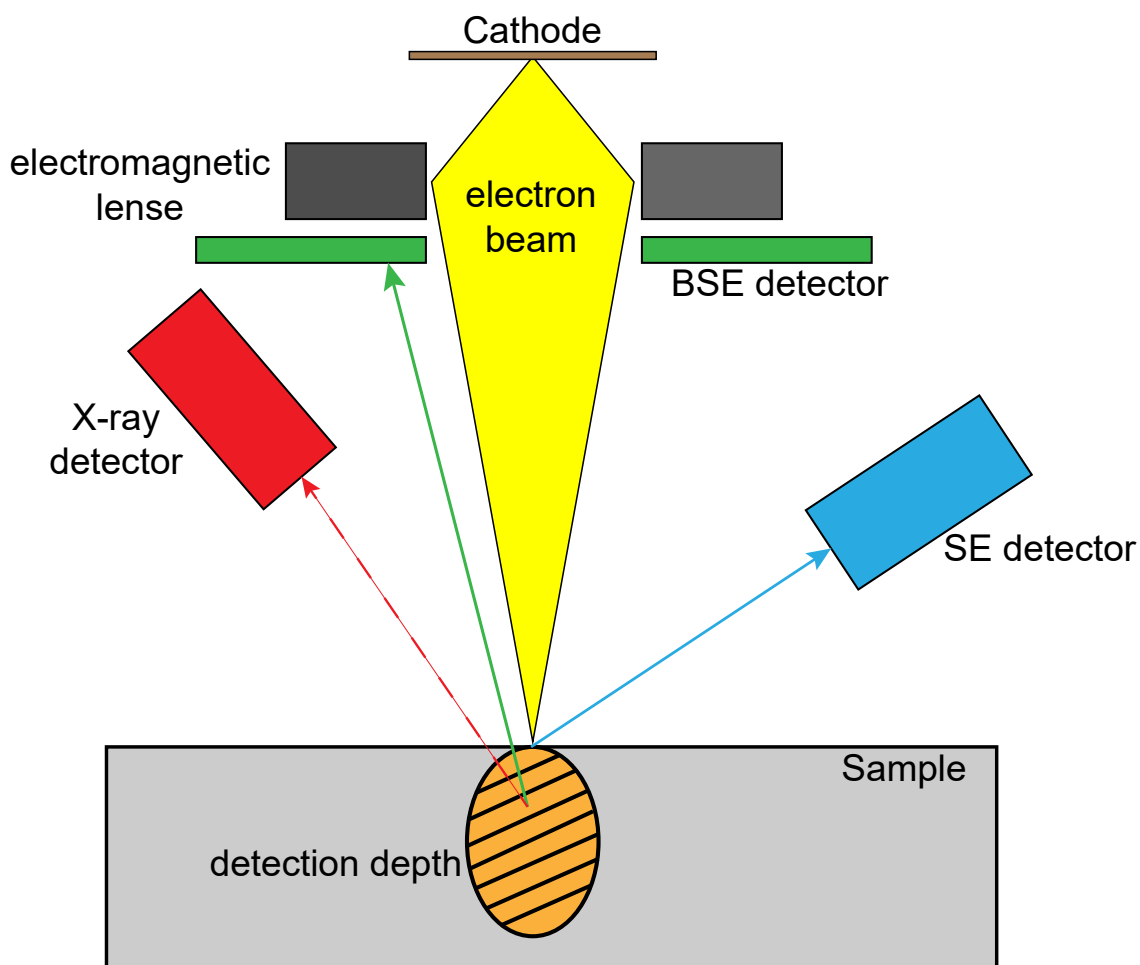


Figure 1.11: Schematic illustration of a SEM. The electron beam is scanning over a sample and induces thereby the generation of secondary electron (blue) from the surface. Backscattered electron (green) and X-rays (red) are also generated from deeper layer depths.

1.4.3 Raman and infrared spectrometry

Raman and infrared (IR) spectroscopies are widely used in chemistry for the identification of molecules and the characterization of their chemical bonds by investigating vibrational, rotational, and low-frequency modes [76].

In Raman spectroscopy, monochromatic laser light is used to excite molecular vibrations. When light interacts with the sample, most photons are elastically scattered (Rayleigh scattering), but a small fraction is inelastically scattered, resulting in light of slightly different frequencies. The difference between the scattered light frequency and the excitation frequency is called the Raman shift:

$$\Delta\tilde{\nu} = \left(\frac{1}{\lambda_{\text{Excitation}}} - \frac{1}{\lambda_{\text{Scattered}}} \right) \quad (1.9)$$

where $\Delta\tilde{\nu}$ is usually expressed in wavenumbers (cm^{-1}).

During Raman scattering, the molecule is temporarily excited to a virtual energy state with a very short lifetime, after which a photon is emitted and the molecule ends up in a different vibrational or rotational state. Therefore, the Raman shift corresponds to the energy difference between the initial and final molecular states.

This process is allowed only if the vibration induces a change in the molecular polarizability. Vibrations that are Raman-active typically include symmetric stretching modes, such as the C–C stretching vibration in ethane [77].

If the final vibrational state is higher in energy than the initial state, the scattered photon loses energy and is shifted to a lower frequency (Stokes shift). Conversely, if the final state is lower in energy, the photon gains energy (Anti-Stokes shift). The intensity of the Raman lines correlates with the polarizability of the molecule's electrons. Raman-scattered light is typically analyzed using an optical spectrometer.

Raman spectroscopy is not only a chemical analysis tool but is also widely used in solid-state physics and materials science to probe composition, crystallographic orientation, mechanical stress (due to temperature or pressure), and crystallinity [78, 79].

In contrast, infrared (IR) spectroscopy uses a continuous spectrum of infrared light rather than monochromatic visible light [76]. Instead of analyzing scattered light, IR spectroscopy measures the absorption of IR light by a sample. The decrease in transmitted IR intensity as a function of wavelength provides information about the vibrational characteristics of chemical bonds.

For a vibrational mode to be IR-active, it must involve a change in the dipole moment of the molecule during vibration, rather than a change in polarizability as in Raman spectroscopy. These are typically asymmetric vibrations, such as the stretching of a C=O bond [77].

Consequently, IR and Raman spectroscopy are complementary techniques: IR is sensitive to vibrational transitions involving changes in dipole moment, while Raman is sensitive to those involving changes in polarizability. Together, they

provide a more complete picture of molecular vibrations [76, 77].

1.4.4 X-ray photoelectron spectroscopy

X-ray Photoelectron Spectroscopy (XPS) is a powerful analytical technique used to qualitatively determine the chemical composition of solid surfaces. The surface is irradiated with X-rays of a specific wavelength, causing the ejection of inner-shell electrons from the atoms on the surface [80]. By examining the kinetic energy of the emitted electrons, the surface's chemical composition can be determined.

When a photon hits the sample surface, it causes the ejection of an inner-shell electron from an atom, which is then directed toward the detector by a hemispherical analyzer. A scheme of a setup is shown in Figure 1.12. This analyzer uses electrostatic lenses to control the range of kinetic energies that the electrons are allowed to have in order to reach the detector, providing energy resolution.

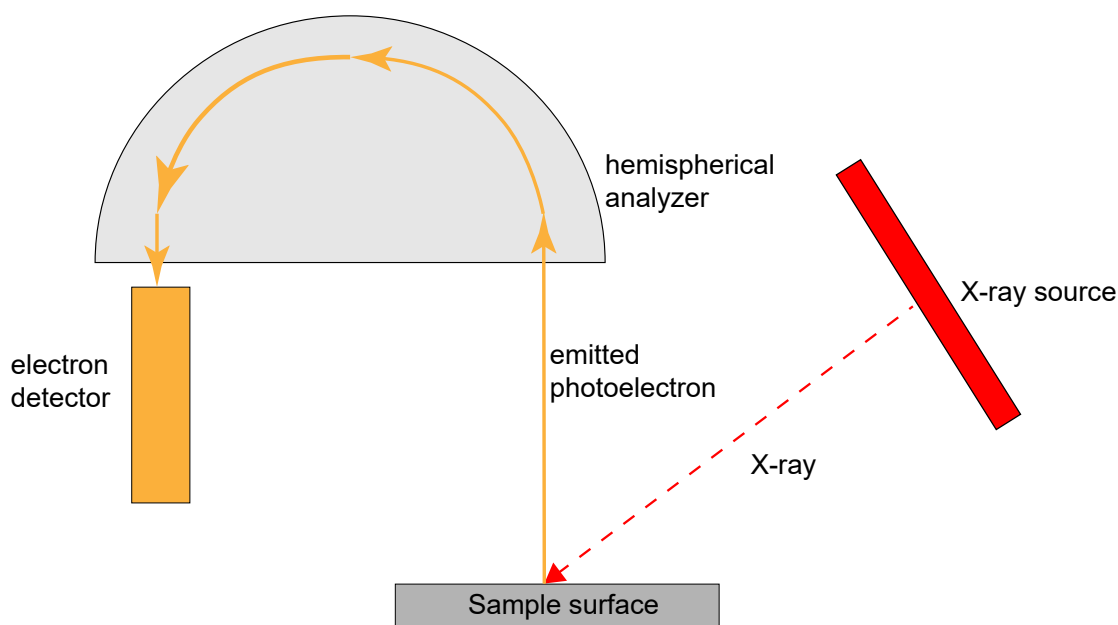


Figure 1.12: Schematic illustration of a XPS spectrometer. The sample is irradiated by X-rays (red) which lead to the emission of photoelectron from the inner-shell of the atoms at the sample surface. The emitted photoelectrons (orange) are selected by their energy and guided by the hemisphere analyzer to the electron detector.

The kinetic energy $E_{kinetic}$ of the ejected electrons is related to the energy of the incident photon and the binding energy of the electron within the atom. The binding energy $E_{binding}$ of the electron can be determined using the following equation:

$$E_{binding} = E_{photon} - E_{kinetic} \quad (1.10)$$

Here, E_{photon} represents the known energy of the X-ray used in the experiment, and $E_{kinetic}$ is the measured kinetic energy of the emitted electron. Typically, the X-ray sources use the K_{α} lines of either Magnesium ($Mg K_{\alpha} = 1253.6$ eV) or Aluminum ($Al K_{\alpha} = 1486.6$ eV) [81].

The kinetic energy of the emitted electron is characteristic not only of the element but also of the specific atomic orbital from which the electron was ejected. Depending on the element, multiple peaks may appear in the spectrum corresponding to different electron orbitals.

The spectrum is then obtained by plotting the counts against the binding energy of the detected electrons. The resolution of the spectrum can be adjusted depending on whether a broad energy range is desired for a general overview or a specific spectral line is being analyzed in more detail.

Since the binding energy of an electron is influenced by the oxidation state of the element and its chemical environment, the peaks in the spectrum shift accordingly [80]. Specifically, the binding energy of the ejected electron increases with the oxidation state of the element. When comparing two compounds where the element has the same oxidation state but different chemical bonding partners, the binding energy of the photoelectron will vary due to changes in the electron density around the element, influenced by the chemical bonding.

1.4.5 Ion-beam analysis

Proton-induced X-ray emission (PIXE), Rutherford Backscattering Spectrometry (RBS), and Elastic Recoil Detection Analysis (ERDA) are analytical techniques that utilize an ion beam to investigate material properties. They are therefore classified as ion beam analysis (IBA) methods.

In Proton-induced X-ray emission (PIXE), the sample is irradiated with protons with an energy of typically 1 – 3 MeV. These incident protons ionize inner-shell electrons of atoms in the near-surface region of the sample, leading to the emission of characteristic X-rays. Since the energy of these X-rays is element-specific, the elemental composition of the sample can be determined quantitatively. PIXE is

particularly well suited for the detection of light to medium elements with atomic numbers approximately $Z = 11 - 40$, and is capable of identifying trace elements with high sensitivity [82–84]. Compared to conventional EDX, PIXE offers substantially lower detection limits down to the ppm range, including for light elements, and provides higher analytical sensitivity with minimal spectral background, making it particularly well suited for trace element analysis [?].

Rutherford Backscattering Spectrometry (RBS) also utilizes a proton beam, although a helium beam can be used as well [82–84]. In RBS, the sample is irradiated by energetic ions, and the elastically backscattered ions are detected at a large scattering angle, typically close to 180° relative to the beam direction. The measured energy spectrum of the backscattered ions provides information about both the elemental composition and the depth distribution of the elements within the sample. Because the backscattering yield increases with the atomic number of the target atoms, RBS is particularly sensitive to heavier elements (typically $Z \geq 20$). Consequently, RBS complements PIXE, which is more effective for lighter elements.

The ion beam can be focused to a diameter of only a few micrometers using electromagnetic lenses. By scanning the focused beam across the sample surface, elemental maps can be generated that reveal the spatial distribution of elements within the specimen.

Elastic Recoil Detection Analysis (ERDA) is an ion beam analysis technique used to determine the elemental composition of a sample. Unlike PIXE and RBS, ERDA typically employs heavier ions as the incident beam, such as ^{35}Cl or ^{40}Ar , with energies in the range of 0.5 – 3 MeV per nucleon [84, 85].

Similar to RBS, ERDA is based on elastic collisions; however, instead of detecting the backscattered incident ions, atoms or ions from the sample itself are ejected through these collisions and subsequently detected. The detector is positioned at a shallow forward angle, typically $20 - 30^\circ$ relative to the sample surface, in contrast to the near 180° scattering angle used in RBS [85].

This geometry and detection scheme make ERDA particularly sensitive to light elements, such as hydrogen, carbon, nitrogen, and oxygen, which are difficult to detect with RBS [84, 85]. Like RBS, ERDA also provides depth-resolved information, allowing determination of the distribution of elements within the near-surface region of the sample.

1.5 Outline of this work

With the short overview the limitation of molecular plated thin films become visible. With further improvements of accelerator technology ion beam intensities will increase, what strains targets used in ion beam experiments. The stability of molecular plated targets hit their limit. Calculations show, that the production rate for superheavy elements produced by hot fusion reactions can be increased by thicker targets, compared to what is right now achievable via molecular plating.

To overcome the limitations of molecular plating regarding stability and layer thickness, the influence of water and CO₂ on molecular plating is studied. Additionally the chemical changes in molecular plated thin films by swift heavy ion beams were studied.

To improve thin film stability in ion beams and increase their layer thickness for increased production of SHE, modern electrochemical aspects, such as working with aprotic solutions and electrochemically inert counter ions to the f-elements cation, were implemented in the production of thin films.

Lanthanides are used as a model for actinides, since the chemistry of lanthanides and late actinides such as americium and curium, which have a high α -activity and are more rare, are similar. Without radioactivity these thin films can be analyzed at different institutes, which are not able to handle radioactive material. Furthermore, lanthanides can be activated by irradiation with neutrons. After activation the yield of the thin films can be studied. Activated lanthanides also have half-lives of days instead of hundreds of years, and have often better detectable γ -lines making detection for γ -spectroscopy easier.

1.6 References

- [1] A. Allisy, Henri becquerel: The discovery of radioactivity, *Radiation Protection Dosimetry* 68 (1) (1996) 3–10. doi:10.1093/oxfordjournals.rpd.a031848.
- [2] L. Meitner, O. R. Frisch, Disintegration of uranium by neutrons: a new type of nuclear reaction, *Nature* 143 (3615) (1939) 239–240. doi:10.1038/143239a0.
- [3] E. McMillan, P. H. Abelson, Radioactive element 93, *Physical Review* 57 (12) (1940) 1185–1186. doi:10.1103/physrev.57.1185.2.
- [4] L. R. Morss, *The Chemistry of the Actinide and Transactinide Elements*, SpringerLink, Springer Netherlands, Dordrecht, 2011.
- [5] J. Khuyagbaatar, The superheavy nuclei: Fusion-evaporation reactions, *EPJ Web of Conferences* 306 (2024) 01013. doi:10.1051/epjconf/202430601013.
- [6] N. Wang, E.-G. Zhao, W. Scheid, Synthesis of superheavy nuclei with $z=118$ in hot fusion reactions, *Physical Review C* 89 (3) (2014) 037601. doi:10.1103/physrevc.89.037601.
- [7] C. E. Düllmann, How elements up to 118 were reached and how to go beyond, *EPJ Web of Conferences* 163 (2017) 00015. doi:10.1051/epjconf/201716300015.
- [8] S. Hofmann, S. N. Dmitriev, C. Fahlander, J. M. Gates, J. B. Roberto, H. Sakai, On the discovery of new elements (iupac/iupap provisional report): Provisional report of the 2017 joint working group of iupac and iupap, *Pure and Applied Chemistry* 90 (11) (2018) 1773–1832. doi:10.1515/pac-2018-0918.
- [9] A. Türler, R. Eichler, A. Yakushev, Chemical studies of elements with z 104 in gas phase, *Nuclear Physics A* 944 (2015) 640–689. doi:10.1016/j.nuclphysa.2015.09.012.
- [10] D. Ackermann, Superheavy elements – a probe for nuclear matter at the extremes, *Progress of Theoretical Physics Supplement* 196 (2012) 255–262. doi:10.1143/ptps.196.255.
- [11] A. Türler, V. Pershina, Advances in the production and chemistry of the heaviest elements, *Chemical Reviews* 113 (2) (2013) 1237–1312. doi:10.1021/cr3002438.
- [12] V. I. Zagrebaev, W. Greiner, Production of heavy and superheavy neutron-rich nuclei in transfer reactions, *Physical Review C* 83 (4) (2011) 044618. doi:10.1103/physrevc.83.044618.

- [13] V. Y. Denisov, Production of superheavy nuclei in hot-fusion reactions, *Physical Review C* 109 (4) (2024) 044618. doi:10.1103/physrevc.109.044618.
- [14] S. Hofmann, G. Münzenberg, The discovery of the heaviest elements, *Reviews of Modern Physics* 72 (3) (2000) 733–767. doi:10.1103/revmodphys.72.733.
- [15] C. E. Düllmann, M. Block, F. P. Heßberger, J. Khuyagbaatar, B. Kindler, J. V. Kratz, B. Lommel, G. Münzenberg, V. Pershina, D. Renisch, M. Schädel, A. Yakushev, Five decades of gsi superheavy element discoveries and chemical investigation, *Radiochimica Acta* 110 (6–9) (2022) 417–439. doi:10.1515/ract-2022-0015.
- [16] Y. Oganessian, Nuclei in the “island of stability” of superheavy elements, *Journal of Physics: Conference Series* 337 (2012) 012005. doi:10.1088/1742-6596/337/1/012005.
- [17] A. Sămark-Roth, D. M. Cox, D. Rudolph, L. G. Sarmiento, M. Albertsson, B. G. Carlsson, J. L. Egido, P. Golubev, J. Heery, A. Yakushev, S. Åberg, H. M. Albers, M. Block, H. Brand, T. Calverley, R. Cantemir, R. M. Clark, C. E. Düllmann, J. Eberth, C. Fahlander, U. Forsberg, J. M. Gates, F. Giacoppo, M. Götz, S. Götz, R.-D. Herzberg, Y. Hrabar, E. Jäger, D. Judson, J. Khuyagbaatar, B. Kindler, I. Kojouharov, J. V. Kratz, J. Krier, N. Kurz, L. Lens, J. Ljungberg, B. Lommel, J. Louko, C.-C. Meyer, A. Mistry, C. Mokry, P. Papadakis, E. Parr, J. L. Pore, I. Ragnarsson, J. Runke, M. Schädel, H. Schaffner, B. Schausten, D. A. Shaughnessy, P. Thörle-Pospiech, N. Trautmann, J. Uusitalo, Spectroscopy along flerovium decay chains. iii. details on experiment, analysis, cn282 , and spontaneous fission branches, *Physical Review C* 107 (2) (2023) 024301. doi:10.1103/physrevc.107.024301.
- [18] G. Münzenberg, M. Gupta, H. M. Devaraja, Y. K. Gambhir, S. Heinz, S. Hofmann, Heavy and superheavy elements: next generation experiments, ideas and considerations, *The European Physical Journal A* 59 (2) (Feb. 2023). doi:10.1140/epja/s10050-023-00939-3.
- [19] A. Yakushev, J. Khuyagbaatar, C. E. Düllmann, M. Block, R. A. Cantemir, D. M. Cox, D. Dietzel, F. Giacoppo, Y. Hrabar, M. Iliaš, E. Jäger, J. Krier, D. Krupp, N. Kurz, L. Lens, S. Löchner, C. Mokry, P. Mošat, V. Pershina, S. Raeder, D. Rudolph, J. Runke, L. G. Sarmiento, B. Schausten, U. Scherer, P. Thörle-Pospiech, N. Trautmann, M. Wegrzecki, P. Wiczorek, Manifestation of relativistic effects in the chemical properties of nihonium and moscovium revealed by gas chromatography studies, *Frontiers in Chemistry* 12 (Sep. 2024). doi:10.3389/fchem.2024.1474820.
- [20] J. M. Gates, C. E. Düllmann, M. Schädel, A. Yakushev, A. Türler, K. Eberhardt, J. V. Kratz, D. Ackermann, L.-L. Andersson, M. Block, W. Bröchle, J. Dvo-

- rak, H. G. Essel, P. A. Ellison, J. Even, U. Forsberg, J. Gellanki, A. Gorshkov, R. Graeger, K. E. Gregorich, W. Hartmann, R.-D. Herzberg, F. P. Heßberger, D. Hild, A. Hübner, E. Jäger, J. Khuyagbaatar, B. Kindler, J. Krier, N. Kurz, S. Lahiri, D. Liebe, B. Lommel, M. Maiti, H. Nitsche, J. P. Omtvedt, E. Parr, D. Rudolph, J. Runke, H. Schaffner, B. Schausten, E. Schimpf, A. Semchenkov, J. Steiner, P. Thörle-Pospiech, J. Uusitalo, M. Wegrzecki, N. Wiehl, First superheavy element experiments at the gsi recoil separator tasca: The production and decay of element 114 in the $\text{pu244}(\text{ca48,3-4n})$ reaction, *Physical Review C* 83 (5) (2011) 054618. doi:10.1103/physrevc.83.054618.
- [21] S. Hofmann, Study of she at the gsi-ship, *Progress in Particle and Nuclear Physics* 62 (2) (2009) 337–343. doi:10.1016/j.pnpnp.2008.12.008.
- [22] K. Banerjee, D. Hinde, M. Dasgupta, E. Simpson, D. Jeung, C. Simenel, B. Swinton-Bland, E. Williams, I. Carter, K. Cook, H. David, C. Düllmann, J. Khuyagbaatar, B. Kindler, B. Lommel, E. Prasad, C. Sengupta, J. Smith, K. Vo-Phuoc, J. Walshe, A. Yakushev, Mechanisms suppressing superheavy element yields in cold fusion reactions, *Physical Review Letters* 122 (23) (2019) 232503. doi:10.1103/physrevlett.122.232503.
- [23] M. Schädel, Chemistry of superheavy elements, *Angewandte Chemie International Edition* 45 (3) (2006) 368–401. doi:10.1002/anie.200461072.
- [24] F. Rösch (Ed.), *Nuclear Chemistry*, 2nd Edition, Vol. 2 of De Gruyter graduate, De Gruyter, Berlin, 2022.
- [25] S. Hofmann, Synthesis and properties of isotopes of the transactinides, *Radiochimica Acta* 107 (9–11) (2019) 879–915. doi:10.1515/ract-2019-3104.
- [26] O. Sorlin, M.-G. Porquet, Nuclear magic numbers: New features far from stability, *Progress in Particle and Nuclear Physics* 61 (2) (2008) 602–673. doi:10.1016/j.pnpnp.2008.05.001.
- [27] M. Laatiaoui, W. Lauth, H. Backe, M. Block, D. Ackermann, B. Cheal, P. Chhetri, C. E. Düllmann, P. van Duppen, J. Even, R. Ferrer, F. Giacoppo, S. Götz, F. P. Heßberger, M. Huyse, O. Kaleja, J. Khuyagbaatar, P. Kunz, F. Lautenschläger, A. K. Mistry, S. Raeder, E. M. Ramirez, T. Walther, C. Wraith, A. Yakushev, Atom-at-a-time laser resonance ionization spectroscopy of nobelium, *Nature* 538 (7626) (2016) 495–498. doi:10.1038/nature19345.
- [28] G. Münzenberg, From bohrium to copernicium and beyond she research at ship, *Nuclear Physics A* 944 (2015) 5–29. doi:10.1016/j.nuclphysa.2015.06.008.

- [29] A. Yakushev, L. Lens, C. E. Düllmann, J. Khuyagbaatar, E. Jäger, J. Krier, J. Runke, H. M. Albers, M. Asai, M. Block, J. Despotopoulos, A. Di Nitto, K. Eberhardt, U. Forsberg, P. Golubev, M. Götz, S. Götz, H. Haba, L. Harkness-Brennan, R.-D. Herzberg, F. P. Heßberger, D. Hinde, A. Hübner, D. Judson, B. Kindler, Y. Komori, J. Konki, J. Kratz, N. Kurz, M. Laatiaoui, S. Lahiri, B. Lommel, M. Maiti, A. K. Mistry, C. Mokry, K. J. Moody, Y. Nagame, J. P. Omtvedt, P. Papadakis, V. Pershina, D. Rudolph, L. Samiento, T. Sato, M. Schädel, P. Scharrer, B. Schausten, D. A. Shaughnessy, J. Steiner, P. Thörle-Pospiech, A. Toyoshima, N. Trautmann, K. Tsukada, J. Uusitalo, K.-O. Voss, A. Ward, M. Wegrzecki, N. Wiehl, E. Williams, V. Yakusheva, On the adsorption and reactivity of element 114, flerovium, *Frontiers in Chemistry* 10 (Aug. 2022). doi:10.3389/fchem.2022.976635.
- [30] Y. Oganessian, V. Utyonkov, Superheavy nuclei from 48ca-induced reactions, *Nuclear Physics A* 944 (2015) 62–98. doi:10.1016/j.nuclphysa.2015.07.003.
- [31] S. Hofmann, D. Ackermann, S. Antalic, H. G. Burkhard, V. F. Comas, R. Dressler, Z. Gan, S. Heinz, J. A. Heredia, F. P. Heßberger, J. Khuyagbaatar, B. Kindler, I. Kojouharov, P. Kuusiniemi, M. Leino, B. Lommel, R. Mann, G. Münzenberg, K. Nishio, A. G. Popeko, S. Saro, H. J. Schött, B. Streicher, B. Sulignano, J. Uusitalo, M. Venhart, A. V. Yeremin, The reaction $48\text{ca} + 238\text{u} \rightarrow 286112^*$ studied at the gsi-ship, *The European Physical Journal A* 32 (3) (2007) 251–260. doi:10.1140/epja/i2007-10373-x.
- [32] J. Khuyagbaatar, A. Yakushev, C. E. Düllmann, D. Ackermann, L.-L. Andersson, M. Asai, M. Block, R. A. Boll, H. Brand, D. M. Cox, M. Dasgupta, X. Derckx, A. Di Nitto, K. Eberhardt, J. Even, M. Evers, C. Fahlander, U. Forsberg, J. M. Gates, N. Gharibyan, P. Golubev, K. E. Gregorich, J. H. Hamilton, W. Hartmann, R.-D. Herzberg, F. P. Heßberger, D. J. Hinde, J. Hoffmann, R. Hollinger, A. Hübner, E. Jäger, B. Kindler, J. V. Kratz, J. Krier, N. Kurz, M. Laatiaoui, S. Lahiri, R. Lang, B. Lommel, M. Maiti, K. Miernik, S. Minami, A. Mistry, C. Mokry, H. Nitsche, J. P. Omtvedt, G. K. Pang, P. Papadakis, D. Renisch, J. Roberto, D. Rudolph, J. Runke, K. P. Rykaczewski, L. G. Sarmiento, M. Schädel, B. Schausten, A. Semchenkov, D. A. Shaughnessy, P. Steinegger, J. Steiner, E. E. Tereshatov, P. Thörle-Pospiech, K. Tinschert, T. Torres De Heidenreich, N. Trautmann, A. Türler, J. Uusitalo, D. E. Ward, M. Wegrzecki, N. Wiehl, S. M. Van Cleve, V. Yakusheva, Fusion reaction $ca48+bk249$ leading to formation of the element ts ($z=117$), *Physical Review C* 99 (5) (2019) 054306. doi:10.1103/physrevc.99.054306.
- [33] Y. T. Oganessian, V. K. Utyonkov, Y. V. Lobanov, F. S. Abdullin, A. N. Polyakov, R. N. Sagaidak, I. V. Shirokovsky, Y. S. Tsyganov, A. A. Voinov, G. G. Gulbekian, S. L. Bogomolov, B. N. Gikal, A. N. Mezentsev, S. Iliev, V. G. Subbotin, A. M.

- Sukhov, K. Subotic, V. I. Zagrebaev, G. K. Vostokin, M. G. Itkis, K. J. Moody, J. B. Patin, D. A. Shaughnessy, M. A. Stoyer, N. J. Stoyer, P. A. Wilk, J. M. Kenneally, J. H. Landrum, J. F. Wild, R. W. Loughheed, Synthesis of the isotopes of elements 118 and 116 in the $^{249}\text{Cf} + ^{245}\text{Cm} \rightarrow ^{118}\text{Og} + ^{4}\text{He}$ fusion reactions, *Physical Review C* 74 (4) (2006) 044602. doi:10.1103/physrevc.74.044602.
- [34] B. Lommel, C. E. Düllmann, B. Kindler, D. Renisch, Status and developments of target production for research on heavy and superheavy nuclei and elements, *The European Physical Journal A* 59 (2) (Feb. 2023). doi:10.1140/epja/s10050-023-00919-7.
- [35] J. Roberto, C. Alexander, R. Boll, J. Burns, J. Ezold, L. Felker, S. Hogle, K. Rykaczewski, Actinide targets for the synthesis of super-heavy elements, *Nuclear Physics A* 944 (2015) 99–116. doi:10.1016/j.nuclphysa.2015.06.009.
- [36] J. B. Roberto, M. Du, J. G. Ezold, S. L. Hogle, J. Moon, K. Myhre, K. P. Rykaczewski, Actinide targets for the synthesis of superheavy nuclei, *The European Physical Journal A* 59 (12) (Dec. 2023). doi:10.1140/epja/s10050-023-01144-y.
- [37] C. E. Düllmann, E. Artes, A. Dragoun, R. Haas, E. Jäger, B. Kindler, B. Lommel, K.-M. Mangold, C.-C. Meyer, C. Mokry, F. Munnik, M. Rapps, D. Renisch, J. Runke, A. Seibert, M. Stöckl, P. Thörle-Pospiech, C. Trautmann, N. Trautmann, A. Yakushev, Advancements in the fabrication and characterization of actinide targets for superheavy element production, *Journal of Radioanalytical and Nuclear Chemistry* 332 (5) (2022) 1505–1514. doi:10.1007/s10967-022-08631-4.
- [38] J. Runke, C. E. Düllmann, K. Eberhardt, P. A. Ellison, K. E. Gregorich, S. Hofmann, E. Jäger, B. Kindler, J. V. Kratz, J. Krier, B. Lommel, C. Mokry, H. Nitsche, J. B. Roberto, K. P. Rykaczewski, M. Schädel, P. Thörle-Pospiech, N. Trautmann, A. Yakushev, Preparation of actinide targets for the synthesis of the heaviest elements, *Journal of Radioanalytical and Nuclear Chemistry* 299 (2) (2013) 1081–1084. doi:10.1007/s10967-013-2616-6.
- [39] P. Hansen, The conditions for electrodeposition of insoluble hydroxides at a cathode surface: A theoretical investigation, *Journal of Inorganic and Nuclear Chemistry* 12 (1–2) (1959) 30–37. doi:10.1016/0022-1902(59)80089-0.
- [40] W. Parker, R. Falk, Molecular plating: A method for the electrolytic formation of thin inorganic films, *Nuclear Instruments and Methods* 16 (1962) 355–357. doi:10.1016/0029-554x(62)90142-8.
- [41] J. P. Greene, I. Ahmad, Molecular plating of actinides on thin backings, *Nuclear Instruments and Methods in Physics Research Section A: Accelerators,*

- Spectrometers, Detectors and Associated Equipment 590 (1–3) (2008) 131–133. doi:[10.1016/j.nima.2008.02.076](https://doi.org/10.1016/j.nima.2008.02.076).
- [42] R. Haas, T. Kieck, D. Budker, C. E. Düllmann, K. Groot-Berning, W. Li, D. Renisch, F. Schmidt-Kaler, F. Stopp, A. Viatkina, Development of a recoil ion source providing slow th ions including 229(m)th in a broad charge state distribution, *Hyperfine Interactions* 241 (1) (Feb. 2020). doi:[10.1007/s10751-019-1688-2](https://doi.org/10.1007/s10751-019-1688-2).
- [43] A. Vascon, N. Wiehl, T. Reich, J. Drebert, K. Eberhardt, C. Düllmann, The performance of thin layers produced by molecular plating as α -particle sources, *Nuclear Instruments and Methods in Physics Research Section A: Accelerators, Spectrometers, Detectors and Associated Equipment* 721 (2013) 35–44. doi:[10.1016/j.nima.2013.04.050](https://doi.org/10.1016/j.nima.2013.04.050).
- [44] W. Loveland, J. D. Baker, Target preparation for the fission tpc, *Journal of Radioanalytical and Nuclear Chemistry* 282 (2) (2009) 361–363. doi:[10.1007/s10967-009-0146-z](https://doi.org/10.1007/s10967-009-0146-z).
- [45] W. Loveland, High quality actinide targets, *Journal of Radioanalytical and Nuclear Chemistry* 307 (3) (2015) 1591–1594. doi:[10.1007/s10967-015-4337-5](https://doi.org/10.1007/s10967-015-4337-5).
- [46] K. Eberhardt, W. Bröchle, C. Düllmann, K. Gregorich, W. Hartmann, A. Hübner, E. Jäger, B. Kindler, J. Kratz, D. Liebe, B. Lommel, H.-J. Maier, M. Schädel, B. Schausten, E. Schimpf, A. Semchenkov, J. Steiner, J. Szerypo, P. Thörle, A. Türler, A. Yakushev, Preparation of targets for the gas-filled recoil separator tasca by electrochemical deposition and design of the tasca target wheel assembly, *Nuclear Instruments and Methods in Physics Research Section A: Accelerators, Spectrometers, Detectors and Associated Equipment* 590 (1–3) (2008) 134–140. doi:[10.1016/j.nima.2008.02.069](https://doi.org/10.1016/j.nima.2008.02.069).
- [47] J. P. Greene, R. V.F. Janssens, I. Ahmad, Preparation of actinide targets by molecular plating for coulomb excitation studies at atlas, *Nuclear Instruments and Methods in Physics Research Section A: Accelerators, Spectrometers, Detectors and Associated Equipment* 438 (1) (1999) 119–123. doi:[10.1016/s0168-9002\(99\)00668-3](https://doi.org/10.1016/s0168-9002(99)00668-3).
- [48] A. Vascon, S. Santi, A. Isse, T. Reich, J. Drebert, H. Christ, C. Düllmann, K. Eberhardt, Elucidation of constant current density molecular plating, *Nuclear Instruments and Methods in Physics Research Section A: Accelerators, Spectrometers, Detectors and Associated Equipment* 696 (2012) 180–191. doi:[10.1016/j.nima.2012.08.072](https://doi.org/10.1016/j.nima.2012.08.072).
- [49] K. Eberhardt, C. E. Düllmann, R. Haas, C. Mokry, J. Runke, P. Thörle-Pospiech, N. Trautmann, Actinide targets for fundamental research in nuclear physics,

in: AIP Conference Proceedings, Vol. 1962, Author(s), 2018, p. 030009. doi: [10.1063/1.5035526](https://doi.org/10.1063/1.5035526).

- [50] G. Sibbens, A. Göök, D. Lewis, A. Moens, S. Oberstedt, D. Vanleeuw, R. Wynants, M. Zampella, Target preparation for neutron-induced reaction measurements, EPJ Web of Conferences 229 (2020) 04003. doi:[10.1051/epjconf/202022904003](https://doi.org/10.1051/epjconf/202022904003).
- [51] S. Sadi, A. Paulenova, P. Watson, W. Loveland, Growth and surface morphology of uranium films during molecular plating, Nuclear Instruments and Methods in Physics Research Section A: Accelerators, Spectrometers, Detectors and Associated Equipment 655 (1) (2011) 80–84. doi:[10.1016/j.nima.2011.06.025](https://doi.org/10.1016/j.nima.2011.06.025).
- [52] W. Parker, H. Bildstein, N. Getoff, Molecular plating iii the rapid preparation of radioactive reference samples, Nuclear Instruments and Methods 26 (1964) 314–316. doi:[10.1016/0029-554x\(64\)90095-3](https://doi.org/10.1016/0029-554x(64)90095-3).
- [53] N. Getoff, H. Bildstein, Molecular plating, iv a rapid method for the electrodeposition of plutonium, Nuclear Instruments and Methods 36 (1965) 173–175. doi:[10.1016/0029-554x\(65\)90420-9](https://doi.org/10.1016/0029-554x(65)90420-9).
- [54] M. Ramaniah, R. Singh, S. Awasthi, S. Prakash, Studies on electrodeposition of actinide elements from non-aqueous medium, The International Journal of Applied Radiation and Isotopes 26 (11) (1975) 648–650. doi:[10.1016/0020-708x\(75\)90019-8](https://doi.org/10.1016/0020-708x(75)90019-8).
- [55] C.-C. Meyer, A. Dragoun, C. Düllmann, R. Haas, E. Jäger, B. Kindler, B. Lommel, A. Prosvetov, M. Rapps, D. Renisch, P. Simon, M. Tomut, C. Trautmann, A. Yakushev, Chemical conversions in lead thin films induced by heavy-ion beams at coulomb barrier energies, Nuclear Instruments and Methods in Physics Research Section A: Accelerators, Spectrometers, Detectors and Associated Equipment 1028 (2022) 166365. doi:[10.1016/j.nima.2022.166365](https://doi.org/10.1016/j.nima.2022.166365).
- [56] A. Stolarz, Target preparation for research with charged projectiles, Journal of Radioanalytical and Nuclear Chemistry 299 (2) (2013) 913–931. doi:[10.1007/s10967-013-2652-2](https://doi.org/10.1007/s10967-013-2652-2).
- [57] E. Jäger, H. Brand, C. E. Düllmann, J. Khuyagbaatar, J. Krier, M. Schädel, T. Torres, A. Yakushev, High intensity target wheel at tasca: target wheel control system and target monitoring, Journal of Radioanalytical and Nuclear Chemistry 299 (2) (2013) 1073–1079. doi:[10.1007/s10967-013-2645-1](https://doi.org/10.1007/s10967-013-2645-1).
- [58] K. J. Moody, Synthesis of Superheavy Elements, Springer Berlin Heidelberg, 2013, pp. 1–81. doi:[10.1007/978-3-642-37466-1_1](https://doi.org/10.1007/978-3-642-37466-1_1).

- [59] S. N. Dmitriev, A. G. Popeko, High-power radioactive targets as one of the key problems in further development of the research program on synthesis of new superheavy elements, *Journal of Radioanalytical and Nuclear Chemistry* 305 (3) (2015) 927–933. doi:10.1007/s10967-014-3920-5.
- [60] J. F. Ziegler, M. Ziegler, J. Biersack, Srim – the stopping and range of ions in matter (2010), *Nuclear Instruments and Methods in Physics Research Section B: Beam Interactions with Materials and Atoms* 268 (11–12) (2010) 1818–1823. doi:10.1016/j.nimb.2010.02.091.
- [61] A. Popeko, A. Yeregin, O. Malyshev, V. Chepigina, A. Isaev, Y. Popov, A. Svirikhin, K. Haushild, A. Lopez-Martens, K. Rezyunkina, O. Dorvaux, Separator for heavy element spectroscopy – velocity filter shells, *Nuclear Instruments and Methods in Physics Research Section B: Beam Interactions with Materials and Atoms* 376 (2016) 140–143. doi:10.1016/j.nimb.2016.03.045.
- [62] D. Kaji, K. Morimoto, N. Sato, A. Yoneda, K. Morita, Gas-filled recoil ion separator garis-ii, *Nuclear Instruments and Methods in Physics Research Section B: Beam Interactions with Materials and Atoms* 317 (2013) 311–314. doi:10.1016/j.nimb.2013.05.085.
- [63] Y. Oganessian, V. Utyonkov, A. Popeko, D. Soloviyev, F. Abdullin, S. Dmitriev, D. Ibadullayev, M. Itkis, N. Kovrizhnykh, D. Kuznetsov, O. Petrushkin, A. Podshibiakin, A. Polyakov, R. Sagaidak, L. Schlattauer, I. Shirokovsky, V. Shubin, M. Shumeiko, Y. Tsyganov, A. Voinov, V. Subbotin, V. Bekhterev, N. Belykh, O. Chernyshev, K. Gikal, G. Ivanov, A. Khalkin, V. Konstantinov, N. Osipov, S. Paschenko, A. Protasov, V. Semin, V. Sorokoumov, K. Sychev, V. Verevochkin, B. Yakovlev, S. Antoine, W. Beeckman, P. Jehanno, M. Yavor, A. Shcherbakov, K. Rykaczewski, T. King, J. Roberto, N. Brewer, R. Grzywacz, Z. Gan, Z. Zhang, M. Huang, H. Yang, Dgfrs-2—a gas-filled recoil separator for the dubna super heavy element factory, *Nuclear Instruments and Methods in Physics Research Section A: Accelerators, Spectrometers, Detectors and Associated Equipment* 1033 (2022) 166640. doi:10.1016/j.nima.2022.166640.
- [64] C.-C. Meyer, E. Artes, M. Bender, J. Brötz, C. E. Düllmann, C. Haese, E. Jäger, B. Kindler, B. Lommel, M. Major, M. Rapps, D. Renisch, C. Trautmann, A. Yakushev, Fabrication, swift heavy ion irradiation, and damage analysis of lanthanide targets, *Radiochimica Acta* 111 (11) (2023) 801–815. doi:10.1515/ract-2023-0197.
- [65] C. Stodel, M. Toulemonde, C. Fransen, B. Jacquot, E. Clément, G. Frémont, M. Michel, C. Dufour, “thermal spike” model applied to thin targets irradiated with swift heavy ion beams at few mev/u, *EPJ Web of Conferences* 229 (2020) 05001. doi:10.1051/epjconf/202022905001.

- [66] D. Mayorov, E. Tereshatov, T. Werke, M. Frey, C. Folden, Heavy-ion beam induced effects in enriched gadolinium target films prepared by molecular plating, *Nuclear Instruments and Methods in Physics Research Section B: Beam Interactions with Materials and Atoms* 407 (2017) 256–264. doi:10.1016/j.nimb.2017.07.012.
- [67] N. T. Brewer, V. K. Utyonkov, K. P. Rykaczewski, Y. T. Oganessian, F. S. Abdullin, R. A. Boll, D. J. Dean, S. N. Dmitriev, J. G. Ezold, L. K. Felker, R. K. Grzywacz, M. G. Itkis, N. D. Kovrizhnykh, D. C. McInturff, K. Miernik, G. D. Owen, A. N. Polyakov, A. G. Popeko, J. B. Roberto, A. V. Sabel'nikov, R. N. Sagaidak, I. V. Shirokovsky, M. V. Shumeiko, N. J. Sims, E. H. Smith, V. G. Subbotin, A. M. Sukhov, A. I. Svirikhin, Y. S. Tsyganov, S. M. Van Cleve, A. A. Voinov, G. K. Vostokin, C. S. White, J. H. Hamilton, M. A. Stoyer, Search for the heaviest atomic nuclei among the products from reactions of mixed-cf with a ca48 beam, *Physical Review C* 98 (2) (2018) 024317. doi:10.1103/physrevc.98.024317.
- [68] I. Usoltsev, R. Eichler, G. Vostokin, A. Sabel'nikov, N. Aksenov, Y. Albin, G. Bozhikov, V. Chepigin, S. Dmitriev, V. Lebedev, O. Malyshev, O. Petrushkin, D. Piguet, G. Starodub, A. Svirikhin, A. Türler, A. Yeremin, Preparation and high intensity heavy ion irradiation tests of intermetallic 243am/pd targets, *Nuclear Instruments and Methods in Physics Research Section B: Beam Interactions with Materials and Atoms* 318 (2014) 297–305. doi:10.1016/j.nimb.2013.10.019.
- [69] P. A. Helmke, Neutron activation analysis (Feb. 1982). doi:10.2134/agronmonogr9.2.2ed.c4.
- [70] K. Eberhardt, C. Geppert, The research reactor triga mainz – a strong and versatile neutron source for science and education, *Radiochimica Acta* 107 (7) (2019) 535–546. doi:10.1515/ract-2019-3127.
- [71] W. Zhou, R. Apkarian, Z. L. Wang, D. Joy, *Fundamentals of Scanning Electron Microscopy (SEM)*, Springer New York, 2006, pp. 1–40. doi:10.1007/978-0-387-39620-0_1.
- [72] S. G. Lipson, H. S. Lipson, D. S. Tannhauser (Eds.), *Optik*, Springer-Lehrbuch, Springer, Berlin, 1997, lizenzpflichtig.
- [73] J. Goldstein, *Scanning electron microscopy and X-ray microanalysis*, fourth edition Edition, Springer, New York, NY, U.S.A., 2018.
- [74] A. Ul-Hamid, *A Beginners' Guide to Scanning Electron Microscopy*, Springer.

- [75] A. J. Garratt-Reed, D. C. Bell, Energy-dispersive X-ray analysis in the electron microscope, 1st Edition, no. 49 in Microscopy handbooks, BIOS Scientific Publ., Oxford, 2003, includes bibliographical references and index.
- [76] B. Schrader, Infrared and Raman Spectroscopy, 1st Edition, John Wiley Sons, Incorporated, Berlin, 1995, description based on publisher supplied metadata and other sources.
- [77] C. N. Banwell, E. M. McCash, Fundamentals of molecular spectroscopy, 4th Edition, MacGraw-Hill, London [u.a.], 1997, literaturangaben.
- [78] B. A. Nogueira, C. Castiglioni, Raman spectroscopy of crystalline materials and nanostructures, Crystals 14 (3) (2024) 251. doi:10.3390/cryst14030251.
- [79] A. Krylov, Raman spectroscopy of crystals, Crystals 10 (11) (2020) 981. doi:10.3390/cryst10110981.
- [80] P. V. der Heide, X-ray photoelectron spectroscopy, Wiley-Blackwell, Hoboken, N.J, 2012, includes index.
- [81] G. Greczynski, L. Hultman, X-ray photoelectron spectroscopy: Towards reliable binding energy referencing, Progress in Materials Science 107 (2020) 100591. doi:10.1016/j.pmatsci.2019.100591.
- [82] J. Cookson, T. Conlon, Mev ion-beam analysis, Journal of Research of the National Bureau of Standards 93 (3) (1988) 473. doi:10.6028/jres.093.123.
- [83] C. Jeynes, J. L. Colaux, Thin film depth profiling by ion beam analysis, The Analyst 141 (21) (2016) 5944–5985. doi:10.1039/c6an01167e.
- [84] M. A. Nastasi, Ion beam analysis, Taylor Francis,, Boca Raton, 2015.
- [85] K. Yasuda, Time-of-flight erda for depth profiling of light elements, Quantum Beam Science 4 (4) (2020) 40. doi:10.3390/qubs4040040.

Chapter **2**

Publication I: The process of molecular plating and the characteristics of the produced thin films – What we have learned in 60 years and what is still unknown

The following article was published as conference paper in *EPJ Web of Conferences*, volume 285 in 2023. It reviews the progress of thin film preparation by molecular plating technique, the understanding of the process and the chemical composition of the produced thin films using different methods, like microscopy, γ - and α -spectroscopy infrared spectroscopy and more.

2.1 Own contributions

The references for this article were curated and put into context. Some targets and pictures were self-made. The paper was written completely self-directed.

2.2 Publication

The process of molecular plating and the characteristics of the produced thin films – What we have learned in 60 years and what is still unknown

Ernst Artes^{1,2,3*}, Christoph E. Düllmann^{1,2,3}, Carl-Christian Meyer^{1,2}, and Dennis Renisch^{1,2}

¹Johannes Gutenberg Universität Mainz, 55099 Mainz, Germany

²Helmholtz-Institut Mainz, 55099 Mainz, Germany

³GSI Helmholtzzentrum für Schwerionenforschung GmbH, 64291 Darmstadt, Germany

Abstract. Molecular plating is a well-established and widely used method for producing thin films of various elements, which are used in variety of nuclear physics applications. Sixty years have passed since the method was established, and some insights into the chemical process underlying the method and the composition of the thin films have been gained. A brief overview of what has been learned about molecular plating since its introduction and the methods applied in the characterization of molecular plated thin films is given here. Through various spectroscopic and microscopic methods, the process of molecular plating and the chemical composition are gradually being elucidated, albeit we still do not understand all aspects.

1 Introduction

The molecular plating (MP) method for the production of mechanically stable thin films of radioisotopes was introduced by Parker and Falk in 1962 [1]. In this method, a salt of the respective element was dissolved in a small volume of diluted acids, added to an organic solution, e.g., alcohols or acetone and then electrochemically deposited. Nowadays, a constant current density of $<1 \text{ mA/cm}^2$ over 1-2 h is applied. This results in high voltages of several hundred volts. MP produces uniform thin films with an even distribution of the deposited element. Such layers found widespread applications, e.g., as targets in ion beam experiments, as recoil sources, or as α -particle sources [3-12]. One example is the synthesis of superheavy elements (SHE), which can be produced in the nuclear fusion of a light projectile with a heavy target nuclide. All known isotopes of the elements with atomic number $Z \geq 113$ resulted from actinide-target based reactions [11]. Typical isotopes like ^{244}Pu , ^{248}Cm or ^{249}Bk are only available in small quantities, rendering production methods with high yields necessary. Therefore, MP has become the standard method for producing these targets [3,11,12]. For this application, the method works reliable up to film thicknesses of $\approx 800 \mu\text{g/cm}^2$, with yields of usually over 90 % [2,3,4]. While thicker films can be produced for various elements, the method becomes unreliable for actinide layers. Consequently, actinide films that are substantially thicker have not been reported. Although molecular plating was introduced in 1962 [1] and has been widely used since, neither the mechanism of the deposition process, nor the

exact composition of the resulting thin layer is fully understood. Parker and Falk coined the method “molecular plating” because they assumed at the time that the provided salts, e.g., the nitrates or chlorides, would be deposited as thin films [1]. Nowadays, it is well known that this is not the case. Many different analytical methods [2,12-18] have shown that the chemical species of the deposited element in the thin film differs from the species in the solution. Over time, mostly microscopic and also some spectroscopic methods have been used to analyse the thin films produced by MP and to understand how the process works, see e.g., [2,4,18,19]. The elucidation of the process and the layer properties appear necessary to produce improved films, which e.g., exceed the limitations in the layer thicknesses, as it appears desirable for, e.g., SHE production [4].

2 Methods

Many methods focused on the film’s morphology, which led to the use of several microscopic methods, such as scanning electron microscopy (SEM) [6,17,21,22] and atomic force microscopy (AFM) [2,16,17]. Radiographic imaging (RI) [18,23,24] exploits the radioactive character of actinides to provide information on the spatial distribution of the radioisotope. Alpha and gamma spectroscopy [8,9,21,23,24] provide further quantitative information.

Neutron activation analysis (NAA) [25] can be used to activate inactive samples or long-lived isotopes,

* Corresponding author: erartes@uni-mainz.de

making gamma measurements possible that reveal the amount of deposited material.

With SEM, energy-dispersive X-ray spectroscopy (EDS) was also employed early on to determine the elemental composition of the thin films. [13,15,19,26]. However, these methods are all unable to provide information on the chemical composition of the thin films, which is why spectroscopic methods, like IR, Raman, X-ray diffraction (XRD), X-ray photoelectron spectroscopy (XPS), or ion beam spectroscopy like elastic recoil detection analysis (ERDA), Rutherford backscattering (RBS) or proton-induced X-ray emission (PIXE), were also used later [2,13,15,16,19,27-29].

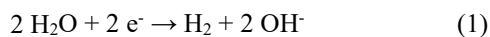
Raman and IR measurements were made early on [15,19], but not recently pursued further. These methods allow determining the chemical composition. Both methods are complementary as the vibrations of the molecules are either IR or Raman active. Further information can be gained by XPS [2,16,17], which provides information on the chemical environment of the element. XRD measurements were used to investigate the crystalline composition of the films [13,14] to reach conclusions about the crystalline structure.

Most recently, various ion beam analyses have also been applied to molecular plated thin films. One such method is ERDA [4], which is particularly well suited for detecting light elements from lithium up to chlorine in the thin film. Complementary to this, RBS was also used [12,28,29] to allow drawing conclusions about the elemental composition of the films.

PIXE was also measured in combination with RBS [4]. In PIXE, a proton beam induces X-rays in the sample to obtain further information about the film. It can also be used as an imaging method, which allows both microscopic and spectroscopic information to be obtained simultaneously.

3 Elucidation of the MP process

In 1959, even before MP was introduced, Hansen [30] had published a theory on electrochemical deposition from water or mixtures of water with alcohols or acetone. He suggested that water is reduced in the process, producing hydroxide ions that lead to basic precipitation of the actinides [19,30]:



In 1975, Ramaniah et al. [15] were able to determine through thermogravimetric, EDS and IR analyses that no nitrates were present in MP films. In particular, the IR analyses of uranium films showed a U-O stretching vibration of UO_2^{2+} , which led to the assumption that uranium was deposited as an oxide or hydroxide. In addition, by adding phenolphthalein, the presence of water was observed in the isopropyl alcoholic solution and a hydroxide-rich layer was observed at the cathode [15]. Sadi et al. [19] proposed the chemical composition to be $\text{UO}_2(\text{OH})_2$, based on the atomic ratios determined by EDS measurements. They proposed the hydroxide ions to act as bridge ligands between the uranyl ions as

a possible structure in the thin film. With more analytical investigations, it became clear that the MP process is even more complex than a hydroxide precipitation, and the thin films contain more than only oxide and hydroxide species [2,14-17,19,27].

4 Elucidation of the properties of MP films

With the help of microscopic methods, the thin layers could be examined in detail. Since the focus was particularly on the deposition of uranium and plutonium in the beginning, the activity of these elements was used to take radiographic images of the samples [18]. These images showed that the activity of the films was particularly homogeneously distributed, which is visible in Fig. 1.

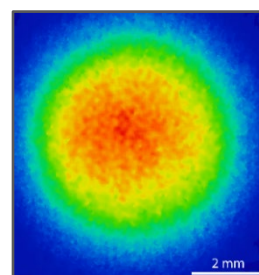


Fig. 1. A radiographic image (RI) of a terbium thin film, produced by MP, with a layer thickness of 500(50) $\mu\text{g}/\text{cm}^2$. Natural terbium was neutron activated in the TRIGA Mainz research reactor [25] before plating.

Radiographic images also made it possible to identify the influence of various experimental parameters, such as cell design or electrode shape, on the deposition. In this way, information could be obtained about the influence of the geometry of the anode, i.e., the counter-electrode, on the distribution of the activity in the thin film [23,24,31,32]. Initial experiments also show that stirring with a rotating anode or an ultrasonic stirrer during deposition can lead to shorter deposition times by forcing convection in the solution. However, the choice of parameters is crucial [7,23,24]. Due to the activity of uranium and thorium isotopes, alpha and gamma spectra of samples produced by molecular plating could also be taken, so that the deposition yield could be optimized by adjusting the deposition time and the applied current [1-3,18-23,31,32].

The usage of a SEM with a spatial resolution of $<1 \mu\text{m}$ [4] made it clear that the molecular plated thin films were not homogeneous and closed surfaces as was inferred from radiographic images, which have a spatial resolution of $>100 \mu\text{m}$ [33], but consisted of many cracks and tiles, referred to as “mudcracking” [1,4,20,26,27]. Pictures of such tiles are visible in Fig. 2. Today, SEM measurements are a standard method to characterise molecular-plated thin films in higher resolution than a usual light microscope [4,16,18,21].

Later Liebe et al. [13] confirmed the absence of nitrogen, as first reported by Ramaniah et al. [15], in the thin MP films by EDS measurements. Therefore, nitrates cannot be present in the thin films, which

definitely refuted Parker and Falk's theory of salt re-deposition [1].

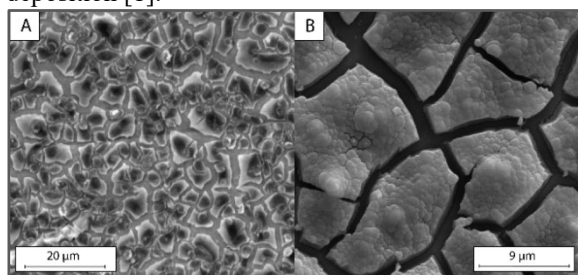


Fig 2. SEM pictures of lanthanide thin films produced by molecular plating. A) Erbium thin film. B) Silver sputtered lanthanum thin film. Both thin films have a layer thickness of 500(50) $\mu\text{g}/\text{cm}^2$.

Vascon et al. [16] were able to show by AFM measurements in solution that cracks are not present in the native film during the MP process, but form only after removal of the solvent, during drying after deposition. Fig. 3 shows an exemplary AFM image of a Tb thin film, after the drying process. They could also show that different solvents impact the quality of the thin film [16] and explained this by the fact that different solvents have different boiling points and different vapour pressures. It is assumed that residues of the solvents are present in the film after deposition. Evaporation during drying leads to rupturing of the films. They were able to observe that deposition from DMF (boiling point: 153 °C), leads to less mudcracking than deposition from isobutanol (boiling point: 108 °C).

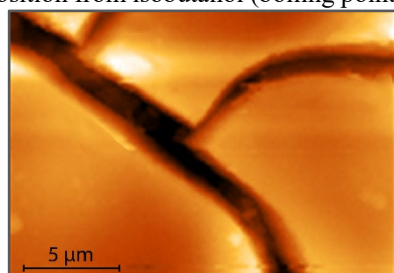


Fig 3. An AFM picture of a terbium thin film with a layer thickness of 100(10) $\mu\text{g}/\text{cm}^2$, which was produced by molecular plating.

Vascon et al. [2,16,17] also found out with the help of XPS measurements that the produced thin films not only contained oxides and hydroxides, but also organic components. Besides adventitious carbon contamination, aliphatic and aromatic carbon was found [2,16,17]. It did not disappear even after sputtering with 4 kV Ar^+ -ions for 10 min. They thus assumed that the carbon was a constituent of the thin film. They attributed the signals to the presence of residue solvents, carbonates and/or carboxylates, which was assumed to form by the electrolysis of the used solvents. Further XPS measurements also showed that the lanthanide is not reduced in the process of plating but remains in the +III oxidation state [2,13,15-17].

In 2016, Choi and Chung [13] did XRD measurements on molecular-plated thin films to understand what happens to the thin films when they are calcinated. They identified, next to oxides and hydroxides, also predominantly oxycarbonates after a short calcination time, further proving that significant

amounts of organic molecules were present in the molecular plated thin films.

Mayorov et al. [26] investigated Gd MP thin films after irradiation with ion beams ($^{48}\text{Ca}^{7+}$ with 3.8 MeV/u and 4.5×10^{14} ions/ cm^2 and $^{45}\text{Sc}^{6+}$ with 4.7 MeV/u and 4.0×10^{15} ions/ cm^2). In the XRD measurements, the only visible compound before and after the irradiation was Gd_2O_3 . The EDS spectra showed, in addition to gadolinium, also carbon which they attributed to carboxylates because of this prior assignment by Vascon et al. [2,16,17]. Mayorov et al. assumed that organic residues evaporated during the irradiation leading to a decreased carbon signal. The SEM picture showed that the typical cracked film became smoother and thinner after the irradiation, closing the cracks, which were visible before [26].

Although much has been learned about the MP method and the produced thin films, much is still unknown. It is not still clear why high voltages of several hundred volts are necessary for this method to work sufficiently well. It is also unknown what happens to most of the current that is applied during the MP process, and whether this loss of charge has any influence [2]. It is also unknown why the layer thickness is limited to 800 $\mu\text{g}/\text{cm}^2$ and how this limit can be exceeded [3,4]. Although individual components such as oxides, hydroxides, carbonates, and carboxylates have been identified in the thin films [2,7,12-17,19,27], the ratios of the individual components to each other are still unknown. It is therefore not yet possible to determine a sum formula for the composition of the film.

5 Conclusion

Since the establishment of molecular plating by Parker and Falk [1] 60 years ago, knowledge about the method has been gained via many different methods. Via different microscopic methods, like RI, SEM and AFM, and different spectroscopic methods, like alpha and gamma spectroscopy, EDS, XPS, XRD, RBS, IR, and Raman spectroscopy [2,4,7,13-17,19,27], a more precise understanding of the process of MP and of the chemical composition of the thin films was obtained.

It became clear that no nitrates or chlorides are deposited, but that the thin film consisted mainly of oxides and hydroxides. In addition, carboxylates and carbonates are also present [2,16,17]. It was also shown that the choice of solvent during deposition has an influence on the film quality [16].

By exposing MP films to heavy ion beams, they are further modified, making them thinner and closing the cracks [26].

We still do not fully know, what the stoichiometric composition of MP films is and what influences the success or failure of a deposition [4,16,21,22]. In addition, it is still not understood, why the thicknesses of the produced thin films are limited and how to overcome this obstacle [3,4].

Therefore, further studies of the MP process and of the resulting layers are necessary, alongside further development to improve the method for future applications. In this way, further systematic studies

could be carried out to understand the influence of CO₂ and water on the MP process.

We acknowledge funding from the German Federal Ministry for Research and Education (project 05P21UMFN2). The contribution of Sebastian Herz (JGU Mainz) is appreciated.

References

1. W. Parker, R. Falk, Nucl. Instr. And Meth. **16**, 355-357 (1962)
2. A. Vascon, S. Santi, A. A. Isse, T. Reich, J. Drebert, H. Christ, Ch. E. Düllmann, K. Eberhardt, Nucl. Instrum. Methods. Phys. Res. A, **696**, 163-175 (2012)
3. K. Eberhardt, W. Brüche, Ch. E. Düllmann, K. E. Gregorich, W. Hartmann, A. Hübner, E. Jäger, B. Kindler, J. V. Kratz, D. Liebe, B. Lommel, H.-J. Maier, M. Schädel, B. Schausten, E. Schimpf, A. Semchenkov, J. Steiner, J. Szerypo, P. Thörle, A. Türler, A. Yakushev, Nucl. Instrum. Methods. Phys. Res. A, **590**, 134-140 (2008)
4. Ch. E. Düllmann, E. Artes, A. Dragoun, R. Haas, E. Jäger, B. Kindler, B. Lommel, K.-M. Mangold, C.-C. Meyer, C. Mokry, F. Munnik, M. Rapps, D. Renisch, J. Runke, A. Seibert, M. Stöckl, P. Thörle-Pospiech, C. Trautmann, N. Trautmann, A. Yakushev, J. Radioanal. Nucl. Chem. (2022) <https://doi.org/10.1007/s10967-022-08631-4>
5. J. Runke, Ch. E. Düllmann, K. Eberhardt, P. A. Ellison, K. E. Gregorich, S. Hofmann, E. Jäger, B. Kindler, J. V. Kratz, J. Krier, B. Lommel, C. Mokry, H. Nitsche, J. B. Roberto, K. P. Rykaczewski, M. Schädel, P. Thörle-Pospiech, N. Trautmann, A. Yakushev, J. Radioanal. Nucl. Chem. **299**, 1081-1084 (2014)
6. B. Lommel, Ch. E. Düllmann, B. Kindler, D. Renisch, Eur. Phys. J. A, (accepted for publication)
7. W. Loveland, J. D. Baker, J. Radioanal. Nucl. Chem **282**, 361-363 (2009)
8. W. Loveland J. Radioanal. Nucl. Chem **307**, 1591-1594 (2016)
9. A. Vascon, Ch. E. Düllmann, K. Eberhardt, B. Kindler, B. Lommel, J. Runke, Nucl. Instrum. Methods. Phys. Res. A **655**, 72-79 (2011)
10. J. P. Greene, R. V. F. Janssens, I. Ahmad, Nucl. Instrum. Methods. Phys. Res. A **438**, 119-123 (1999)
11. R. Haas, T. Kieck, D. Budker, Ch. E. Düllmann, K. Groot-Berning, W. Li, D. Renisch, F. Schmidt-Kaler, F. Stopp, A. Viatkina, Hyperfine Interactions **241**, 25 (2020)
12. R. Haas, M. Hufnagel, R. Abrosimov, Ch. E. Düllmann, D. Krupp, C. Mokry, D. Renisch, J. Runke, U. W. Scherer, Radiochim. Acta **108**, 923-941 (2018)
13. D. Liebe, K. Eberhardt, W. Hartmann, T. Häger, A. Hübner, J. V. Kratz, B. Kindler, B. Lommel, p. Thörle, J. Steiner, Nucl. Instrum. Methods. Phys. Res. A, **590**, 145-150 (2008)
14. J. Choi, Y. H. Chung, Journal of Nanomaterials, **2016**, 5140219 (2016)
15. M. V. Ramaniah, R. J. Singh, S. K. Awasthi, S. Prakash, Int J Appl Radiat Isot **26**, 648-650 (1975)
16. A. Vascon, S. Santi, A. A. Isse, A. Kühnle, T. Reich, J. Drebert, K. Eberhardt, Ch. E. Düllmann Nucl. Instrum. Methods Phys. Res. A **714**, 163-175 (2013)
17. A. Vascon, J. Runke, N. Trautmann, B. Cremer, K. Eberhardt, Ch. E. Düllmann, Appl. Radiat. Isot. **95**, 36-43 (2015)
18. N. Getoff, H. Bildstein, Nucl. Instr. And Meth. **36**, 173-175 (1965)
19. S. Sadi, A. Paulenova, P. R. Watson, W. Loveland, Nucl. Instrum. Methods. Phys. Res. A, **655**, 80-84 (2011)
20. Ch. E. Düllmann, M. Block, F. P. Heßberger, J. Khuyagbaatar, B. Kindler, J. V. Kratz, B. Lommel, G. Münzenberg, V. Pershina, D. Renisch, M. Schädel, A. Yakushev, Radiochim. Acta, **110**, 417-439 (2022)
21. W. Parker, H. Bildstein, N. Getoff, Nucl. Instr. And Meth. **26**, 55-60 (1964)
22. W. Parker, H. Bildstein, N. Getoff, H. Fischer-Colbrie, H. Regal, Nucl. Instr. And Meth. **26**, 61-65 (1963)
23. M. T. Crespo, Appl. Radiat. Isot. **70**, 210-215 (2012)
24. H. Klemenčič, L. Benedik, Appl. Radiat. Isot. **68**, 1247-1251 (2010)
25. K. Eberhardt, C. Geppert, Radiochim. Acta **107**, 535-546 (2019)
26. D. A. Mayorov, E. E. Tereshatov, T. A. Werke, M. M. Frey, C. M. Folden III, Nucl. Instrum. Methods. Phys. Res. B **407**, 256-264 (2017)
27. C.-C. Meyer, A. Dragoun, Ch. E. Düllmann, R. Haas, E. Jäger, B. Kindler, B. Lommel, A. Prosvetov, M. Rapps, D. Renisch, P. Simon, M. Tomut, C. Trautmann, A. Yakushev, Nucl. Instrum. Methods. Phys. Res. A, **1028**, 166365 (2022)
28. O. A. Wasson, R. A. Schrack, Nucl. Instrum. Methods. Phys. Res. A **282**, 194-198 (1989)
29. C. Stodel, EPJ Web of Conferences **229**, 02001 (2020)
30. P. G. Hansen, J. Inorg. Nucl. Chem. **12**, 30-37 (1959)
31. Young Gun Ko, J. Radioanal. Nucl. Chem. **326**, 861-877 (2020)
32. C. Ingelbrecht, A. Moens, R. Eykens, A. Dean, Nucl. Instrum. Methods. Phys. Res. A, **397**, 34-38 (1997)
33. R. Haas, L. Lohse, Ch. E. Düllmann, K. Eberhardt, C. Mokry, J. Runke, Nucl. Instrum. Methods. Phys. Res. A, **874**, 43-49(2017)

Chapter **3**

Publication II: Influence of carbon dioxide and water in production of lanthanide thin films made by molecular plating

The following article was published as full article in *Radiochimica Acta*, in volume 113 pages 779-789 in 2025. It describes the influence of CO₂ and water on thin films produced by molecular plating. Molecular plating is a technique that is widely used in the production of thin films used for ion beam experiments.

3.1 Own contributions

The thin films were self-prepared. The ion beam experiments were planned. The post irradiation analysis at other institutes were organized and the data were evaluated. At last, the paper was written completely self-directed.

3.2 Publication

Ernst Artes*, Primiana Cavallo, Tobias Häger, Carl-Christian Meyer, Christoph Mokry, Dennis Renisch, Jörg Runke, Evgenia Schaffner, Alice Seibert, Christina Trautmann and Christoph E. Düllmann

Influence of carbon dioxide and water concentration on terbium thin films produced by Molecular Plating

<https://doi.org/10.1515/ract-2025-0021>

Received February 18, 2025; accepted June 20, 2025;

published online July 16, 2025

Abstract: Terbium and thulium thin films were produced by Molecular Plating under controlled conditions to elucidate a possible influence of water and carbon dioxide present in the plating solution. Platings were made in a glovebox with variable concentration of residual water and CO₂ in a controlled inert atmosphere to study the impact on the

quality of the produced thin films and on deposition yields. The morphology of the thin films was analyzed by scanning electron microscopy. The deposition yield was determined by neutron activation analysis at the research reactor TRIGA Mainz. Chemical analysis of the deposited layers was conducted using a combination of infrared, Raman and X-ray photoelectron spectroscopy. The Raman and IR spectra reveal the formation of hydroxides, oxides and carbonates. Water in the plating solution affects the quality of the thin films when its concentration exceeds 1 vol%. The presence of CO₂ leads to an increased carbonate content, which negatively influences the film quality.

***Corresponding author: Ernst Artes**, Department Chemie, Standort TRIGA – Johannes Gutenberg-Universität Mainz, 55128 Mainz, Germany; Helmholtz-Institut Mainz, 55128 Mainz, Germany; and GSI Helmholtzzentrum für Schwerionenforschung GmbH, 64291 Darmstadt, Germany, E-mail: erartes@uni-mainz.de. <https://orcid.org/0000-0003-2457-022X>

Primiana Cavallo and Evgenia Schaffner, Department Chemie, Standort TRIGA – Johannes Gutenberg-Universität Mainz, 55128 Mainz, Germany, E-mail: prcavall@students.uni-mainz.de (P. Cavallo), jenny.schaffner@web.de (E. Schaffner). <https://orcid.org/0009-0009-8904-9778> (P. Cavallo)

Tobias Häger, Institut für Geowissenschaften, Johannes Gutenberg-Universität Mainz, Johann-Joachim-Becher-Weg 2, 55128 Mainz, Germany, E-mail: haeger@uni-mainz.de

Carl-Christian Meyer, Christoph Mokry and Dennis Renisch, Department Chemie, Standort TRIGA – Johannes Gutenberg-Universität Mainz, 55128 Mainz, Germany; and Helmholtz-Institut Mainz, 55128 Mainz, Germany, E-mail: cmeyer02@uni-mainz.de (C.-C. Meyer), mokry@uni-mainz.de (C. Mokry), renisch@uni-mainz.de (D. Renisch). <https://orcid.org/0000-0002-0350-3784> (C.-C. Meyer). <https://orcid.org/0000-0001-8561-0016> (D. Renisch)

Jörg Runke, Department Chemie, Standort TRIGA – Johannes Gutenberg-Universität Mainz, 55128 Mainz, Germany; and GSI Helmholtzzentrum für Schwerionenforschung GmbH, 64291 Darmstadt, Germany, E-mail: runke@uni-mainz.de

Alice Seibert, European Commission, Joint Research Centre (JRC) – Karlsruhe, Hermann-von-Helmholtz-Platz 1, 76344 Eggenstein-Leopoldshafen, Germany, E-mail: Alice.SEIBERT@ec.europa.eu

Christina Trautmann, GSI Helmholtzzentrum für Schwerionenforschung GmbH, 64291 Darmstadt, Germany; and Technische Universität Darmstadt – Materialwissenschaft, 64287 Darmstadt, Germany, E-mail: C.Trautmann@gsi.de

Christoph E. Düllmann, Department Chemie, Standort TRIGA – Johannes Gutenberg-Universität Mainz, 55128 Mainz, Germany; Helmholtz-Institut Mainz, 55128 Mainz, Germany; and GSI Helmholtzzentrum für Schwerionenforschung GmbH, 64291 Darmstadt, Germany, E-mail: duellmann@uni-mainz.de. <https://orcid.org/0000-0002-1194-0423>

Keywords: electrochemical deposition; infrared spectroscopy; Molecular Plating; Raman spectroscopy; thin film deposition; X-ray photoelectron spectroscopy

1 Introduction

Electrochemical deposition of radionuclides has been researched for over 100 years.¹ Based on these studies Molecular Plating (MP) was developed 60 years ago by Parker and Falk² for the production of thin films.^{2–10} In MP the element of interest is electrochemically deposited from organic solutions such as alcohols.⁷ This method is still used as a standard to produce thin films on various substrates like titanium or carbon for various nuclear physics applications,^{8–13} including targets used for ion beam experiments for the production of superheavy elements.^{8,14–16}

The production of superheavy elements necessitates the use of actinides such as ^{242,244}Pu, ²⁴³Am, or ²⁴⁹Bk. The rarity of these isotopes necessitates the use of a technique that can achieve high deposition yields, which is possible with Molecular Plating. This technique enables the deposition of thin films with a thickness ranging up to about 1,000 $\frac{\mu\text{g}}{\text{cm}^2}$ on substrates such as thin titanium foils with a thickness of 2.3 μm . It is imperative that the targets have a homogeneous surface and exhibit sufficient resilience to withstand the impact of heavy ions, such as $\approx 5 \frac{\text{MeV}}{\text{u}}$ ⁴⁸Ca, at ion fluences of $10^{17} \frac{\text{ions}}{\text{cm}^2}$. Despite the long time, for which MP has been employed, the deposition process and the chemical composition of the thin

films are still being studied but yet not fully understood.^{17,18} It is, e.g., not fully clear why the quality and yield of the depositions often vary from deposition to deposition, despite identical experimental parameters.

Over the years, it has been found that the deposition is predominantly a basic precipitation of the element of interest.^{18–21} Spectroscopic studies suggested that organic components such as carbonates and carboxylates are present in the thin films alongside oxides and hydroxides.^{17,19} Carbonates can be formed by the presence of CO₂ and water in the reaction solution, by forming carbonic acid and its deprotonation. The concentration of CO₂ and water in the solvents can vary with the age of the solvents and the atmospheric conditions under which they are stored and used by diffusion.²²

Since targets are produced with rare isotopes, it is particularly undesirable if the deposition fails for no apparent reason. Therefore we have conducted a systematic investigation of the influence of CO₂ and water on layers produced by the MP technique. Instead of rare actinides, terbium and thulium are used as lighter homologous and are deposited on titanium foil. Unlike the actinides, terbium and thulium are not radioactive, which simplifies handling and allows for characterization in laboratories, that are not certified for work with radioactive samples.

2 Experimental section

2.1 Target production

All targets were prepared using terbium(III) nitrate (Tb(NO₃)₃ CAS: 10043-27-3), or thulium(III) nitrate (Tm(NO₃)₃ CAS: 36548-87-5) in analytical quality. The used solvents isobutanol (IB, CAS:78-83-1, 2-methylpropan-1-ol), isopropanol (IP, CAS:67-63-0, propan-2-ol) had water contents of 30–50 ppm according to the supplier. D₂O (CAS: 7789-20-0) was used to add water to the reaction solution. All chemicals were purchased from Merck KGaA, Darmstadt, Germany.

The reactions were prepared in an argon glovebox (MBraun) to keep ambient moisture and CO₂ as low as possible. D₂O was used with the intention to perform ²H NMR measurements of the supernatant solution. However, the NMR results showed no conclusive results.

The targets were deposited on 10-μm thick titanium foil from an alcoholic solution containing terbium and thulium using an electrochemical cell by applying a constant current of 0.7 $\frac{\text{mA}}{\text{cm}^2}$ for 2 h. The voltage between anode and cathode varied between 100 and 600 V for the depositions.

The molecular plating was performed in a small cell with a volume of 10 mL, which is shown in Figure 1. It features a circular deposition area with a diameter of 6 mm. The substrate for the deposition was a titanium foil with a thickness of 10 μm and a purity of 99.6 %. The titanium foil was purchased from HMW Hauner GmbH & Co. KG. A palladium wire (1 mm diameter) served as an anode. It was curled at the end to increase the surface toward the cathode.

The solvent used was a mixture of isobutanol (IB) and isopropanol (IP) in a ratio 9:1. Terbium nitrate and thulium nitrate were each dissolved in the solvent to get stock solutions with concentrations of 7.1 $\frac{\mu\text{g}}{\mu\text{L}}$. CO₂ was passed through the IB/IP = 9:1 mixture for 15 min to obtain a CO₂-saturated solution, which features a CO₂-concentration of 0.18 $\frac{\text{mol}}{\text{L}}$ at 20 °C for this specific mixture.²²

The saturated solution was mixed with a CO₂-free mixture containing the lanthanide salt. In this way, final solutions with different saturation levels of CO₂ (depending on the ratio between CO₂-saturated and untreated solvent) were produced. The untreated solvent was considered as CO₂-free as procured.

An aliquot of the stock solution containing 142 μg of the lanthanide was mixed with the CO₂-saturated alcoholic mixture to set the CO₂-concentration in the solution. As a result, each deposition led to an areal weight of 500 $\frac{\mu\text{g}}{\text{cm}^2}$ by assuming quantitative deposition.

Afterwards D₂O was added to that solution, to obtain the desired D₂O-concentration. The volume was adjusted to

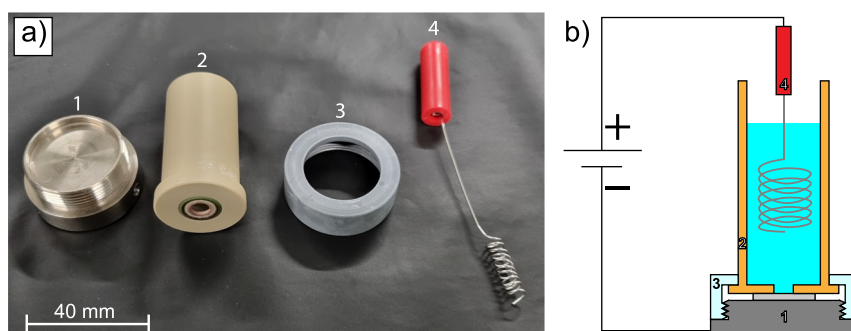


Figure 1: The used plating cell to produce the thin films. (a) The single parts of the cell (from left to right) consist of a titanium base (1), the PEEK cell with gasket and deposition opening with a diameter of 6 mm (2), a nut to fix the cell (3) and the palladium anode (4). (b) A scheme of the fully assembled and electrically connected PEEK cell is shown.

Table 1: Morphology and yield (given as percentage value in the corresponding field) of terbium thin films produced by Molecular Plating with varying water and CO₂-saturation. For selected samples, a picture from a conventional microscope is shown on the left side (diameter 6 mm). On the right a SEM picture of the sample with the size of 130 × 130 μm is shown for some samples.

CO ₂ saturation in %	D ₂ O concentration in vol%		Yield (%)
	Microscope	SEM	
0	0		8 ± 5 %
	0.2		21 ± 5 %
	0.5		87 ± 4 %
	1.0		93 ± 1 %
	1.5		68 ± 5 %
10	0		3 ± 3 %
	0.5		89 ± 1 %
	1.0		97 ± 1 %
	1.5		
	2.0		75 ± 2 %
20	0		9 ± 5 %
	0.5		88 ± 1 %
	1.0		91 ± 1 %
	1.5		
	2.0		
40	0		
	0.5		94 ± 1 %
	1.0		84 ± 1 %
	1.5		
	2.0		
50	0		9 ± 5 %
	0.5		74 ± 2 %
	1.0		84 ± 1 %
	1.5		
	2.0		
60	0		20 ± 5 %
	0.5		98 ± 1 %
	1.0		89 ± 1 %
	1.5		
	2.0		
80	0		19 ± 5 %
	0.5		
	1.0		81 ± 2 %
	1.5		
	2.0		
100	0		
	0.5		
	1.0		
	1.5		
	2.0		

10 mL with CO₂-free alcoholic mixture to achieve the desired concentration of CO₂ and D₂O. Targets were prepared with D₂O-concentrations of 0, 0.5, 1.0, 1.5 and 2.5 vol% and CO₂-saturations of 0, 20, 40, 60, 80 and 100 %. By varying both parameters fourteen targets were produced, as displayed in a matrix (Table 1) that encompasses both parameters.

2.2 Target analysis

Different methods were used to analyze the samples. Samples prepared with the salt Tb(NO₃)₃ were analyzed in a scanning electron microscope (SEM), and infrared (IR) and Raman spectra were recorded. The yields of the depositions

were determined indirectly by neutron activation analysis (NAA) by determining the lanthanide concentration left in the supernatant solution after deposition.²³

X-ray photoelectron spectroscopy (XPS) was performed on samples prepared with $\text{Tm}(\text{NO}_3)_3$.

2.2.1 Neutron activation analysis

Neutron activation analysis (NAA) is a simple and sensitive method of determining the quantity of a substance.²⁴ The terbium deposition yields were determined by NAA. For this purpose, aliquots of the solutions were taken before and after deposition and activated in the research reactor TRIGA Mainz at a neutron flux of $7 \times 10^{11} \frac{n}{\text{cm}^2 \text{s}}$ for 1 h. Terbium is a monoisotopic element (^{159}Tb). This isotope has a neutron capture cross section of 23.6 b. The neutron capture product ^{160}Tb has a half-life of 72.3 d and undergoes β^- decay (100 %), which is followed by a gamma-ray emission [$E_\gamma = 879$ keV (30.1 %); 299 keV (26.1 %) and 966 keV (25.1 %)].²⁵ After neutron irradiation, the gamma activities of the samples were measured in a high purity germanium (HPGe) detector (Ortec) and the gamma spectra were evaluated with the Genie 2000 software (Canberra). From the difference of the activities of the samples before and after deposition, the deposition yield, is obtained, assuming that all of the lanthanides no longer present after the plating procedure were deposited on the substrate. The thin films were not measured directly as their geometry precluded their activation due to the fact that bending the substrate in order to irradiate it in the reactor would destroy the thin film.

2.2.2 Scanning electron microscopy

To evaluate the surface morphology of the films, the samples were examined in a scanning electron microscope (SEM, Philips XL30) with an accelerating voltage of 20 kV in combination with detectors for secondary (SE) and backscattered electrons (BSE).

2.2.3 Confocal Raman spectroscopy

The targets were analyzed with a confocal Raman microscope (HR800 system, Horiba Jobin Yvon) of the Materials Research Department at GSI Darmstadt. A laser with 473 nm emission wavelength, a grating with $1,800 \frac{\text{grooves}}{\text{mm}}$, and a slit width of 100 μm were used to acquire the data. The spectral resolution was 0.8 cm^{-1} . The acquisition time for one spectrum was set to 20 s for all measurements. Raman spectra of the different terbium nitrate samples from 200 cm^{-1} – $3,200 \text{ cm}^{-1}$ were collected.

2.2.4 Infrared microscopy

The targets were analyzed by infrared microscopy (Nicolet Continuum connected to a Nicolet 6700, THERMO SCIENTIFIC) at the Institute of Geosciences of the Johannes Gutenberg University Mainz. A mercury cadmium telluride (short: MCT) detector was used. The increments were set to 0.1 nm. The acquisition time for each spectrum was set to 5 min. Infrared spectra from 650 cm^{-1} to $4,000 \text{ cm}^{-1}$ were collected in reflection on a gold mirror. IR spectra were recorded from three different locations of each terbium thin film produced to exclude artifacts in the film. The reflection of IR radiation from the sample was measured. Initially, the substrate, which was titanium, was measured for background correction. The Ti background was subtracted from the recorded spectra.

2.2.5 X-ray photoelectron spectroscopy

The XPS spectra were recorded at the Joint Research Center (JRC) in Karlsruhe, Germany.²⁶ For the XPS analysis of the $\text{D}_2\text{O}/\text{CO}_2$ matrix samples, the thulium targets were used because the relevant XPS peaks in the investigated thulium and oxygen binding energy regions are not superimposed or interfered by other contributions. Targets from 0.5 and 1 vol% D_2O -concentration and CO_2 -saturation from 0 to 80 % were produced as described in Section 2.1 and placed on designated XPS sample holders. These targets were enclosed in an airtight container and transported to JRC Karlsruhe where they were introduced into the ultra-high vacuum (UHV) chamber for the XPS measurements via a two-stage loading system. The facility at JRC Karlsruhe is described in²⁶.

The XPS measurements were conducted several weeks after sample preparation and days after introduction to the UHV system. They were also stored during the measurement campaign of 2 weeks in a chamber with a base pressure of about 2.0×10^{-10} mbar adjacent to the XPS analysis chamber. XPS measurements were performed using a monochromatic Al K_α -X-ray source (XRC-1000 MF) equipped with a μ -FOCUS 500 monochromator and a Phoibos 150 hemispherical analyzer controlled by a HAS 3500 plus system (both from Specs, Berlin). The spectrometer was calibrated using the Au metal's $4f_{7/2}$ (83.9(1) eV) and Cu metal's $2p_{3/2}$ (932.7(1) eV) reference lines. Surveys and high-resolution spectra were recorded at pass energies of 50 or 20 eV. To suppress sample charging, a flood gun FG-500 (Specs, Berlin) was available. All measurements were conducted at room temperature using an in-house data acquisition program.

3 Results and discussion

3.1 Morphology

The morphology of the samples prepared from $\text{Tb}(\text{NO}_3)_3$, examined with the scanning electron microscope and a conventional USB optical microscope (Traveler), are shown in Table 1, tabulated according to the D_2O and CO_2 -concentration.

The images of the thin films show that a deposition without the presence of D_2O or CO_2 is not possible. The light microscope image shows a slightly darker shade of the titanium substrate where the deposition took place. However, the SEM image clearly shows the substrate and the rolling marks from production. There is no significant height contrast, indicating that the surface is relatively smooth. Addition of CO_2 to the solution facilitates deposition, but the thin films show only loose tiles with wide cracks in between, as seen in the SEM images shown in Table 1. This trend is even more pronounced when the CO_2 content in the solution is high. Clearly a deposition can be seen at a water concentration of 0.5–1 vol%. This is visible due to the white layer on the titanium substrate. Additionally, in the SEM pictures there is clearly a layer visible, which shows “mudcracking”, which is already described for molecular plated targets by e.g. Vascon et al.¹⁷ If the CO_2 content of the solution increases at these water concentrations, the thin films become brittle and the mudcracking becomes more intense. At 80 % CO_2 saturation, the tiles are loose and the thin film does no longer adhere well to the substrate. This is visible with the naked eye and especially in the corresponding SEM picture for the sample with 0.5 vol% D_2O .

It can be seen that the film quality again decreases dramatically, if the water concentration in the reaction solution exceeds 1 vol%. The layer is inhomogeneous and a look at the surface with the naked eye shows a brittle film. In the SEM image the films do no longer show the typical mudcracking, but rather singular regions with granular material without significant adherence to the substrate.

Table 1 highlight the crucial role of D_2O and CO_2 levels on the film quality and yield. Molecular Plating needs the presence of water in the solution. D_2O concentration of 0.5 or 1 vol% facilitates Molecular Plating, while higher water content results in weak adhesion and more cracked films, as exemplified by the sample with 1.5 vol%. To achieve optimal results, it is recommended to have a water content of 0.5–1 vol% in the solution. The presence of water in Molecular Plating induces cathodic reduction, converting water into hydrogen and hydroxide ions. The hydroxide ions create a local alkaline environment at the cathode, promoting deposition as is long known.¹⁸ However, we assume

that the generation of hydrogen has negative effects on the film quality. An increase of water content triggers excessive hydrogen formation. This leads to a constant production of hydrogen at the surface hindering the formation of a thin layer at this particular point, thereby preventing adhesion, leading to the formation of a heavily cracked film, and to reduced adhesion and homogeneity.

3.2 Yields

Deposition yields of terbium were indirectly determined by NAA of the supernatant solution. The yields as function of the D_2O and CO_2 -concentrations are given in Table 1.

The uncertainties are based on the net number of counts of the gamma spectra of the supernatant solution before and after deposition, and the resulting Gaussian error propagation.

Without any addition of water beyond the amounts already present in the solvents the deposition yield remains below 20 % and reaches such levels only at elevated CO_2 concentrations. In a water concentration of 0.5–1.0 vol%, the yield increases significantly, reaching levels of 90 %, and does become independent of the CO_2 concentration. However, higher CO_2 concentrations under these conditions result in films that are more brittle and show poor adhesion to the substrate. At yet higher water concentrations, the yield decreases again. The influence of CO_2 in this regime was not studied, as the negative effects associated with increasing CO_2 concentrations had already been observed at lower water concentrations.

Even trace amounts of water, in the order of a few ppm as already present in the original solution, appear sufficient to promote the formation and precipitation of carbonates, albeit this results in small yields (<20 %) and films with poor adhesion to the substrate.

Molecular Plating can produce thin films even without the addition of water, if the CO_2 concentration is high enough. With small amounts of water in the range of a few ppm already present in the solution, carbonates can be formed and precipitated in the process. However, the adhesion to the substrate is weak and the deposition yield does not exceed 20 %. The presence of CO_2 might alter the film composition by incorporating carbonates and formates, facilitating deposition. However, this modified composition does lead to insufficient adhesion and low yields.

Additionally, the introduction of CO_2 to the reaction solution containing 0.5 or 1 % D_2O results in diminished adhesion and film uniformity compared to films prepared without CO_2 . SEM images reveal that cracks in the films

become more pronounced as the CO_2 concentration increases in the solution.

3.3 Raman and IR spectroscopy

Spectra taken with the Raman microscope of all samples with 0.5 vol% D_2O are shown in Figure 2 and those of all samples with 1.0 vol% D_2O in Figure 3. Due to the inhomogeneity and the mudcracking of the surface of the films, it is challenging to make quantitative statements. Consequently, qualitative statements are made about the individual spectra. The individual bands are then compared to the baseline of the spectra, thus enabling statements to be made about the influence of CO_2 and D_2O on the samples.

The observed vibrational bands and their assignments to the corresponding species^{27–31} are summarized in Table 2.

The Raman spectra of the samples with 0.5 vol% of water show bands at approximately 500 cm^{-1} (assigned to oxidic species), at 700 cm^{-1} and $1,100\text{ cm}^{-1}$ (assigned to carbonate vibrations), and at $2,700\text{--}3,000\text{ cm}^{-1}$ (assigned to formate vibrations). Notably, no formates or formic acid were intentionally added to the solutions.

With increasing CO_2 -concentrations, the oxidic vibration (500 cm^{-1}) diminishes, while the carbonate vibrations (700 cm^{-1} and $1,100\text{ cm}^{-1}$) become more pronounced compared to the baseline. Additionally, the peak at 700 cm^{-1} becomes significantly broader. The formate peaks also broadens, but does not intensify as much as the carbonate peak with increasing CO_2 -concentrations. Frost et al.²⁷ reported a weak carbonate band at the range of $1,400\text{--}1,500\text{ cm}^{-1}$, which could not be observed. Since its

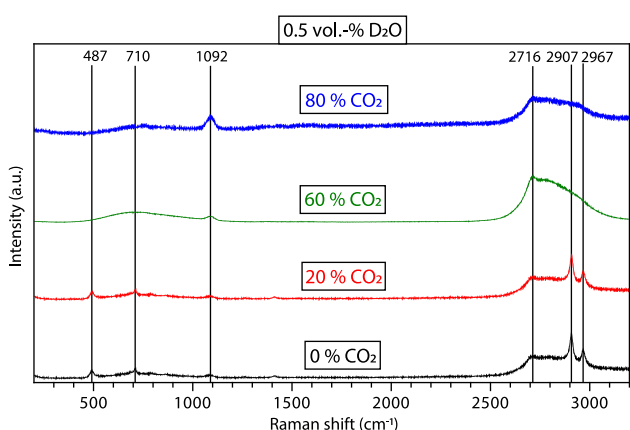


Figure 2: Stacked Raman spectra of terbium thin films produced by MP from solution with fixed water content of 0.5 vol% D_2O and different CO_2 saturation. All spectra are normalized to their respective maximum value. A detailed assignments of the vibrational bands are given in Table 2.

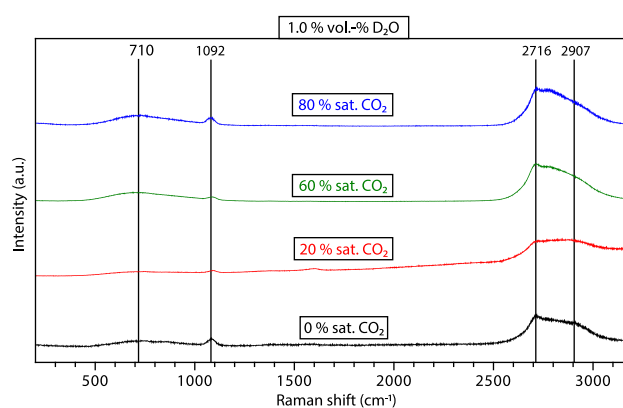


Figure 3: Stacked Raman spectra of terbium thin films produced by MP from solution with fixed water content of 1.0 vol% D_2O and different CO_2 saturation. All spectra are normalized to their respective maximum value. A detailed assignments of the vibrational bands are given in Table 2.

intensity is weak, we assume, that the band disappears due to the mudcracking and amorphicity of the sample.

This broadening phenomenon of vibrational bands is observed consistently in all spectra of samples with 1 vol% water concentration.

With increasing water content in the samples, it should be assumed that the oxide bands are more pronounced. However, these were no longer observed in the Raman spectra. We suspect that the oxidic bands are still present, but are no longer observable in the Raman spectra, because more cracks appear in the thin films. These cracks enhance unintentional light scattering, thereby diminishing the intensity of the detected Raman bands.

Spectra taken with the infrared microscope are shown in Figures 4 and 5. Like for the Raman spectra, all samples

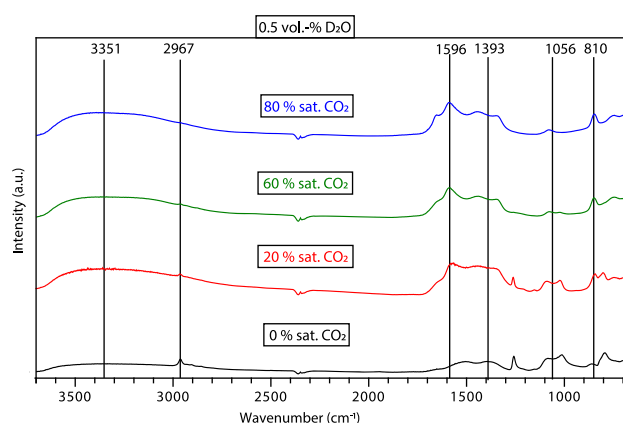


Figure 4: Stacked IR spectra of terbium thin films produced by MP from solutions with fixed water concentration of 0.5 vol% D_2O and different CO_2 saturation. All spectra are normalized to their respective maximum value. A detailed assignments of the vibrational bands are given in Table 2.

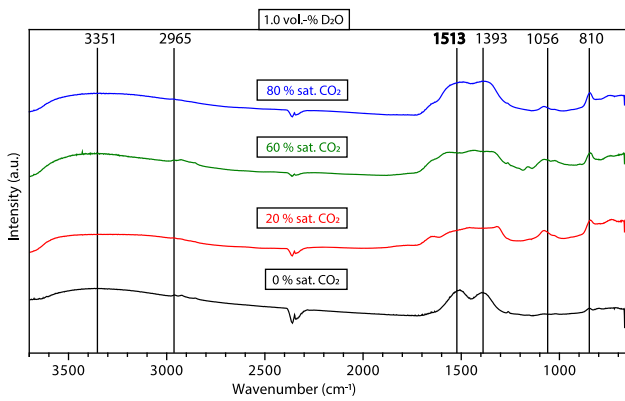


Figure 5: Stacked IR spectra of terbium thin films produced by MP from solutions with fixed water concentration of 1.0 vol% D₂O and different CO₂ saturation. All spectra are normalized to their respective maximum value. A detailed assignments of the vibrational bands are given in Table 2.

Table 2: The assignment of the Raman and IR bands to the corresponding vibrations and species.

Chemical species	Vibration mode	Raman band [cm ⁻¹]	IR band [cm ⁻¹]	Reference
Hydroxide residue water	ν	–	3,351	33
Oxide	ν_4	487	–	34
Carbonate	ν_3	–	1,596	27,30,35–37
	ν_3	–	1,393	
	ν_1	1,092	–	
	ν_2	–	1,056	
	ν_4	710	810	
Formate	ν_1	2,967	2,965	28,36,38,39
	ν_1	2,907	–	
	ν_1	2,716	–	
	ν_5	–	1,596	
	ν_2	–	1,393	
	ν_6	–	1,056	

with 0.5 vol% and with 1.0 vol% D₂O were combined in one graph each. In Table 2 all bands and assigned species^{28–32} are given. As described above, qualitative statements are also predominantly made here. Here too, the intensities of the individual bands compared to the baseline are taken into account for the evaluation.

The infrared spectra reveal the presence of oxides, carbonates, and also formates. A broad band at 3,600–2,800 cm⁻¹ indicates hydroxide vibrations. At 2,967 and 2,965 cm⁻¹, a formate band is evident, but it diminishes with increasing CO₂-content. At 2,400 cm⁻¹, a vibrational band associated with titanium is observed in the spectra.

At 1,596 cm⁻¹, carbonate, and formate bands overlap, with additional overlap at 1,393 cm⁻¹ and 1,056 cm⁻¹, making distinct identification challenging. The only interference free bands of an organic compound is the formate band at 2,950 cm⁻¹. Another carbonate band can be observed at 810 cm⁻¹.

As the concentrations of water and CO₂ increase, a broadening of the carbonate bands is evident.

In addition to hydroxides and oxides, vibrational modes of carbonates and formates are visible in the spectra. The Raman and IR spectra reveal that formates are produced when the MP process occurs. This can be understood by the CO₂ exposure to negative potentials and high pH value at the cathode. In this situation, CO₂ can be transformed into formates through reduction, as indicated by the Pourbaix diagram shown in Figure 6.⁴⁰

However, the Raman spectra show that a significant portion of CO₂ transforms into carbonates, leading to their precipitation. This is visible by the increased intensity of the carbonate bands in the Raman spectra at 710, 1,092 and 2,716 cm⁻¹, while the formate peaks do not increase in intensity with increasing CO₂ compared to the base line of each spectrum. The deposition of carbonates can occur immediately; however, the electrochemical production of formates at the cathode is a prerequisite for their subsequent deposition. The formation of formates at the cathode precedes the deposition process, which is the rate-limiting step in formate deposition.

If the CO₂ concentration increases in the solution, the amount of carbonates in the thin film also increases. In contrast the relative amount of oxides decreases. This shows that the formation of carbonates competes with the formation of hydroxides and oxides.

3.4 X-ray photoelectron spectroscopy

Figures 7 and 8 display XPS detail spectra (C_{1s}, O_{1s}, Tm_{4d}, Ti_{2p}) for samples with 0.5 and 1 vol% water at 0 and 80 % CO₂

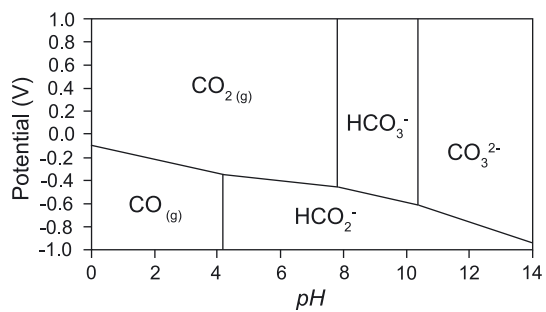


Figure 6: The Pourbaix diagram for CO₂ depicts how CO₂ reacts in water across varying pH levels and diverse potentials relative to a standard reference electrode.⁴⁰

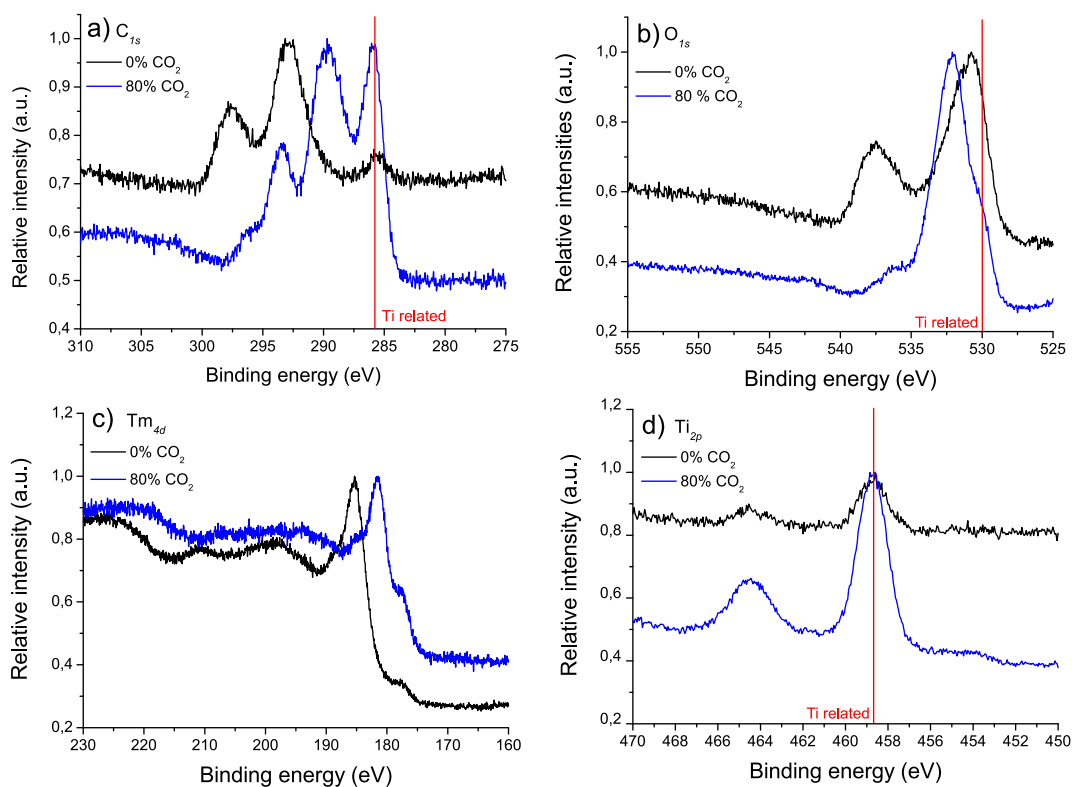


Figure 7: XPS spectra of C_{1s} (a), O_{1s} (b), Tm_{4d} (c) and Ti_{2p} (d) of samples with 0.5 vol% D₂O at 0 % CO₂ saturation (black) versus 80 % CO₂ saturation (blue). The red vertical lines represent species related to the titanium substrate.

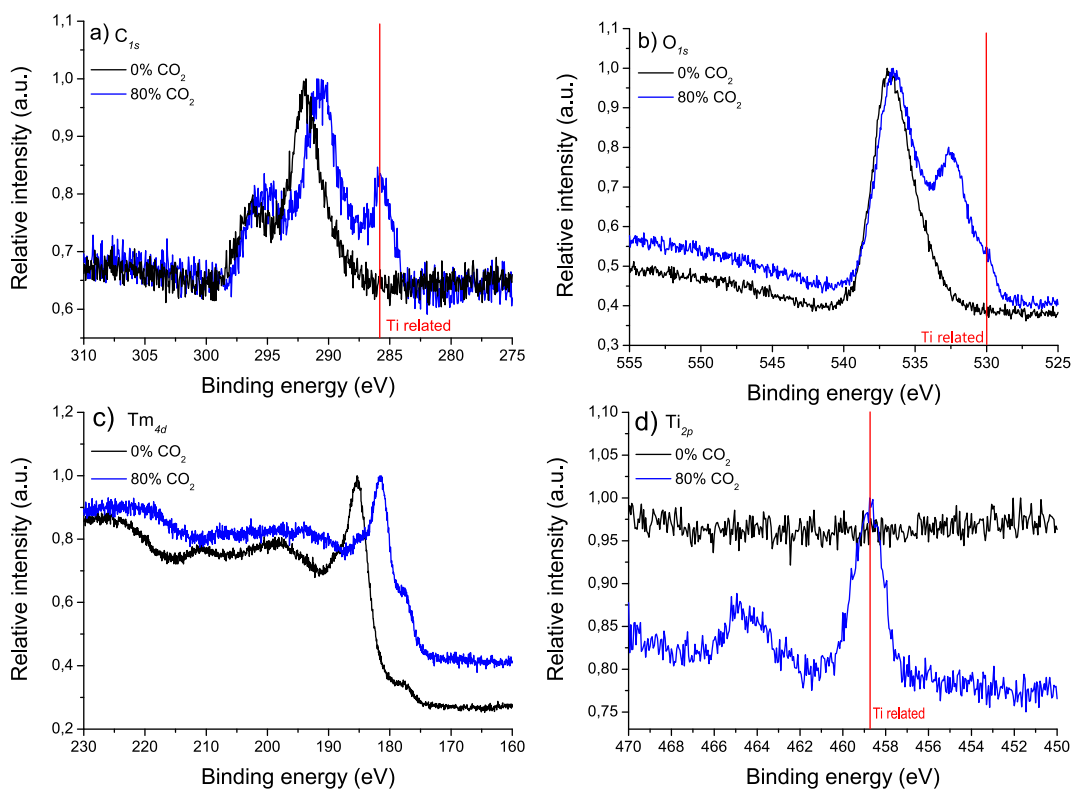


Figure 8: XPS spectra of C_{1s} (a), O_{1s} (b), Tm_{4d} (c) and Ti_{2p} (d) of samples with 1 vol% D₂O at 0 % CO₂ saturation (black) versus 80 % CO₂ saturation (blue). The red vertical lines represent species related to the titanium substrate.

saturation. The thick thulium deposits and use of a monochromatic X-ray source caused charging, leading to shifted peak positions due to the insulating nature of the material. This could only be partially compensated by a flood gun.

Cracking and flaking of the thin films, similar to the terbium samples shown in Table 1, expose the titanium backing, complicating spectral interpretation. Signals stemming from the titanium substrate appear in the C_{1s} and O_{1s} spectra in addition to the signals related to the deposited thulium layers. The Ti_{2p} doublet at ≈ 458.7 and 464.4 eV, with 5.7 eV spin-orbit splitting, indicates a TiO_2 surface layer, which is also present on untreated titanium foils. The titanium substrate related signals remain unshifted, indicating effective charge compensated.

Charging effects and overlapping signals hinder the precise assignment of the C_{1s} and O_{1s} peaks. A consistent C_{1s} peak at ≈ 285 eV, which is highlighted by the red line in

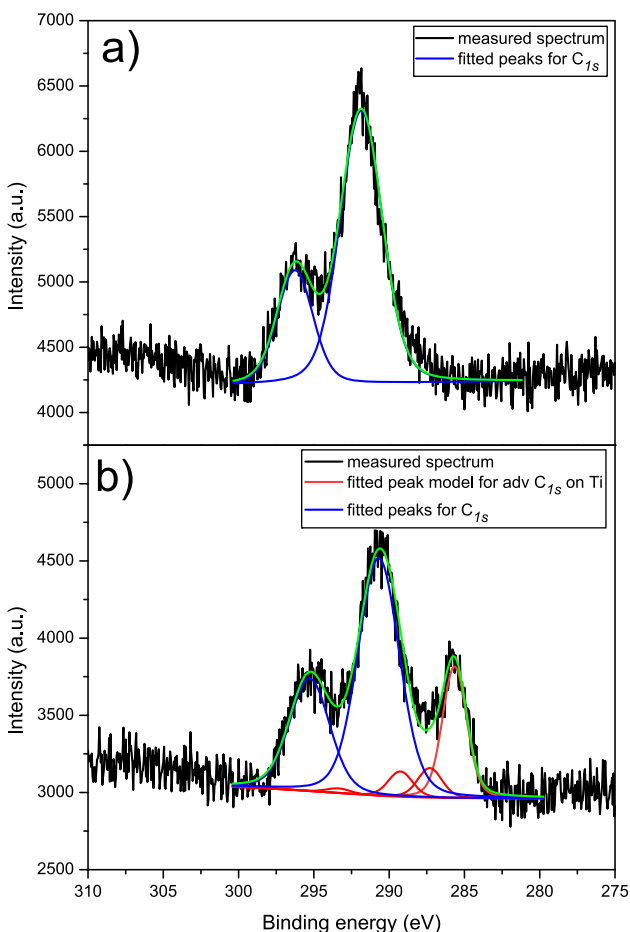


Figure 9: Comparison of C_{1s} spectrum for a deposition from 1 vol% water and 0 % CO_2 (panel a) and a deposition from 1 vol% water and 80 % CO_2 (panel b). The black curves are the measured spectra. The blue curves are the fitted peaks for C_{1s} . The red curves are the fitted peak model for adventitious C_{1s} on titanium. The green curve is the fitted envelope.

Figures 7a and 8a correlates with the presence of Ti_{2p} suggesting it originates from adventitious carbon on the titanium backing. A peak model for this C_{1s} contribution was developed (Figure 9b, red curves) based on a titanium blank sample. Additional broad C_{1s} peaks are observed and attributed to charge-shifted carbon species from the deposition.

Figure 9 compares C_{1s} spectra from 1 vol% D_2O samples at 0 % (panel a) and 80 % CO_2 (panel b). The fitting approaches shows beside the 285.7 eV peak related to titanium backing broader, shifted components at around 290 eV and 296 eV attributed to carbon originating from the deposition.

The ≈ 4.5 eV peak separation and intensity ratio of ≈ 2.5 differ from typical adventitious carbon, suggesting higher-oxidized species.

Barr et al.⁴¹ identified C–C/C–H as the main component of adventitious carbon, with minor contributions from C–O and O–C=O (as seen for the adventitious carbon on titanium substrate). In contrast, the thulium films show unusually strong high-BE components, likely indicating formates or carbonates from the deposition in addition to the adventitious carbon layer.

The O_{1s} spectra (Figures 7b and 8b) include a Ti-related oxide peak at ≈ 533 eV (indicated by the red line), and broader peaks at ≈ 533 and 537 eV. The high-BE peak at ≈ 537 eV decreases with CO_2 content and increase with water content, possibly linked to oxidic species (Tm_2O_3) while the peak at ≈ 530 eV increases in intensity with increasing CO_2 -content, possibly linked to carbonates/formates.

The Tm_{4d} region (Figures 7c and 8c) shows a main peak between 181.4 and 185 eV, with a low-BE shoulder (≈ 178 eV) more pronounced at depositions with high CO_2 . This may reflect different thulium species or uncharged deposit regions due to the influence of the cracked thin film and possible increasing conductivity. XPS trends align with IR/Raman data for terbium films: oxide signals diminish while carbonate signals rise with increasing CO_2 . In the 0.5 vol% D_2O series, high-BE C_{1s} peaks (5.6 – 6.3 eV) appear, consistent with carbonate formation. These films, though prone to charging, indicate CO_2 -induced preference for carbonates over oxides.

4 Conclusion and outlook

CO_2 and water greatly affect the layers produced by the Molecular Plating technique, emphasizing the importance of controlling solvent purity. Water is essential in the reaction solution for Molecular Plating, but excessive water concentration (>1 vol%) leads to a deterioration in thin film quality.

The presence of CO₂ consistently degrades the thin film quality by increasing carbonate content.

No conclusions can be drawn from the IR and Raman spectra about the absolute quantity of the different species and their relative concentrations to each other. Only trends between the spectra can be observed. The Raman and IR spectra show clearly the presence of hydroxides and oxides. This also fits to the theory that the Molecular Plating technique is based on hydroxide precipitation.¹⁸

The IR and Raman spectra clearly indicate the presence of carbonates and formates besides hydroxides and oxides in the thin films. These formates are generated and deposited through CO₂ reduction under basic conditions at the cathode.

Moreover, the spectra reveal that as the CO₂ content in the solutions increases, the amount of carbonate rises while the relative levels of oxide and hydroxide species decrease, indicating that the reactions forming these species competes with each other. The XPS spectra further support the trends that the formation of carbonates and oxides compete with each other.

The obtained XPS spectra are difficult to interpret, though. Charging effects seem to affect different parts of the surface differently, leading to somewhat arbitrary shifts and fragmentation of the peaks. Due to the complex composition of the samples and the charging effects an extensive peak fitting does not seem advisable.

Thinner films might be less affected by charging, since the layer thickness influences its insulation and therefore the charging effects. So by using relatively thin films of maybe $<100 \frac{\mu\text{g}}{\text{cm}^2}$ that also seem to have a more homogeneous surface without major mud cracking some clarification may be obtained from XPS. On the other hand such very thin films may not represent the full reality of the final targets actually in use for the super heavy-element production.

In summary, the solvent quality significantly influences the success of the deposition process and requires careful control. Preserving high solvent quality can be achieved by storing them in an inert atmosphere, such as a glove box.

In the future, these discoveries can enhance the reliability and effectiveness of Molecular Plating. By deepening our understanding of the chemical composition, we can improve the technique itself, as well as create novel methods derived from these insights. These advancements aid the production of more effective targets for ion beam experiments and other nuclear physical experiments.

Acknowledgments: Our sincere thanks go the staff of the mechanical workshop at the research reactor TRIGA Mainz for their local support. We would also like to thank Constantin Haese from the Max-Planck-Institut für Polymerforschung

Mainz who carried out NMR measurements for us. We acknowledge funding from the German Federal Ministry for Research and Education (project 05P21UMFN2). The experimental data used in this research were generated through access to the ActUsLab/PAMEC under the Framework of access to the Joint Research Centre Physical Research Infrastructures of the European Commission (Project Targets-SHE2, Research Infrastructure Access Agreement No 36107/01).

Research ethics: Not applicable.

Informed consent: Not applicable.

Author contributions: All authors have accepted responsibility for the entire content of this manuscript and approved its submission.

Use of Large Language Models, AI and Machine Learning

Tools: During the preparation of this work the authors used [ChatGPT GPT-4o] to improve readability and language. After using this tool, the authors reviewed and edited the content as needed and take full responsibility for the content of the published article.

Conflict of interest: The author state no conflict of interest.

Research funding: German Federal Ministry for Research and Education (project 05P21UMFN2).

Data availability: The data that support the findings of this study are available from the corresponding author, E.A., upon reasonable request.

References

1. Tödt, F. Die elektrolytische Abscheidung unedler Radioelemente. *Z. Phys. Chem.* **1924**, *113U*, 329–335.
2. Parker, W.; Falk, R. Molecular Plating: A Method for the Electrolytic Formation of Thin Inorganic Films. *Nucl. Instrum. Methods* **1962**, *16*, 355–357.
3. Parker, W.; Bildstein, H.; Getoff, N. Molecular Plating I, a Rapid and Quantitative Method for the Electrodeposition of Thorium and Uranium. *Nucl. Instrum. Methods* **1964**, *26*, 55–60.
4. Parker, W.; Bildstein, H.; Getoff, N.; Fischer-Colbrie, H.; Regal, H. Molecular Plating II a Rapid and Quantitative Method for the Electrodeposition of the Rare-Earth Elements. *Nucl. Instrum. Methods* **1964**, *26*, 61–65.
5. Getoff, N.; Bildstein, H.; Proksch, E.; Molecular plating, V. The Influence of Some Experimental Factors on the Deposition Yield. *Nucl. Instrum. Methods* **1967**, *46*, 305–308.
6. Getoff, N.; Bildstein, H. Molecular Plating. *Nucl. Instrum. Methods* **1969**, *70*, 352–354.
7. Eberhardt, K.; Brühle, W.; Düllmann, C.; Gregorich, K.; Hartmann, W.; Hübner, A.; Jäger, E.; Kindler, B.; Kratz, J.; Liebe, D.; Lommel, B.; Maier, H. J.; Schädel, M.; Schausten, B.; Schimpf, E.; Semchenkov, A.; Steiner, J.; Szerypo, J.; Thörle, P.; Türlér, A.; Yakushev, A. Preparation of Targets for the Gas-Filled Recoil Separator TASCA by Electrochemical Deposition and Design of the TASCA Target Wheel Assembly. *Nucl. Instrum. Methods Phys. Res., Sect. A* **2008**, *590*, 134–140.
8. Runke, J.; Düllmann, C. E.; Eberhardt, K.; Ellison, P. A.; Gregorich, K. E.; Hofmann, S.; Jäger, E.; Kindler, B.; Kratz, J. V.; Krier, J.; Lommel, B.;

- Mokry, C.; Nitsche, H.; Roberto, J. B.; Rykaczewski, K. P.; Schädel, M.; Thörle-Pospiech, P.; Trautmann, N.; Yakushev, A. Preparation of Actinide Targets for the Synthesis of the Heaviest Elements. *J. Radioanal. Nucl. Chem.* **2013**, *299*, 1081–1084.
9. Loveland, W. High Quality Actinide Targets. *J. Radioanal. Nucl. Chem.* **2015**, *307*, 1591–1594.
10. Loveland, W.; Baker, J. D. Target Preparation for the Fission TPC. *J. Radioanal. Nucl. Chem.* **2009**, *282*, 361–363.
11. Greene, J. P.; Janssens, R. V.; Ahmad, I. Preparation of Actinide Targets by Molecular Plating for Coulomb Excitation Studies at ATLAS. *Nucl. Instrum. Methods Phys. Res., Sect. A* **1999**, *438*, 119–123.
12. Haas, R.; Hufnagel, M.; Abrosimov, R.; Düllmann, Ch. E.; Krupp, D.; Mokry, C.; Renisch, D.; Runke, J.; Scherer, U. W. Alpha Spectrometric Characterization of Thin ^{233}U Sources for $^{229\text{m}}\text{Th}$ Production. *Radiochim. Acta* **2020**, *108*, 923–941.
13. Trautmann, N.; Folger, H. Preparation of Actinide Targets by Electrodeposition. *Nucl. Instrum. Methods Phys. Res., Sect. A* **1989**, *282*, 102–106.
14. Düllmann, C. E.; Artes, E.; Dragoun, A.; Haas, R.; Jäger, E.; Kindler, B.; Lommel, B.; Mangold, K. M.; Meyer, C. C.; Mokry, C.; Munnik, F.; Rapps, M.; Renisch, D.; Runke, J.; Seibert, A.; Stöckl, M.; Thörle-Pospiech, P.; Trautmann, C.; Trautmann, N.; Yakushev, A. Advancements in the Fabrication and Characterization of Actinide Targets for Superheavy Element Production. *J. Radioanal. Nucl. Chem.* **2022**, *332*, 1505–1514.
15. Düllmann, C. E.; Block, M.; Heßberger, F. P.; Khuyagbaatar, J.; Kindler, B.; Kratz, J. V.; Lommel, B.; Münzenberg, G.; Pershina, V.; Renisch, D.; Schädel, M.; Yakushev, A. Five Decades of GSI Superheavy Element Discoveries and Chemical Investigation. *Radiochim. Acta* **2022**, *110*, 417–439.
16. Lommel, B.; Düllmann, C. E.; Kindler, B.; Renisch, D. Status and Developments of Target Production for Research on Heavy and Superheavy Nuclei and Elements. *Eur. Phys. J. A* **2023**, *59*; <https://doi.org/10.1140/epja/s10050-023-00919-7>.
17. Vascon, A.; Santi, S.; Isse, A.; Reich, T.; Drebert, J.; Christ, H.; Düllmann, C. E.; Eberhardt, K. Elucidation of Constant Current Density Molecular Plating. *Nucl. Instrum. Methods Phys. Res., Sect. A* **2012**, *696*, 180–191.
18. Hansen, P. The Conditions for Electrodeposition of Insoluble Hydroxides at a Cathode Surface: A Theoretical Investigation. *J. Inorg. Nucl. Chem.* **1959**, *12*, 30–37.
19. Artes, E.; Düllmann, C. E.; Meyer, C.-C.; Renisch, D. The Process of Molecular Plating and the Characteristics of the Produced Thin Films – what We Have Learned in 60 Years and what is Still Unknown. *EPJ Web Conf.* **2023**, *285*, 03001.
20. Crespo, M. A Review of Electrodeposition Methods for the Preparation of Alpha-Radiation Sources. *Appl. Radiat. Isot.* **2012**, *70*, 210–215.
21. Klemenčič, H.; Benedik, L. Alpha-Spectrometric Thin Source Preparation with Emphasis on Homogeneity. *Appl. Radiat. Isot.* **2010**, *68*, 1247–1251.
22. Fogg, P. Pergamon Press Ltd. In *Carbon Dioxide in Non-aqueous Solvents at Pressures Less than 200 kPa*; Pergamon Press Ltd.: Oxford, 2017.
23. Liebe, D.; Eberhardt, K.; Hartmann, W.; Häger, T.; Hübner, A.; Kratz, J.; Kindler, B.; Lommel, B.; Thörle, P.; Schädel, M.; Steiner, J. The Application of Neutron Activation Analysis, Scanning Electron Microscope, and Radiographic Imaging for the Characterization of Electrochemically Deposited Layers of Lanthanide and Actinide Elements. *Nucl. Instrum. Methods Phys. Res., Sect. A* **2008**, *590*, 145–150.
24. Eberhardt, K.; Geppert, C. The Research Reactor TRIGA Mainz – a Strong and Versatile Neutron Source for Science and Education. *Radiochim. Acta* **2019**, *107*, 535–546.
25. Nica, N. Nuclear Data Sheets for A = 160. *Nucl. Data Sheets* **2021**, *176*, 1–428.
26. Gouder, T.; Huber, F.; Eloirdi, R.; Caciuffo, R. U_2O_5 Film Preparation via UO_2 Deposition by Direct Current Sputtering and Successive Oxidation and Reduction with Atomic Oxygen and Atomic Hydrogen. *J. Visualized Exp.* **2019**, *144*, e59017.
27. Frost, R. L.; Dickfos, M. J. Raman Spectroscopy of Halogen-Containing Carbonates. *J. Raman Spectrosc.* **2007**, *38*, 1516–1522.
28. Kartha, V.; Venkateswaran, S. Vibrational Spectra and Normal Vibrations of Rare Earth Formates. *Spectrochim. Acta, Part A* **1981**, *37*, 927–934.
29. Silva, E. N.; Moura, M. R.; Ayala, A. P.; Guedes, I.; Polla, G.; Vega, D. R.; Tobia, D.; Saleta, M. E. Vibrational Modes of Rare-Earth Formates. *J. Raman Spectrosc.* **2009**, *40*, 954–957.
30. Spiridigliozzi, L.; Bortolotti, M.; Accardo, G.; Vergara, A.; Frattini, D.; Ferone, C.; Cioffi, R.; Dell’Agli, G. An In-Depth Multi-Technique Characterization of Rare Earth Carbonates – $\text{RE}_2(\text{CO}_3)_3 \cdot 2\text{H}_2\text{O}$ – Owning Tengerite-type Structure. *J. Rare Earths* **2022**, *40*, 1281–1290.
31. Sohn, Y. Structural and Spectroscopic Characteristics of Terbium Hydroxide/Oxide Nanorods and Plates. *Ceram. Int.* **2014**, *40*, 13803–13811.
32. Caro, P.; Sawyer, J.; Evning, L. The Infrared Spectra of Rare Earth Carbonates. *Spectrochim. Acta, Part A* **1972**, *28*, 1167–1173.
33. Klevtsov, P. V.; Klevtsova, R. F.; Sheina, L. P. Relationship between the Infrared Absorption Spectra and Crystal Structure of the Hydroxides of the Rare Earth Elements and Yttrium. *J. Struct. Chem.* **1967**, *8*, 229–233.
34. White, W. B.; Keramidis, V. G. Vibrational Spectra of Oxides with the C-type Rare Earth Oxide Structure. *Spectrochim. Acta, Part A* **1972**, *28*, 501–509.
35. Frost, R. L.; Erickson, K. L.; Weier, M. L.; McKinnon, A. R.; Williams, P. A.; Leverett, P. Effect of the Lanthanide Ionic Radius on the Raman Spectroscopy of Lanthanide Agardite Minerals. *J. Raman Spectrosc.* **2004**, *35*, 961–966.
36. Frost, R. L.; López, A.; Scholz, R.; Xi, Y.; Belotti, F. M. Infrared and Raman Spectroscopic Characterization of the Carbonate Mineral Huanghoite – and in Comparison with Selected Rare Earth Carbonates. *J. Mol. Struct.* **2013**, *1051*, 221–225.
37. Rahimi-Nasrabadi, M.; Pourmortazavi, S. M.; Ganjali, M. R.; Norouzi, P. Nanosized Terbium Carbonate and Oxide Particles: Optimized Synthesis, and Application as Photodegradation Catalyst. *J. Mater. Sci.: Mater. Electron.* **2017**, *29*, 2988–2998.
38. Saralidze, O. D.; Shklover, L. P.; Petrov, K. I.; Plyushchev, V. E. Infrared Absorption Spectra of Formates of the Rare Earth Elements. *J. Struct. Chem.* **1967**, *8*, 45–49.
39. De Hosson, J. The Infrared Spectra of Several Rare-Earth Formates. *J. Inorg. Nucl. Chem.* **1975**, *37*, 2350–2351.
40. König, M.; Vaes, J.; Klemm, E.; Pant, D. Solvents and Supporting Electrolytes in the Electrocatalytic Reduction of CO_2 . *iScience* **2019**, *19*, 135–160.
41. Barr, T. L.; Seal, S. Nature of the Use of Adventitious Carbon as a Binding Energy Standard. *J. Vac. Sci. Technol., A* **1995**, *13*, 1239–1246.

Chapter **4**

Publication III: Microscopic and spectroscopic analysis of ion-irradiated molecular-plated thin films for superheavy element production

The following article was published as full article in *Nuclear Instruments and Methods in Physics Research Section A: Accelerators, Spectrometers, Detectors and Associated Equipment*, volume 1075 in 2025. It describes the chemical and morphological changes of molecular plated thin films after ion beam irradiation.

4.1 Own contributions

Sample preparation was shared by the main author Carl-Christian Meyer and me. Support for the RBS and XPS analysis was provided.

4.2 Publication



Full Length Article



Microscopic and spectroscopic analysis of ion-irradiated molecular-plated thin films for superheavy element production

C.-C. Meyer^{a,b},* E. Artes^{a,b,c}, M. Bender^{c,g}, J. Brötz^d, Ch.E. Düllmann^{a,b,c}, T. Gouder^e, E. Jäger^c, B. Kindler^c, S. Herz^a, B. Lommel^c, M. Major^d, C. Mokry^{a,b}, F. Munnik^f, M. Rapps^{a,1}, D. Renisch^{a,b}, J. Runke^c, A. Seibert^e, C. Trautmann^{c,d}, N. Trautmann^a, O. Walter^e, A. Yakushev^c

^a Department Chemie - Standort TRIGA, Johannes Gutenberg-Universität Mainz, Fritz-Strassmann-Weg-2, 55128 Mainz, Germany

^b Helmholtz-Institut Mainz, Staudingerweg 18, 55128 Mainz, Germany

^c GSI Helmholtzzentrum für Schwerionenforschung GmbH, Planckstraße 1, 64291 Darmstadt, Germany

^d Technische Universität Darmstadt - Materialwissenschaft, Peter-Grünberg-Straße 2, 64287 Darmstadt, Germany

^e European Commission, Joint Research Centre (JRC) - Karlsruhe, Hermann-von-Helmholtz-Platz 1, 76344 Eggenstein-Leopoldshafen, Germany

^f Helmholtz-Zentrum Dresden-Rossendorf, Ion Beam Center, Bautzner Landstraße 400, 01328 Dresden, Germany

[§] Hochschule RheinMain, Am Brückweg 26, 65428 Rüsselsheim, Germany

ARTICLE INFO

Keywords:

Target preparation
Molecular plating
Electrochemical deposition
Raman microscopy
Lanthanide

ABSTRACT

The heaviest known elements are produced via fusion reactions by bombarding actinide targets with intense heavy ion beams. The production of actinide targets relies mainly on the molecular plating (MP) technique. Long-term stability of MP produced targets is typically achieved by a conditioning procedure, in which fresh targets are exposed to successively increasing beam intensities. This leads to non-trivial physical and chemical transformations, which are presently poorly understood. To shed light on processes in the initial irradiation stage, we irradiated thin Tm MP films with Cl and Au ions of different fluences, with the latter ranging from $10^{10} \frac{\text{ions}}{\text{cm}^2}$ to $10^{14} \frac{\text{ions}}{\text{cm}^2}$, and analyzed their morphology and composition by a variety of microscopic, spectroscopic and ion beam techniques. The study was conducted on lanthanide targets, which serve as non-radioactive analogues for heavy actinide targets. Combining the results of several methods, we conclude that the MP thin films consist of a mixture of carbonates and formates. Under irradiation, these films transform into amorphous oxides with embedded carbon clusters.

1. Introduction

In recent decades, remarkable progress has been made in the production of superheavy elements (SHE) [1–4]. For this purpose, targets of the heaviest actinides, such as ^{242}Pu [5], ^{243}Am [6,7] and ^{249}Bk [8], were irradiated with ^{48}Ca ions at heavy-ion accelerators. Actinide targets are typically produced by molecular plating (MP), where the desired actinides are electrochemically deposited as thin films ($\frac{\mu\text{g}}{\text{cm}^2}$) on very thin Ti foils (1.5 μm to 2.3 μm) [9]. The MP method presents a critical limitation to experimental progress in the field [10–12], as it is unable to produce targets of sufficient thickness to cover the full useful width of the excitation functions [12,13]. Given the large solid angle acceptances of current recoil separators and the overall detection efficiency of current experimental setups, production rates can almost exclusively be increased by using more intense ion beams

and/or thicker targets [14–18]. Both options require the development of actinide targets with improved stability. At present, the MP method is unable to take full advantage of the higher beam intensities that are now available [2,10,11]. A prerequisite for new target developments is a profound understanding of the existing MP method and the behavior of MP targets in the ion beam. Despite numerous publications on the MP method, the exact process of molecular plating and thus the properties of the MP thin films remain rather unknown. A brief current literature overview can be found in [19].

MP targets have sometimes limited stability after production and are usually conditioned on-line [20,21] using progressively increasing heavy-ion beam intensities over the course of a few hours. Bake-in procedures at GSI are done at earliest available beamtimes after target fabrication or alternatively directly at the beginning of a SHE production run, e.g., during adjustments of the experimental setup.

* Corresponding author at: Department Chemie - Standort TRIGA, Johannes Gutenberg-Universität Mainz, Fritz-Strassmann-Weg-2, 55128 Mainz, Germany.
E-mail address: cmeyer02@uni-mainz.de (C.-C. Meyer).

¹ Deceased.

Examples for this are ^{243}Am targets used at TASCA (TransActinide Separator and Chemistry Apparatus) in 2012 for spectroscopy experiments on Mc ($Z=115$) decay chains [6], and later Nh ($Z=113$) and Mc ($Z=115$) chemistry studies [7]. Or ^{244}Pu targets produced in 2014 for chemical studies of Fl ($Z=114$) [22,23] as well as for Fl nuclear spectroscopy studies [5,24,25]. Without conditioning, the actinide thin films may experience limited adherence to their backing. After bake-in, though, even storage for months or years under normal conditions in air has no effect on the performance of such baked-in targets. The chemical processes involved in different conditioning procedures are still unknown, but attempts have already been made to develop offline equipment in order to make progress in this field without irradiation time at an accelerator [26,27].

For SHE production experiments, special MP targets are fabricated from actinide isotopes, which usually are α -emitters [28]. α -Spectroscopic studies of the target layer show that the width of the α -lines undergoes a change [20,21] as the beam fluence increases, indicating a radiation-induced alteration in the material. These modifications are initiated by a relatively low ion dose and then remain constant throughout the entire SHE production experiment. Changes in the morphology of actinide thin films were also documented by photographic images [20,21], Atomic Force Microscopy (AFM) [29] and Scanning Electron Microscopy (SEM) [29]. Analytical methods have so far been limited to Energy Dispersive X-ray spectroscopy (EDX) [29] and conventional X-ray Diffraction (XRD) [29]. Both methods are challenged by the peculiarities of the current MP target technology and characterized by a poor signal-to-noise ratio. Initial research using Raman spectroscopy on thin ion-irradiated lead films [26,27] as a model system for accelerator targets has demonstrated the conversion of carbonates into oxides.

A more detailed examination of MP-produced films and research into the conditioning process would benefit from access to state-of-the-art analytical techniques. Furthermore, the analysis of actinide films necessitates the use of licensed laboratories with the corresponding handling permits. To circumvent this issue, we thus replaced the actinides with lanthanide targets. Actinides elements with $Z \geq 95$ are chemically very similar to lanthanides [30], rendering the latter ideal for initial studies and for the development of novel protocols for actinide target production [9,12,19]. The irradiation of lanthanide thin films serves as a preliminary stage for irradiation experiments on actinide thin films. Analyzing these films poses specific challenges due to their intricate morphology. Similar demands are present for both irradiated and non-irradiated films. The MP thin films produced and irradiated in this study were characterized using the following analytical methods (see Table 1):

- (i) SEM to examine morphological alterations.
- (ii) Various Ion Beam Analysis (IBA) techniques for elemental analysis, including Elastic Recoil Detection Analysis (ERDA), Rutherford Backscattering Spectrometry (RBS) and Particle-Induced X-ray Emission (PIXE).
- (iii) Raman and infrared (IR) spectroscopy to identify changes of functional groups.
- (iv) X-ray Photoelectron Spectroscopy (XPS) for identification of elements and their chemical state on the surface.
- (v) Grazing Incidence X-ray Diffraction (GIXD) to identify beam-induced structural changes of the MP films.

2. Experimental

2.1. Target production

The targets were prepared from analytical grade lanthanide nitrates (Merck KGaA Darmstadt). The used solvents, isopropanol and isobutanol, and the nitric acid were also of analytical quality (Merck KGaA Darmstadt). The Ti backings had 99.9% purity (Goodfellow). A solution

Table 1

List of studied samples and analytical methods applied. The uncertainty of the area density is assumed to be 10% based on an average of the density values given in the literature [32].

Sample name	Element	Area density $\frac{\mu\text{g}}{\text{cm}^2}$	SEM	Raman	IR	IBA	GIXD	XPS
Tb-50	Tb	50	x	x	-	-	-	-
Er-50	Er	50	x	x	-	-	-	-
Tm-50	Tm	50	x	x	-	-	-	-
Tm-500	Tm	500	-	x	x	-	x	x
Tm target-1	Tm	500	-	x	-	-	-	-
Tm target-2	Tm	500	-	x	-	x	-	-
Tm target-3	Tm	500	x	x	-	x	x	-
Tm target-4	Tm	500	x	x	-	x	x	-
Tm target-5	Tm	500	x	x	-	-	x	x
Tm target-6	Tm	500	-	x	x	-	-	x
HDZR-500	Tm	500	x	-	-	x	-	-

Table 2

List of irradiations. The first irradiation used $8.3 \frac{\text{MeV}}{\text{u}}$ Au^{26+} ions at the M3 beamline of the GSI Darmstadt. For damage characterization of the Au-irradiated samples by means of ion beam analysis (IBA), we used a $1.2 \frac{\text{MeV}}{\text{u}}$ Cl^{7+} beam at the HZDR. All samples have an area density of $500 \frac{\mu\text{g}}{\text{cm}^2}$. The uncertainty of the area density and of ion irradiations are estimated to be 10%.

Sample name	Element	1st irradiation $\frac{\text{Au ions}}{\text{cm}^2}$	IBA	2nd irradiation $\frac{\text{Cl ions}}{\text{cm}^2}$
Tm target-1	Tm	3.0×10^{11}	-	-
Tm target-2	Tm	5.0×10^{11}	x	2.0×10^{14}
Tm target-3	Tm	1.0×10^{12}	x	2.4×10^{14}
Tm target-4	Tm	3.0×10^{12}	x	2.4×10^{14}
Tm target-5	Tm	5.0×10^{12}	-	-
Tm target-6	Tm	1.0×10^{13}	-	-
HDZR-500	Tm	-	x	8.7×10^{13}

comprising a 9:1 ratio of isobutanol to isopropanol was employed for the deposition process. This ratio is the most commonly utilized solvent mixture for MP target production within our laboratory [28]. The lanthanides were then electrochemically deposited from this solution onto a $25 \mu\text{m}$ -thick Ti foil. The deposited area was circular with a diameter of 0.6 cm (area: 0.28 cm^2). The depositions were carried out galvanostatically at a constant current of $0.28 \mu\text{A}$ and for 1 h. The exact production method and the electrochemical cell construction are described in [28,31].

2.2. Target irradiation

Irradiations were performed at the materials research beamline M3 at the UNILAC accelerator at the GSI Helmholtz Centre for Heavy Ion Research in Darmstadt, Germany, using $8.3 \frac{\text{MeV}}{\text{u}}$ Au^{26+} ions. Homogeneous exposure of samples was achieved by using a slightly defocused beam. To prevent heating of the samples, the ion flux was kept below approximately $2.0(2) \times 10^9 \frac{\text{ions}}{\text{cm}^2 \text{ s}}$. The applied fluence ranged from 3.0×10^{11} to $1.0 \times 10^{13} \frac{\text{ions}}{\text{cm}^2}$ with an estimated uncertainty of about 10%. This accumulated fluence corresponds to the first few minutes of the target irradiation in a superheavy element production campaign and thus provides insight on the effects during the target conditioning process.

The parameters for the irradiations with Cl and Au ions are given in Table 3 together with comparative data for Ca ion irradiations applied earlier during bake-in procedures [27]; because ^{48}Ca has been the most important projectile of the SHE research during the last decades [2]. For the density of the MP films, we presume $2.73 \frac{\text{g}}{\text{cm}^3}$ [33] which is the density of a thulium carbonate and as such notably lower than that of thulium hydroxide and oxide.

The calculated ranges of the three different ion species exceed by far the thickness of 0.7 to $1.4 \mu\text{m}$ [29] or the achievable area density (about $500 \frac{\mu\text{g}}{\text{cm}^2}$) of the MP films, as shown in Table 3. In contrast to typical SHE experiments [11,12], where the beam first penetrates the backing and then enters the target thin film, our samples were positioned with the thin film facing the ion beam. This was also considered

Table 3

Beam parameters for the different irradiations of Tm targets including the total kinetic energy in MeV per nucleon (MeV/u), the electronic and nuclear stopping power, the applied fluence as well as the projected ion range as calculated with the SRIM-2013.00 code, assuming a thulium carbonate target density of 2.73 g cm^{-3} [33]. The dose D is the product of the energy loss and the accumulated fluence.

Ion	Energy [$\frac{\text{MeV}}{u}$]	(dE/dx)e [$\frac{\text{keV}}{\text{nm}}$]	(dE/dx)n [$\frac{\text{keV}}{\text{nm}}$]	Fluence [$\frac{\text{ions}}{\text{cm}^2}$]	Range [μm]	Range [$\frac{\mu\text{g}}{\text{cm}^2}$]	Dose [MGy]
^{35}Cl	1.2	3.3	6.1×10^{-3}	20×10^{13}	16	4452	388.94
^{197}Au	8.3	17.9	2.2×10^{-2}	1×10^{13}	109	29769	105.07
^{48}Ca	5.9	2.8	1.8×10^{-3}	7×10^{13}	85	23160	106.50

in the calculations presented. The total absorbed dose in Gray was calculated by multiplying the electronic energy loss per unit pathlength (dE/dx)e with the fluence.

2.3. Target characterization

2.3.1. Scanning electron microscopy and energy dispersive X-ray spectroscopy

In order to evaluate the ion beam-induced surface modifications, scanning electron microscopy (Philips XL30) with an acceleration voltage of 20 kV was used. In some cases, the samples were sputter-coated by a thin silver layer to avoid charging effects during imaging. The elemental composition of the thin films was investigated by EDX and analyzed with the NIST DTSA-II Lorentz software package [34].

2.3.2. Elastic recoil detection analysis

Some of the Tm targets were analyzed with Elastic Recoil Detection Analysis (ERDA) at the Ion Beam Center of the Helmholtz-Zentrum Dresden-Rossendorf (HZDR) using a $1.2 \frac{\text{MeV}}{u}$ Cl ion beam. The angle between the normal direction of the sample surface and the incoming beam was 75° , the scattering angle was 30° . The analyzed area was about $2 \times 2 \text{ mm}^2$. The recoil atoms and scattered ions were detected with a Bragg Ionisation Chamber (BIC), which enables energy measurements and Z identification of the particles. H recoils were detected with a separate solid state detector at a scattering angle of 40° . The beam fluence is monitored using a gold plated rotating vane (1 Hz) and a solid state detector, which detects Cl backscattering from Au. This system is calibrated against the ion beam current measured with a Faraday cup. The resulting fluences per sample are given in Table 2.

2.3.3. μ -beam - spatially resolved RBS and PIXE

Some of the Tm targets were analyzed with RBS and PIXE at HZDR using a 3 MeV proton beam. The beam was focused to about $7 \times 5 \mu\text{m}^2$. The backscattered protons were detected at a scattering angle of 174° with a silicon strip detector. A Ketek silicon drift detector collimated to 80 mm^2 was used to detect the X-rays emitted from the sample. The detector was placed outside the sample chamber. In addition, a $65 \mu\text{m}$ aluminium absorber was used to further reduce the contribution of the X-rays from the Ti substrate and stop back-scattered protons from entering the detector. RBS was used to obtain depth profiles of the main elements except H, which cannot be detected by RBS. For C, N, and O evaluated cross-sections from SigmaCalc are used [35]. For Ti, there is no accurate data in the relevant energy range and for the used scattering angle. Therefore a measurement on the Ti backing foil was performed to obtain non-Rutherford cross-sections, which was possible using the program NDF [36]. AFM measurements across the pristine Ti foil showed a substantial roughness of $\text{rms} = 39(8) \text{ nm}$. Thus the deduced cross-section might not be of universal validity.

In the case of the Tm thin films, a preliminary large-scale PIXE scan was conducted, after which individual areas of the thin film were selected for point measurements. All large PIXE scans contain 128×128 points or 128×100 points and have a size of $260 \times 260 \mu\text{m}^2$ or $260 \times 205 \mu\text{m}^2$, respectively.

2.3.4. Raman spectroscopy

Raman spectra from 50 cm^{-1} to 4000 cm^{-1} were collected with a Jobin Yvon (Horiba) LabRam HR 800 spectrometer equipped with an Olympus BX41 optical microscope and a Si-based charge-coupled device (CCD) detector. The instrumentation used a grating with $1800 \frac{\text{grooves}}{\text{mm}}$ and a slit width of 100 nm. Excitation wavelengths of 633 nm and 488 nm were used. These parameters, and the optical path length of the spectrometer led to a spectral resolution of 0.8 cm^{-1} . The spectral acquisition time was set to 40 s for all measurements. In order to exclude modifications due to laser irradiation, long-term measurements were carried out analogous to [37]. The Raman spectra were assessed using the Fityk software [38].

2.3.5. Infrared spectroscopy

IR spectra were recorded with a Bruker Alpha Platinum-ATR. For this purpose, the Bruker Platinum ATR monolithic diamond crystal was pressed onto the MP thin films and the spectra were recorded in the Attenuated Total Reflection (ATR) setup. The IR spectra were recorded after all other analytical work was completed, as the ATR mode may mechanically damage the surfaces. The spectra were recorded using Bruker OPUS software and analyzed by the Spectragryph software package [39].

2.3.6. X-ray photoelectron spectroscopy

For elemental analysis, several selected samples were investigated by XPS, some time (days up to months) after their preparation. Irradiated samples were stored under ambient air for even longer times and underwent several other characterization methods beforehand. During the measuring campaign the samples were stored in a UHV-chamber (base pressure about 2.0×10^{-8} mbar) neighboring the XPS analysis chamber. The base pressure in the XPS chamber was kept below 5.0×10^{-10} mbar. XPS measurements were conducted using a monochromatic Al K_α ($\lambda = 8.3395 \text{ \AA}$) X-ray source and a hemispherical analyzer Phoibos 150 with HAS 3500 plus controller (all from Specs, Berlin). The micro-focus high performance X-ray source XRC-1000 MF was equipped with a μ -FOCUS 500 monochromator (all from Specs, Berlin). XPS analysis and peak fitting were performed with CasaXPS [40] (Ver. 2.3.24 PR 1.0).

In general, charging effects result in a slight broadening of the Full Width Half Maximum (FWHM) and a shift of the XPS peaks. Such charge shifts can be corrected using a flood gun, which flushes the sample surface with low-energy electrons in order to compensate the charge. At the same time, the electron beam emitted by the flood gun can modify surface species [41,42]. Therefore, care has to be taken in the interpretation of the data.

2.3.7. Grazing incidence X-ray diffraction

In GIXD, a very small angle of incidence (ω) was chosen to limit the penetration depth of the photons to a thin surface layer of the film. The X-ray beam and sample were fixed to ensure a small angle of incidence ($\omega \approx 0.1\text{--}5^\circ$) while the detector moves at an angle of 2θ to collect diffraction signals. The structural information thus originates predominantly from the near-surface region ($< 400 \text{ nm}$). For the GIXD measurements, a SmartLab device from the Rigaku company with a rotating anode was used with Cu K_α radiation ($\lambda = 1.5406 \text{ \AA}$).

3. Results and discussion

3.1. Morphology of MP films

3.1.1. Non-irradiated samples

The molecular plating method produces thin films with a characteristic morphology consisting of individual tiles separated from neighboring tiles by deep cracks down to the substrate as shown in a representative SEM image (Fig. 1 right). This morphology is extensively described for the MP process [43,44] and is also referred to as

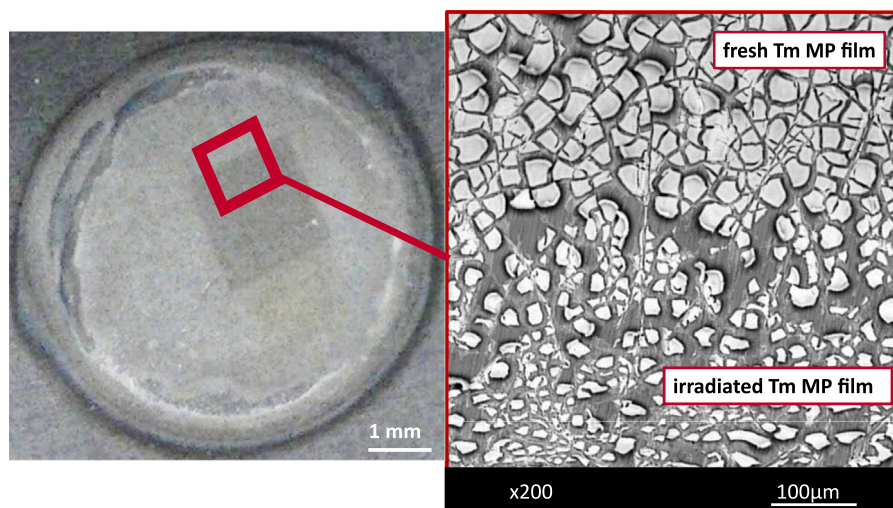


Fig. 1. Photograph (left) and SEM image (right) of a $500 \frac{\mu\text{g}}{\text{cm}^2}$ thick Tm target (sample: HZDR-500) after irradiation with $1.2 \frac{\text{MeV}}{\text{u}}$ Cl ions ($2.0 \times 10^{14} \frac{\text{ions}}{\text{cm}^2}$). On the photograph, the irradiated area is clearly visible as dark square.

mudcracking [19,45] or mud-caking [46,47]. Each material produces a different mudcracking pattern and minute changes in MP parameters can have a large impact on the morphologies [43,48]. Other methods of electrochemical deposition of lanthanides and actinides also describe a cracked surface structure [45,49–51]. Vascon et al. showed that the cracks form after plating during drying and that the individual tiles of the thin film are not smooth, but have a rough substructure [48]. The formation of surface cracks depends mainly on the chosen solvent (isobutanol:isopropanol, 9:1). It should be noted that the solvent was kept constant throughout our experimental series.

Our scanning electron microscopy images clearly show (Fig. 1 right), that mudcracking leads to a significant portion of the surface of MP targets becoming uncovered. This effect should be taken into account during irradiation experiments and when utilizing analysis methods without a micrometre spatial resolution such as ERDA, GIXD and IR spectroscopy, etc.

3.1.2. Irradiated samples

First we discuss morphological changes of a fresh Tm MP film caused by the irradiation with $1.2 \frac{\text{MeV}}{\text{u}}$ Cl ions (beam applied for ERDA). For an accumulated fluence of $2 \times 10^{14} \frac{\text{ions}}{\text{cm}^2}$, the changes in the irradiated area ($2 \times 2 \text{ mm}^2$) can easily be identified by the naked eye (Fig. 1 left). The sharp focus of the ion beam allows the interface between irradiated and non-irradiated area of the target to be displayed in one SEM image (Fig. 1 right) at high magnification. The SEM images of the two areas underline the difference; the characteristic tiles due to mudcracking are clearly visible in the non-irradiated area (Fig. 1 right). After the irradiation with $1.2 \frac{\text{MeV}}{\text{u}}$ Cl ions, the tiles barely cover the Ti backing, they shrank in size and are strongly deformed (Fig. 1 right).

We also inspected the morphological changes of samples exposed to a fluence series with $8.3 \frac{\text{MeV}}{\text{u}}$ Au²⁶⁺ ions (Fig. 2, 1a–1c) and subsequently analyzed the films by ERDA with $1.2 \frac{\text{MeV}}{\text{u}}$ Cl¹⁷⁺ ions (Fig. 2, 2a–2c). Up to the maximum applied Au ion fluence, the size of the tiles does not seem to change, but the uncovered area in between individual tiles becomes smaller. At the highest fluence ($3.0 \times 10^{12} \frac{\text{ions}}{\text{cm}^2}$), Tm covers the Ti backing almost without cracks. Comparable observations have been described for MP gadolinium films [29].

Samples that were irradiated with Au ions and then ERDA-analyzed with the high-intensity Cl beam are shown in Fig. 2, 2a–2c. Morphological changes were also observed in samples irradiated with Cl ions only. Individual tiles exhibit deformation and shrinkage, but the overall effects appeared to be less pronounced the larger the fluence of the preceding Au irradiation.

3.2. Ion beam analysis

Damage effects in samples exposed to $1.2 \frac{\text{MeV}}{\text{u}}$ Cl ions for ERDA were analyzed with a μ -beam RBS/PIXE. The border area between ERDA-irradiated and non-irradiated sample surface was examined, so that the influence of irradiation on the thin films could be studied (Fig. 4a). A sketch (Fig. 3) of the cross-section of the non-irradiated MP thin films, as derived from our microscopy images and the existing literature [31,52,53], illustrates the challenges in the application of ion beam methods in materials analysis.

3.2.1. Non-irradiated samples

The analysis of RBS and PIXE with a μ -beam made it possible to spectroscopically investigate individual tiles on the mudcracked surface. The element concentrations calculated from the RBS depth profiles for individual tiles of non-irradiated MP thin film (thickness $500 \frac{\mu\text{g}}{\text{cm}^2}$) are dominated by the elements C and O (Fig. 4c). Tm is only a minor component in atomic percent of the thin films. The N signal is characterized by a poor signal-to-noise ratio, which is why nitrogen is just barely detectable by RBS. Still, the weakness of the N signal suggests that we can exclude a significant deposition of nitrate species, which is consistent with other spectroscopic studies [48,52]. The Ti signal from the backing foil varies between individual tiles, which indicates that the tiles are of different thicknesses. The signal strength remained consistent across all tiles for the other elements. The depth profiles are obtained after analysis using the NDF-code [36] and conversion from the spectrum recorded during the RBS measurement. The film thicknesses obtained from the analysis are given in units of at/cm^2 . A conversion into a length unit is problematic as the mass density of the film is not precisely known. A length estimate based on the weighted average of the atomic densities gives a film thickness of about $2 \mu\text{m}$ for the μ -beam measurements (Fig. 4 (c,d)), which is consistent with our AFM and 3D laser scanning microscope measurements (not shown).

3.2.2. Irradiated samples

Comparing the PIXE data at the transition between non-irradiated and irradiated thin film (Fig. 4b), we first see that the elemental distribution of the PIXE map reproduces quite well the morphology of the MP thin films, as observed by SEM (Fig. 1 right). The higher intensity of the Tm-L signal is the result of Tm being accumulated in a smaller area. Furthermore, the distances between the Tm island or MP tiles are larger than in the non-irradiated area.

The RBS element analysis of the non-irradiated area (Fig. 4c) is dominated by C and O. Irradiation leads to the loss of most of the

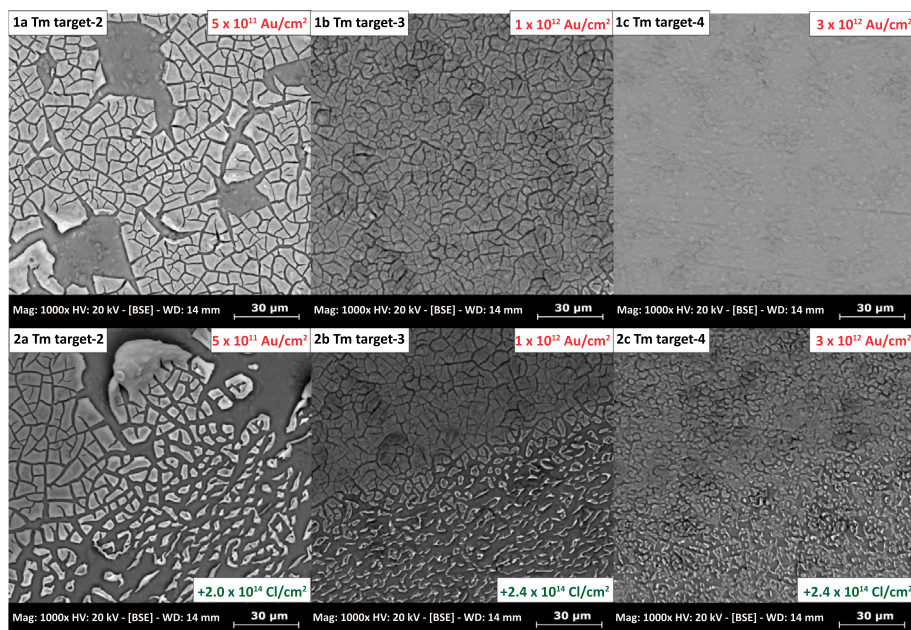


Fig. 2. SEM images of MP Tm thin films (thickness $500 \frac{\mu\text{m}}{\text{cm}^2}$, samples: Tm target-2 to Tm target-4) irradiated with different fluences. Top row (1a-1c): Tm films irradiated with $8.3 \frac{\text{MeV}}{\text{u}}$ Au ions at increasing fluence. Bottom row (2a-2c): same sample series after ERDA analysis using $1.2 \frac{\text{MeV}}{\text{u}}$ Cl ions of fluence 2.0×10^{14} to $2.4 \times 10^{14} \frac{\text{ions}}{\text{cm}^2}$. The lower series shows exactly the transition area of the ERDA analysis beam spot. Note that the SEM image 1c is slightly defocused, making the surface appear smoother than it really is.

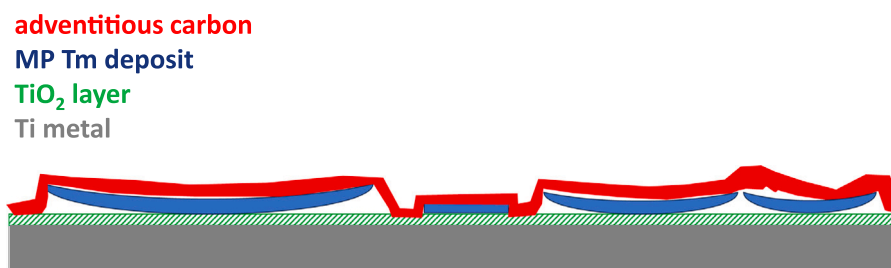


Fig. 3. Sketch of cross-section through the MP Tm film, to illustrate the difficulties of XPS, RBS and ERDA measurements due to tile formation, cracks and adventitious carbon contamination.

carbon. Due to the irradiation, the relative proportion of Tm increases, oxygen and Tm become the dominant components, C is detectable just above the measurement background and nitrogen is below the detection limit (Fig. 4d).

The ERDA investigation of the fluence series of Au-ion irradiated Tm samples (Fig. 5) confirms the decrease of the overall carbon and oxygen concentration as a function of fluence. The depth profile of the oxygen concentration fits well with the oxygen contents that were detected in the irradiated thin films by means of RBS. The carbon content determined by ERDA is higher than what was determined by the RBS measurements of irradiated thin films. The irradiation-induced alterations of the thin films, namely compaction and the loss of light elements, rendered the evaluation of the ERDA data a challenging endeavour. The ERDA measurements were further complicated by the morphology of the samples, a problem that is circumvented in RBS/PXIE measurements due to their superior spatial resolution. Collectively, the ERDA measurements align with the hypothesis that the irradiation with energetic heavy ions results in a depletion of C and O in MP thin films. Based on the results obtained from the ion beam methods, no significant beam-induced loss of Tm was observed. Instead, the combined PIXE/RBS/ERDA data suggest that the MP film tiles lose volatile components containing O and C, as a consequence of irradiation. This may result in chemical transformations that could potentially lead to the formation of a compound with a higher density, which in turn would result in a reduction of the area covered by the MP thin film.

We conclude from our data, that the determination of the elemental composition by the applied ion beam analysis was clearly at the limit of statistical significance for both non-irradiated and irradiated thin films. Techniques with high spatial resolution (e.g. using a μ -beam) are particularly suitable for overcoming challenges associated with the morphology of the MP films.

3.3. Vibrational spectroscopy

3.3.1. Non-irradiated samples

After achieving promising results using confocal Raman spectroscopy on lead model systems [26,27], we applied the method on a series of thin MP-produced lanthanide films including Tb, Er, and Tm (Fig. 6). The exceptional spatial resolution of this method enabled us to spectroscopically examine individual tiles, ensuring that the complex morphology and the presence of a Ti backing did not affect the accuracy of the measurements. Despite the thin Tb films exhibiting more pronounced mudcracking compared to Er and Tm, their Raman spectra are remarkably similar (Fig. 6). Furthermore, none of the samples exhibit any orientation-dependent behavior in their Raman spectra, indicating that they are in an amorphous or microcrystalline state composed of randomly oriented microcrystals [54].

The Raman spectra were recorded by means of the confocal Raman microscope using two different lasers with wavelengths, 473 nm and 633 nm, of the confocal Raman microscope. Several different tiles were

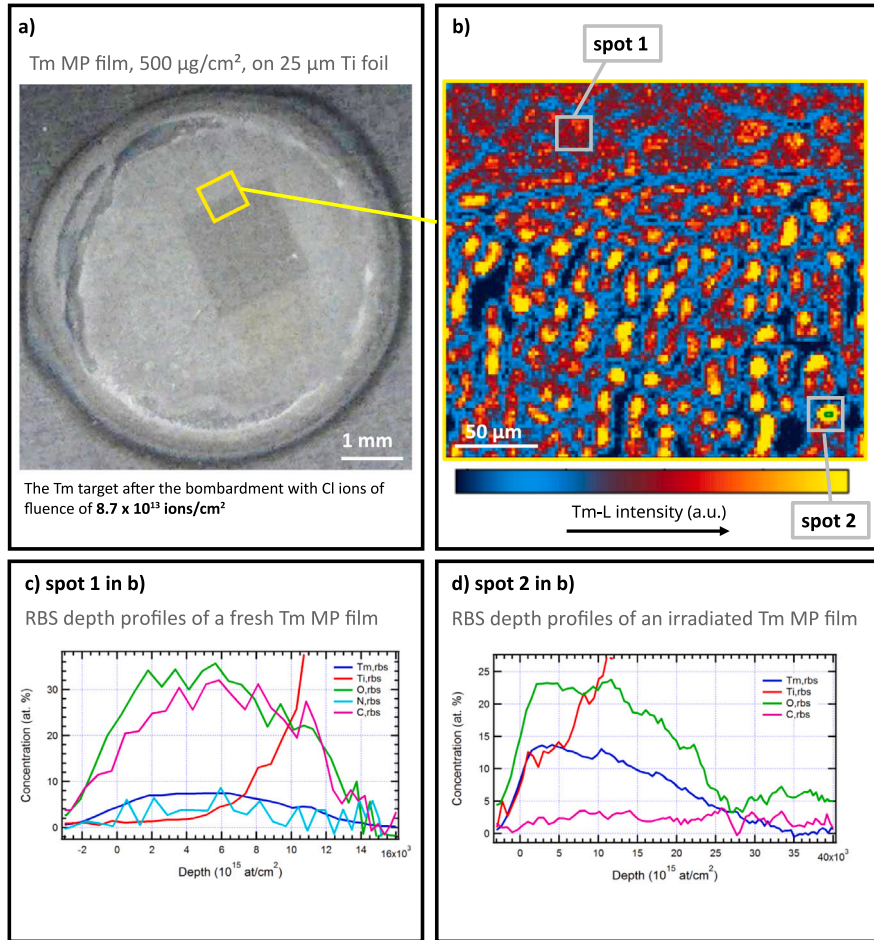


Fig. 4. (a) Photograph of MP Tm thin film (sample: HZDR-500) with yellow frame indicating the PIXE analyzed area performed after ERDA analysis with 8.7×10^{13} ions $\frac{\text{MeV}}{\text{cm}^2}$ of 1.2 MeV Cl ions. (b) PIXE map of non-irradiated (top area) and Cl-ion exposed area (bottom). The color code corresponds to high (yellow) and low (blue) Tm concentrations. Spot 1 and 2 indicate spots analyzed by μ -beam RBS analysis. (c) and (d) RBS data for various elements from spot 1 (non-irradiated) and spot 2 (Cl ion irradiated), respectively.

examined per sample in order to produce representative results for each sample. The spectra were identical for both excitation wavelengths and exhibited identical peak intensities. The ratio of the peak positions also remained constant, but the peak positions themselves fluctuated by about 3 cm^{-1} from measuring point to measuring point. According to [52], MP films are amorphous material, while the reference literature cited below refers exclusively to monocrystalline materials. For the final fit of the bands and the assignment to literature values, the spectrum with the lowest background was selected (Fig. 7).

In the Raman spectra of our Tb, Er and Tm films, carbonate [54–57] and formate [58–60] could be identified. Some Raman modes of the chemically closely-related anions overlap (Fig. 7). The identified bands are given in Table 4 and assigned to Raman modes where possible. Herzberg [61] nomenclature was used.

The wavenumber range from 50 to 700 cm^{-1} is characterized by a high background and a poor signal-to-noise ratio. We thus ignored this wave number regime for the analysis (Fig. 6). At larger wavenumbers, the spectrum is dominated by two bands, a sharp narrow peak (902 cm^{-1}), which can be assigned to the out-of-plane bend (ν_2) of the carbonate ion, as well as a multiplet (2733 to 3066 cm^{-1}), which is assigned to the C–H stretching vibration of the formate. Most of the other peaks in the spectrum can be assigned to either anion.

The free carbonate anion belongs to the point group D_{3h} and therefore has four vibrational transitions [55]. We assign the bands between 1560 to 600 cm^{-1} (Table 4) to coordinated carbonate. The four normal vibrational transitions are expected in a range from 1090 to 1070 cm^{-1} (ν_1), 930 to 850 cm^{-1} (ν_2), 1560 to 1420 cm^{-1} (ν_3) and 820 to 750 cm^{-1}

(ν_4). The splitting of the degenerate modes ν_3 and ν_4 may be caused by the symmetry reduction from D_{3h} to C_{2v} or C_s from the free to the coordinated carbonate anion [57]. In an amorphous phase all four vibrational transitions of the carbonate ions are expected to be both infrared and Raman active. Furthermore, one would expect that the degeneracy of the ν_3 and ν_4 modes for the free carbonate ions is lifted [55]. Detailed correlation schemes and group theory discussion of the spectroscopy of carbonate in solid phases can be found in [55–57]. The observed Raman spectra (Fig. 7) can therefore be partly explained by bound carbonate in an amorphous phase.

The free formate anion has the point group C_{2v} , thus six vibrational transitions can be derived from group theory [58–60]: The C–H stretch in the range from 3070 to 2730 cm^{-1} (ν_1), the O–C–O symmetric stretch from 1380 to 1360 cm^{-1} (ν_2), the O–C–O symmetric deformation from 820 to 750 cm^{-1} (ν_3), the O–C–O asymmetric stretch from 1610 to 1580 cm^{-1} (ν_4), the C–H in-plane bend from 1430 to 1420 cm^{-1} (ν_5) and the out-of-plane bend from 1080 to 1005 cm^{-1} (ν_6) [60]. Only the most intense bands at 2918 cm^{-1} and 2942 cm^{-1} can be unambiguously assigned to the C–H stretch (ν_1) of the formate [59], which is in good agreement with the reported literature values of 2920 cm^{-1} and 2949 cm^{-1} [58]. For the other transitions, no exactly measured or calculated values are given for thulium formates, but they are available for homologues from the lanthanide series. As in the case of carbonate, symmetry reduction in amorphous materials would be an explanation for the occurrence of bands that are in principle symmetry-forbidden bands in the Raman spectrum. The C–H stretching vibration (ν_1) is of particular importance in formates, thus its variation within the lanthanide series has been systematically studied [58,60].

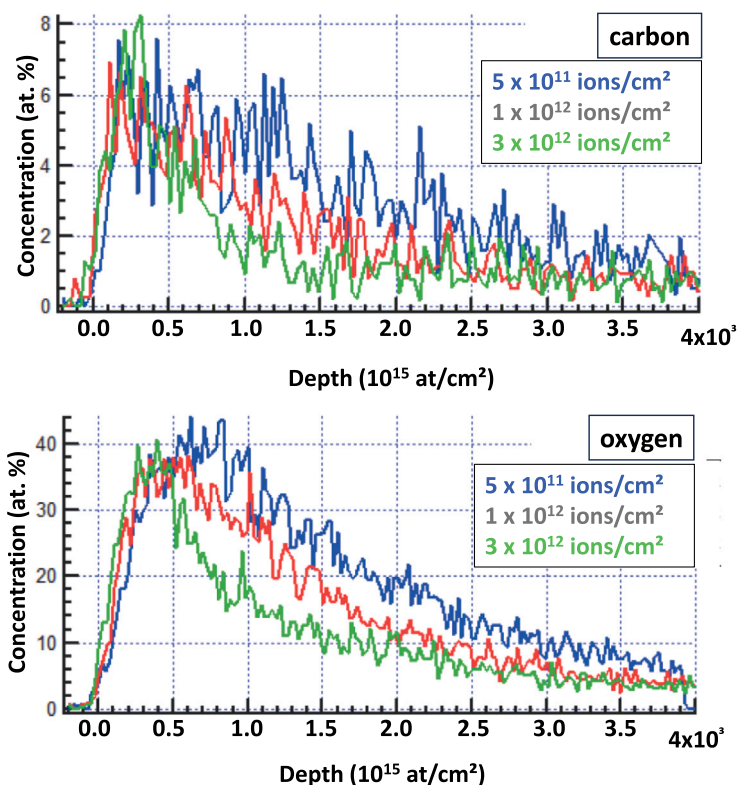


Fig. 5. C and O concentration as a function of depth deduced from ERDA spectra for MP Tm thin films (sample series Tm target-2 to Tm target-4). The contribution of both elements decreases with depth and with increasing fluence.

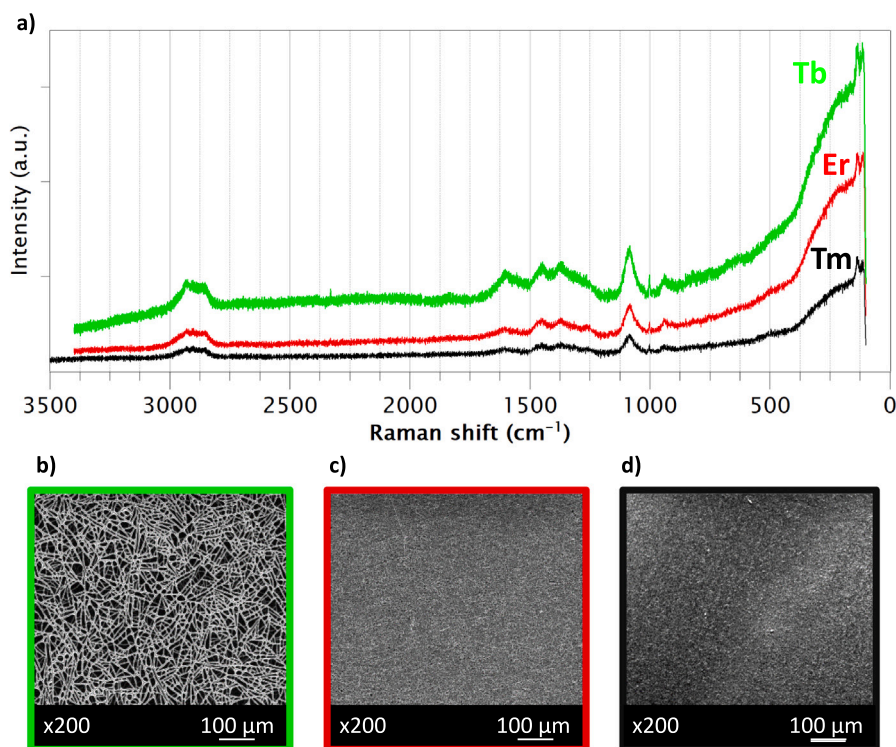


Fig. 6. (a) Raman spectra of Tb (sample Tb-50), Er (sample Er-50) and Tm (sample Tm-50) films of thickness: $50 \frac{\mu\text{m}}{\text{cm}^2}$ and (b)–(d) respective SEM images. Despite different morphologies, MP thin films of different lanthanides show the same Raman spectrum.

It should be mentioned that the nitrate anion also has a D_{3h} symmetry and should thus produce Raman bands similar to those of carbonates, which is how Raman spectra of uranium MP films were

interpreted [63]. However, due to the very different chemistry of uranium compared to lanthanides and heavy actinides, this interpretation of the Raman spectra cannot be applied. Other studies on uranium

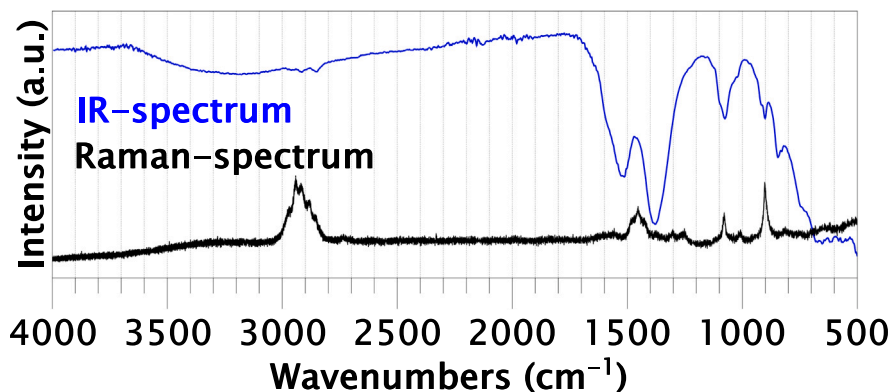


Fig. 7. Raman and IR spectrum of MP Tm thin film (thickness $500 \frac{\mu\text{g}}{\text{cm}^2}$, sample: Tm-500).

Table 4

Assignment of bands in the Raman and IR spectra of the non-irradiated MP Tm films, as designated by Herzberg [61].

Wavenumber	Method	Carbonate	Formate	References
401	IR		Unknown	
563	IR		Unknown	
619	IR	ν_{4a}	–	[62]
653	IR	ν_{4b}	–	[62]
673	IR	ν_{4c}	–	[62]
754	Raman	ν_{4a}	ν_{3a}	[55–58,60]
813	Raman	ν_{4b}	ν_{3b}	[55–58,60]
846	IR	ν_{2a}	–	[62]
901	IR	ν_{2b}	–	[62]
902	Raman	ν_2	–	[55–57]
1008	Raman	–	ν_{6a}	[60]
1076	IR	ν_1	–	[55–57]
1079	Raman	ν_1	ν_{6b}	[55–57,60]
1252	Raman		Unknown	
1302	Raman		Unknown	
1374	Raman	–	ν_{2a}	[58,60]
1379	IR	ν_{3a}	ν_{2a}	[58,60,62]
1423	Raman	ν_{3a}	ν_{5a}	[55–58,60]
1453	Raman	ν_{3b}	–	[55–57]
1476	Raman	ν_{3c}	–	[55–57]
1514	IR	ν_{3b}	–	[62]
1557	Raman	ν_{3d}	–	[55–57]
1583	Raman	–	ν_{4a}	[59,60]
1605	Raman	–	ν_{4b}	[59,60]
2733	Raman	–	ν_{1a}	[58–60]
2770	Raman	–	ν_{1b}	[58–60]
2882	Raman	–	ν_{1c}	[58–60]
2915	IR	–	ν_{4a}	[58]
2918	Raman	–	ν_{1d}	[58–60]
2942	Raman	–	ν_{1e}	[58–60]
2960	IR	–	ν_{4b}	[58]
3066	Raman	–	ν_{1f}	[58–60]

MP targets could not detect any nitrate in the thin films by Raman and IR [64] or XPS [65,66], and the thin films were reported to be nitrogen-free.

3.3.2. Irradiated samples

Fig. 8 shows spectra from a series of $8.3 \frac{\text{MeV}}{\text{u}}$ Au ion irradiations. With increasing fluence, the two most prominent Raman bands (at 1079 cm^{-1} (a) and at 2942 cm^{-1} (c)) disappear and two new bands (b) gradually emerge around 1590 cm^{-1} (1650 to 1480 cm^{-1}) and 1360 cm^{-1} (1440 to 1290 cm^{-1}).

The two new bands can be assigned to the D (1440 to 1290 cm^{-1}) and G (1650 to 1480 cm^{-1}) peaks, which are characteristic for graphite-like structures embedded into an oxide structure [67–69]. The G-band is the primary mode in graphene and graphite. It represents the planar configuration sp^2 -bonded carbon that constitutes graphene. The band is resonant, which means that it is much more intense than would

be expected otherwise. The D-band is known as the disorder band or the defect band. It represents a ring breathing mode from sp^2 carbon rings, though to be active the ring must be adjacent to a graphene edge or a defect. A significant D-band indicates defects to be present in the material. The intensity of the D-band is directly proportional to the level of defects in the sample [70]. In light of the aforementioned findings, it can be posited that the irradiated MP thin films can be characterized as amorphous oxides with embedded carbon clusters, as evidenced by the results of our Raman spectroscopy analysis [69].

The IR spectrum of the sample with the highest fluence is plotted together with the Raman spectrum of the same sample in Fig. 9. In the region of high wavenumbers, there is also IR activity that could be assigned to OH-oscillations. The hygroscopicity of the samples may be a potential explanation for the origin of these OH-oscillations. Otherwise, the IR spectrum of the irradiated samples does not permit further identification of chemical species. Yet, the appearance of oxycarbonates has been inferred from earlier GIXD and XPS studies [52], for lanthanum MP thin films that were heated to 700 K . However, Raman and IR spectra of these oxycarbonates [71] could not be identified in our films. Therefore, ion irradiation obviously induces a different form of transformation rather than pure heating [29].

3.4. X-ray photoelectron spectroscopy (XPS)

In the XPS overview spectra (not shown) of the MP Tm thin films the expected characteristic Tm, O, and C peaks as well as the peaks of Ti are visible. The Ti signal originates from the Ti backing due to the mudcracking morphology as illustrated in Figs. 1 and 3. The tiles do not completely cover the surface and therefore, the Ti backing (together with its oxide layer) is exposed to the analyzing X-ray beam.

The electrical conductivity of the MP films is rather poor, which favors charging effects [72,73] during the XPS measurement. As is typical for air-exposed samples, they are covered with so-called “adventitious carbon”, a layer of short-chain oxygen-containing organic carbon compounds. Together with charging effects, this makes the direct interpretation of the C1s spectra difficult [41,74]. Further, it is important to note that numerous authors report charge-corrected measured binding energies. Often, the dominant C1s peak is attributed to adventitious carbon and placed in a range of 284.5 to 285.5 eV . This approach leads to inconsistencies in the energy positions among different reports as the final charge-corrected binding energy is not necessarily accounting for the nature of different organic species [41,74]. Therefore in this experimental series we tried to avoid relying on the absolute, charge-corrected BE values, but rather used peak differences instead for our interpretations [42].

Despite the problems described in the previous paragraphs, we discuss in the following the change in C1s spectra under irradiation. The C1s region (Fig. 10) for the irradiated samples is less complex than that of the fresh MP samples. The number of carbon species needed

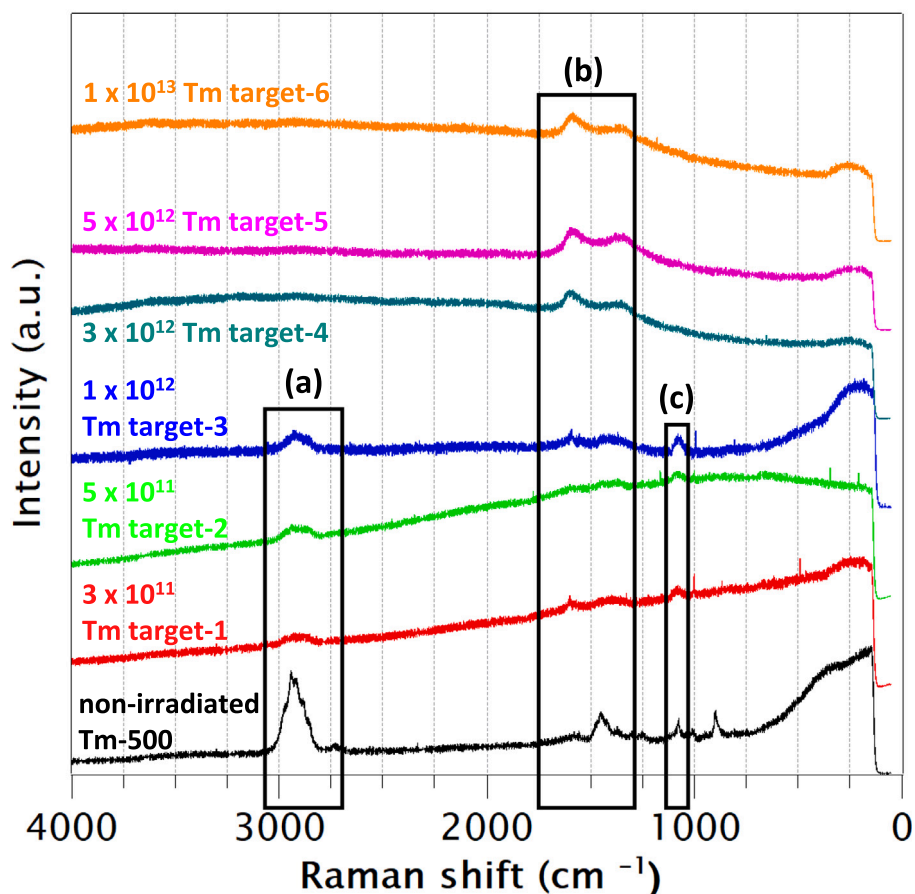


Fig. 8. Raman spectra of a Tm sample series (Table 2) irradiated with $8.3 \frac{\text{MeV}}{\text{u}}$ Au ions of different fluences. The boxes indicate the position of bands assigned to formate (a), graphite (D and G band) (b) and carbonate (c). The fluence is given in units of $\frac{\text{ions}}{\text{cm}^2}$.

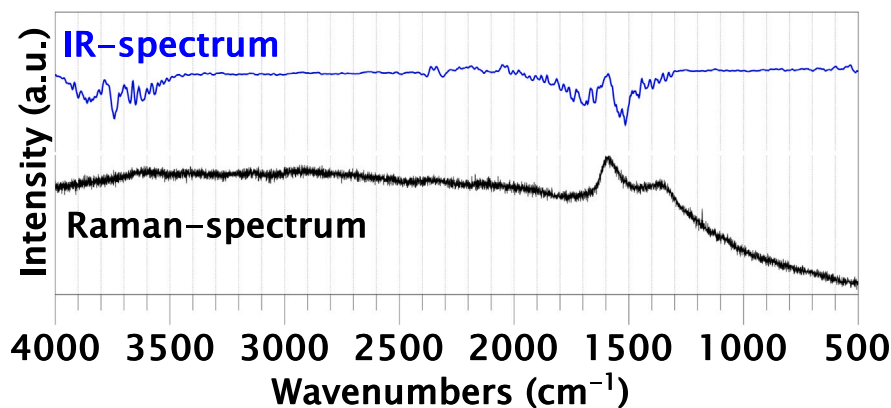


Fig. 9. IR and Raman spectra of MP Tm thin film (thickness $500 \frac{\text{Å}}{\text{cm}^2}$, sample: Tm target-6) after irradiation with $8.3 \frac{\text{MeV}}{\text{u}}$ Au ions of fluence $10^{13} \frac{\text{ions}}{\text{cm}^2}$.

to develop a peak model is reduced for the irradiated samples and the peak observed above 292 eV is absent after irradiation. Table 5 summarizes the assigned chemical species. Carbon species containing C–Cl and C–N bonds were excluded from consideration as no indications for the presence of Cl and N were obtained in XPS overview spectra, nor with other analytical methods like RBS or ERDA. Fluorine was observed only for the irradiated films (samples Tm target-5 and Tm target-6) and is assumed to be due to surface contamination during sample handling or storage in an UHV-chamber. We ascribe the peaks in the C1s XPS spectra to the following three carbon species: (i) a thin layer of adventitious carbon-containing material on the conductive

Ti [74], (ii) the same layer on the MP thin film and (iii) the confirmed carbon species in the MP thin film itself.

The C1 peak is interpreted to represent the C–C/C–H contribution of the adventitious carbon on the Ti backing (Fig. 10). This is supported by the absence of the peak when no Ti is detected in overviews and Ti2p detail spectra. The Binding Energy (BE) corresponds to the value measured on a blank Ti reference backing (not shown) without deposited film. The superposition of the peaks in the irradiated samples (Fig. 10b and 10c) illustrates a major problem of interpretation. The main peak can be fitted with variable proportions of adventitious carbon contributions, i.e. both C1 and C2 species in variable proportions. This discrepancy is likely due to the challenging morphology of the samples,

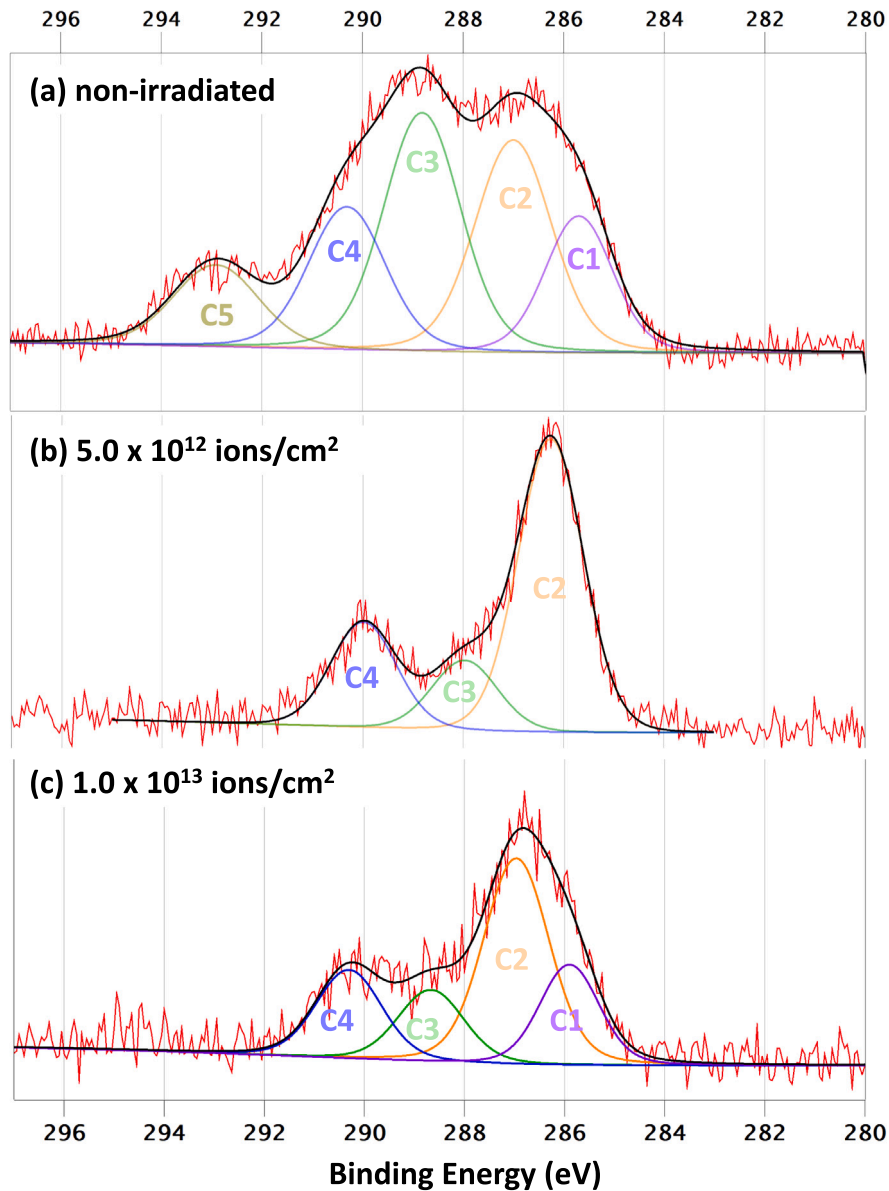


Fig. 10. C1s XPS spectra of MP Tm samples together with fits of individual carbon species for non-irradiated sample (top) and two samples irradiated with $8.3 \frac{\text{MeV}}{\text{u}}$ Au ions of different fluence. The samples shown are Tm-500 (a), Tm target-5 (b) and Tm target-6 (c).

Table 5
Measured Binding Energy (BE) and Chemical Shift (CS) of different carbon species.

Peak	BE eV	CS eV	Possible species
C1	285.7		C-C/C-H contrib. of advent. carbon on Ti backing [74]
C2	286.3–287.0		C-C/C-H contrib. of advent. carbon on MP Tm film [74]
C3	287.9–288.8	1.5–1.8	C-O-C, C-OH, C*-O-G=O [40]
C4	290.0–290.4	3.3–3.7	C-O-C*=O HCOO [40]
C5	292.8–292.9	5.9	O-C(-O)-2 [40]

in addition to the limitations of the XPS method, such as charging effects.

Given the intricate surface morphology of the samples and the ion-beam-induced inconsistency in the XPS spectra, a quantification of the Tm-C ratio was deemed to be unreliable and unsound. Additionally, the issue of adventitious carbon (Table 5) on the Ti backing alone would have rendered further calculations even more arbitrary.

However, the clear change in the C1s spectra induced by the ion irradiation can be reconciled with the results of Raman spectroscopy and ion beam analysis, which suggest that the freshly deposited formates,

(hydroxo)carbonates, hydroxides change under irradiation to a more oxidic species with intercalated carbon clusters.

Also in the O1s region distinct differences between the freshly deposited and the irradiated samples are observed (Fig. 11a). Again, a BE component at 532 eV is observed that correlates with the presence of Ti in the spectra. This is likely due to an oxidized Ti surface (TiO_2). For the blank Ti reference sample, an oxidized layer was observed as well. Another assignment possibility would be a thulium oxide component [75]. In a freely accessible database for XPS spectra, Tm_2O_3 is characterized by a double peak, the peak energy is given as 532 eV.

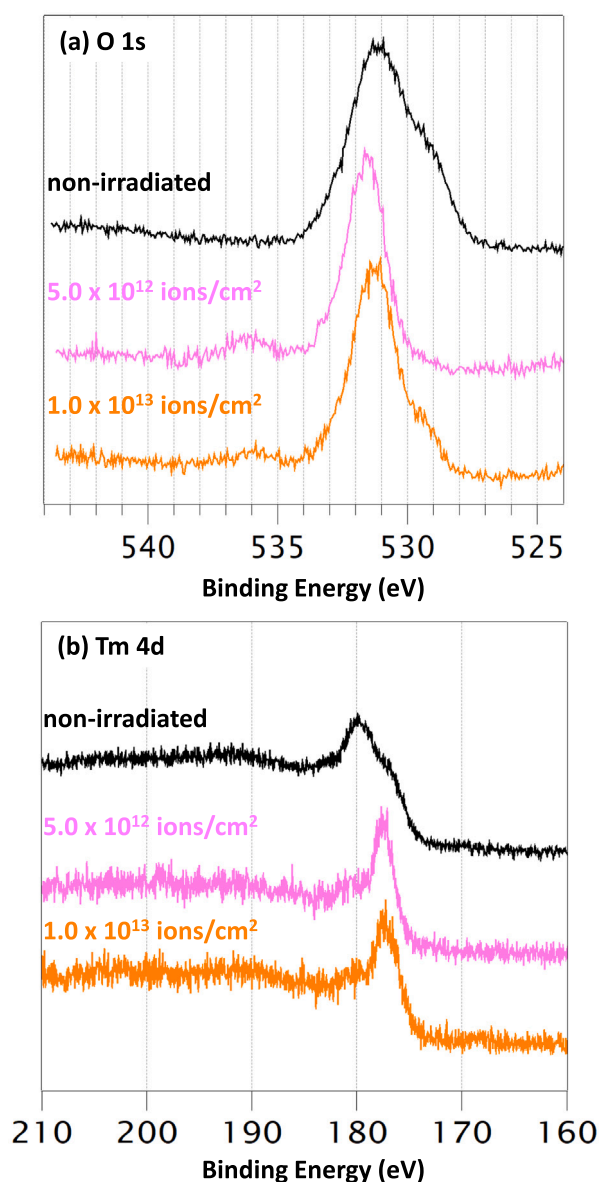


Fig. 11. (a) O1s and (b) Tm4d XPS spectra of MP Tm samples for a non-irradiated sample (top) and two samples irradiated with $8.3 \frac{\text{MeV}}{\text{u}}$ Au ions of different fluence. The samples shown are Tm-500 (black), Tm target-5 (pink) and Tm target-6 (orange).

In principle, the O1s peaks of metal oxides are characterized by a narrow peak shape, while the peaks of carbonates or formates should be broader. The shoulder at 529 eV in the non-irradiated samples could be explained by carbonate or formate based on the other analysis results, but this is not certain due to the inconclusive energy calibration. Furthermore, metal carbonates would be expected at higher, not lower BE than metal oxides [53]. Thus, no clear, unambiguous conclusion can be drawn from the O1s spectra alone.

In the Tm4d region differences are observed between non-irradiated and irradiated samples (Fig. 11b). While the fresh samples display a double peak structure for the 4d maximum, this is not distinctly seen for the irradiated samples. The double-peak structure in the Tm4d spectrum of the non-irradiated MP samples may be due to a differential charge shift effect that is not fully compensated by the flood gun, the intrinsic shape of the deposited material, or a superposition of different chemical species.

3.5. X-ray diffraction

For structural analysis of our thin films, X-ray diffraction under grazing incidence was performed (Fig. 12). Non-irradiated MP thin films yield only three broad and weak reflections, which can be best fitted with thulium formate [58,76,77]. Based on the half-width of the reflexes, the size of the crystallites in the sample that contribute to the reflex can be deduced. The diffraction pattern of our samples is thus indicative of the amorphicity of the phases and is consistent with the literature for diffraction experiments on untreated lanthanum MP films on Ti foils [52]. The roughness of the Ti substrate [78,79] used also made the diffraction measurements more difficult and certainly contributes to the dominance of the Ti reflections. The characterization of irradiated MP films was unsuccessful. This is attributed to the further amorphization. Yet, future diffraction experiments with even smaller angles of incidence together with Synchrotron X-ray Diffraction (SXRD) could enable a reliable identification of the different crystallites in the MP thin films.

4. Summary

4.1. Characterization of fresh films prepared by molecular plating

Microscopic methods confirm that of thin Tm films produced by molecular plating on a Ti backing are fractured, exhibiting a mudcracking morphology (Fig. 1 right). The films are composed of individual tiles, which significantly impacts the applicability of various analysis methods (Fig. 3). The most accurate results were obtained using high spatial resolution analytical methods such as Raman and RBS/PIXE, which allowed us to analyze individual tiles.

Our XPS characterization showed that the fresh films do not contain significant amounts of N, although Tm was added as nitrates in diluted nitric acid in the MP process. This result for N agrees well with the literature for the MP process from alcoholic solvents [48,52]. Studies on the MP process with aqueous nitrates from DMF [80] also showed no significant N in the XPS spectra, which in this particular case, also excludes the intercalation of nitrogen-based solvent degradation products. Thus, nitrogen compounds, such as nitrates and their degradation products, can be excluded as a constituent component of MP thin films.

The C1s XPS spectra of non-irradiated MP films showed a whole range of different carbon species. Unambiguous chemical identification by XPS alone is not possible, but in accordance with literature [48,52,80] the assignment of the dominant carbon compounds in the MP thin film to the carbonates and a carboxylic acid-like species (Table 5) is apparent. The formation of carbonates right after electroplating can be excluded, because the phase diagrams in the literature [81] clearly show that at room temperature and under ambient concentration of carbon dioxide (about 600 ppm) in the laboratory air, the formation of lanthanide carbonates is negligible [82,83]. Therefore, it can be concluded that the formation of carbonates through the weathering of hydroxides and oxides is an unlikely mechanism. A similar behavior is to be expected for the production process of heavy actinide targets, but literature data are scarce. Experiments reported in [31,48] clearly showed that the C1s species are formed during the MP process and not by drying the thin films in laboratory air. In addition, several XPS studies [48,65,80] have demonstrated that the carbon species in MP thin films is not a surface phenomenon, but is intrinsic to the entire thin film.

The XPS oxygen spectra did not permit a clear identification of the chemical species of the MP thin films and could not be reconciled with the assignments of the C peaks. This is because different binding energies would be expected for carbonates or carboxylic acid-like species, but from our XPS analysis, which is afflicted by differential charging, a reliable determination of binding energies is not possible. Publications on XPS studies of MP thin films often neglect discussion of the oxygen spectra. However, in one XPS study [80] on samarium MP films, the

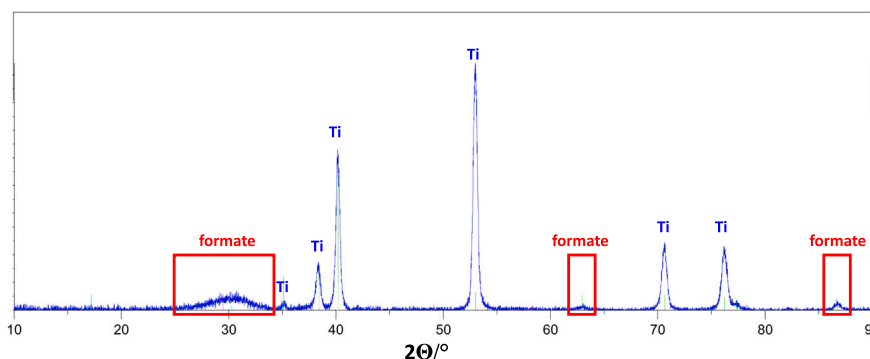


Fig. 12. GIXD diffractogram of non-irradiated MP Tm sample (sample: Tm-500), the red boxes show the reflections that can be assigned to thulium formate, while the sharp reflections originate from the Ti backing.

O1s spectra were discussed, and the observed O1s binding energy could be attributed to carbonates based on the observed C1s spectra.

Our ion beam analysis experiments also showed that C and O are the dominant species in fresh MP thin films. In both the ERDA (Fig. 5) and RBS (Fig. 4c and 4d) depth profiles, O and C dominate over the intended lanthanides in atomic percent. Again, a conclusive quantification of the MP film constituents was not possible, i.e., no sum formula of the MP thin films could be determined.

From GIXD measurements, we conclude that the MP films are amorphous and that Tm exists in the formate phase (Fig. 12). Due to the amorphous structure [52] of the MP thin films, as well as the roughness of the Ti backings, the results are not very clear. Moreover, the challenging morphology makes it difficult to interpret the GIXD data. By means of vibrational spectroscopy, carbonates and formates were identified as components of the fresh films (Fig. 7).

4.2. Chemical changes induced by heavy-ion irradiation

The irradiation of Tm MP thin films with $8.3 \frac{\text{MeV}}{\text{u}}$ Au ions induces drastic changes in morphology (Fig. 2). With increasing fluence, the cracks disappear and Tm becomes more and more homogeneously distributed across the entire surface. This effect has also been reported for MP plated Gd films [29]. Upon further irradiation with Cl ions of $1.2 \frac{\text{MeV}}{\text{u}}$, (characterized by a lower energy loss than the $8.3 \frac{\text{MeV}}{\text{u}}$ Au ions), films pre-irradiated with Au ions exhibit fewer morphological changes than non-irradiated films (Fig. 2).

Analysis by RBS revealed that the ion irradiation drastically reduces the C content of the MP thin films (Fig. 4). The RBS spectra of the irradiated films are dominated by O and Tm. Overall, the relative proportion of the target element is larger after irradiation, probably because a large fraction of volatile by-products from the MP process outgassed. This loss of unwanted material through the first irradiation could be an explanation for the beneficial effect of the conditioning process [20,21]. Our ERDA investigation showed that the loss of O and C increases with fluence (Fig. 5).

The XPS measurements of the irradiated MP films underline beam-effects on the C component (Fig. 10). No clear chemical species can be assigned. However, within the C1s peak, the loss of carbon species with higher binding energies, e.g. carbonates and formates, is obvious. The carbon species (Table 5) with the highest relative binding energy (C5, carbonate-like) disappears completely through irradiation. In contrast, an aliphatic carbon species (C2) is the dominant component of the MP thin films following irradiation. We were not able to identify by XPS compounds with higher binding energies as seen by Raman spectroscopy. Our XPS data clearly demonstrate the loss of carbon species and the disappearance of carbonates.

IR and Raman spectroscopy (Fig. 9) provide evidence for newly formed chemical species. Two characteristic Raman bands are visible

over a very high background, which fit an assignment to C nanoparticles [67,69]. In the IR spectra hydroxide bands were identified. Based on the overall spectroscopic findings, the irradiated MP thin films can be best described as amorphous oxide with embedded C nanoparticles.

5. Conclusion

The established models for the MP process assumed the formation of hydroxyl ions during deposition according to Hansen's theory [84–87]. Due to the non-reduction of the lanthanide or actinide cations [48,52,65,80], basic precipitation is assumed to occur by a combination of electrophoresis and electroplating [43]. The observed C content was explained by intercalated solvents and products of solvent decomposition. The analytical methods used in this study could not detect any decomposition products from the solvents used. The origin of observed C content is not clear, but organic solvents can dissolve much more carbon dioxide than, e.g., water can. At room temperature and normal pressure, the solubility of carbon dioxide in water is $0.033 \frac{\text{mol}}{\text{L}}$, $0.15 \frac{\text{mol}}{\text{L}}$ to $0.17 \frac{\text{mol}}{\text{L}}$ for short-chain alcohols and $0.18 \frac{\text{mol}}{\text{L}}$ for DMF [88]. Therefore, it can be assumed that moist and non-degassed organic solvents contain enough carbon dioxide to explain the formation of the carbonates that we observed. Another source for the input of carbon dioxide and thus carbonates could also be the used acids [89,90]. If we look at the Pourbaix diagram [91,92] of carbon dioxide, we see that formate can be formed from carbonates under the parameters described for the MP process, i.e., standard room temperature and partial pressure for carbon dioxide in ambient air. Due to the reductive basic conditions at the cathode, the carbonates are partially reduced to formates. It is precisely under these conditions that the oxidation of solvents, such as isopropanol and isobutanol, to carboxylic acid-like species seems very unlikely to occur as an explanatory model for the observed C1s XPS (Fig. 10) and Raman spectra (Fig. 7). However, should the solvents used be oxidized anodically and reach the cathode by diffusion, we or comparable studies [48,52,65,80] should have been able to detect these decomposition products. Neither studies in DMF [80] found nitrogen signals in the thin film, nor did we find the typical rotational spectra of short-chain alcohols. As with the carbonates, no conclusive mechanism is described in the literature for the formation of thulium formates by weathering of hydroxides and oxides that may have formed in humid laboratory air. Formate formation during the molecular plating process is the most obvious explanation, while a formation after plating seems to be unlikely. The resulting thin films can therefore be described as a mixture of amorphous basic carbonates and formates.

The chemical conversion of our samples differs significantly from the heat-induced conversion of MP thin films described in literature [46,52]. The oxycarbonate agglomerates reported are known thermal degradation products of carbonates [81] and formates [59]. Thermogravimetric investigations of related carboxylic acid-lanthanide compounds also indicate oxycarbonates as the final product before the

heat-induced transformation into the sesquioxides [71,93]. The chemical transformations we identified after the irradiation with heavy ions cannot be explained by a purely thermal process [29,94], since none of the known decomposition products were detected. Radiation-induced amorphousness could also be a reason for the lack of spectroscopic evidence. The response of the oxides of the lanthanides [95] and actinides [96] to irradiation with swift heavy ions has been extensively investigated for pure crystalline samples. Ion irradiation induces defect formation in the crystal and a loss of O. It would therefore be logical to attribute the chemical transformation of our MP films to a comparable mechanism [97]. This also includes the loss of light volatile elements, like C and O, so that the lanthanide oxide with embedded carbon clusters remain [69]. The relatively strong Raman-signal of the carbon clusters does not yield any information regarding their quantitative contribution to the MP thin film following irradiation. Based on the ion beam analyses, it can be inferred that irradiated thin films exhibit a significantly higher O than C content. Despite extensive research, we were unable to identify a satisfactory explanation for the observation that thin films previously irradiated with Au ions exhibit a reduced degree of morphological change when irradiated with Cl ions, in comparison to those that have not been irradiated.

Future studies would benefit from complementary microscopic techniques that offer sufficient spatial resolution enabling effective analysis despite the challenging morphology of the MP thin films. As the production of superheavy elements relies on actinide, and not on lanthanide targets, the presented studies will ideally also be performed with actinide targets. Such studies, though, require access to modern analytical methods in appropriate licensed nuclear analytical laboratories. These studies will ideally be complemented with irradiations applying higher fluences.

CRediT authorship contribution statement

C.-C. Meyer: Writing – review & editing, Writing – original draft, Project administration, Methodology, Investigation, Funding acquisition, Formal analysis, Data curation, Conceptualization. **E. Artes:** Investigation. **M. Bender:** Investigation. **J. Brötz:** Investigation. **Ch.E. Düllmann:** Writing – review & editing, Supervision, Project administration. **T. Gouder:** Investigation. **E. Jäger:** Investigation. **B. Kindler:** Investigation. **S. Herz:** Investigation. **B. Lommel:** Investigation. **M. Major:** Investigation. **C. Mokry:** Investigation. **F. Munnik:** Investigation. **M. Rapps:** Investigation. **D. Renisch:** Investigation. **J. Runke:** Investigation. **A. Seibert:** Investigation. **C. Trautmann:** Writing – review & editing, Supervision, Project administration. **N. Trautmann:** Supervision, Project administration. **O. Walter:** Investigation. **A. Yakushev:** Project administration, Investigation.

Declaration of Generative AI and AI-assisted technologies in the writing process

In the course of preparing this work, the authors employed the DeepL tool to enhance the readability and linguistic quality of the text. Following the utilization of this tool, the authors conducted a thorough review and editing of the content, assuming full responsibility for the content of the published article.

Declaration of competing interest

The authors declare that they have no known competing financial interests or personal relationships that could have appeared to influence the work reported in this paper.

Acknowledgments

We would like to thank our colleagues from the research reactor TRIGA Mainz for carrying out the neutron activation of the lanthanide standards. We also acknowledge the local support of the mechanical workshop at the TRIGA reactor site Mainz and the financial support from the Helmholtz Institute Mainz. We would like to thank our colleagues from the Department of Materials Science at the Technical University of Darmstadt for their helpful cooperation. The results presented here are based on experiments, which were performed at the beam lines X0 and X8 at the GSI Helmholtzzentrum für Schwerionenforschung, Darmstadt (Germany) in the frame of FAIR Phase-0. This project received funding from the German BMBF (project 05P21UMFN2). We express our gratitude to the Ion Beam Centre of the Helmholtz-Zentrum Dresden-Rossendorf for conducting the ion beam analysis of our samples. Access to the ActUsLab/PAMEC and ActUsLab/FMR facilities was granted under the Framework of access to the Joint Research Centre Physical Research Infrastructures of the European Commission (Research Infrastructure Access Agreement № 2020-1-RD-ActUsLab-FMR Targets-SHE1 (AUL-233) and 2020-1-RD-ActUsLab-PAMEC Targets-SHE2 (AUL-228)). Any opinions, findings and conclusions or recommendations expressed in this paper are those of the authors and do not necessarily reflect those of the European Commission.

Data availability

Data will be made available on request.

References

- [1] S. Hofmann, Synthesis and properties of isotopes of the transactinides, *Radiochim. Acta* 107 (9–11) (2019) 879–915.
- [2] S. Dmitriev, A. Popeko, High-power radioactive targets as one of the key problems in further development of the research program on synthesis of new superheavy elements, *J. Radioanal. Nucl. Chem.* 305 (2015) 927–933.
- [3] Y.T. Oganessian, S.N. Dmitriev, Synthesis and study of properties of superheavy atoms. Factory of superheavy elements, *Russ. Chem. Rev.* 85 (2016) 901.
- [4] O.R. Smits, C.E. Düllmann, P. Indelicato, W. Nazarewicz, P. Schwerdtfeger, The quest for superheavy elements and the limit of the periodic table, *Nat. Rev. Phys.* 6 (2) (2024) 86–98.
- [5] A. Sâmark-Roth, D. Cox, D. Rudolph, L. Sarmiento, B. Carlsson, J. Egido, P. Golubev, J. Heery, A. Yakushev, S. Åberg, et al., Spectroscopy along flerovium decay chains: Discovery of Ds-280 and an excited state in Cn-282, *Phys. Rev. Lett.* 126 (3) (2021) 032503.
- [6] D. Rudolph, U. Forsberg, P. Golubev, L. Sarmiento, A. Yakushev, L.-L. Andersson, A. Di Nitto, C.E. Düllmann, J. Gates, K. Gregorich, et al., Spectroscopy of element 115 decay chains, *Phys. Rev. Lett.* 111 (11) (2013) 112502.
- [7] A. Yakushev, J. Khuyagbaatar, C.E. Düllmann, M. Block, R. Cantemir, D. Cox, D. Dietzel, F. Giacoppo, Y. Hrbar, M. Iliáš, et al., Manifestation of relativistic effects in the chemical properties of nihonium and moscovium revealed by gas chromatography studies, *Front. Chem.* 12 (2024) 1474820.
- [8] Y.T. Oganessian, F.S. Abdullin, C. Alexander, J. Binder, R.A. Boll, S. Dmitriev, J. Ezold, K. Felker, J. Gostic, R.K. Grzywacz, et al., Experimental studies of the $^{249}\text{Bk} + ^{48}\text{Ca}$ reaction including decay properties and excitation function for isotopes of element 117, and discovery of the new isotope ^{277}Mt , *Phys. Rev. C—Nucl. Phys.* 87 (5) (2013) 054621.
- [9] B. Lommel, C.E. Düllmann, B. Kindler, D. Renisch, Status and developments of target production for research on heavy and superheavy nuclei and elements, *Eur. Phys. J.* 59 (2) (2023) 14.
- [10] C. Stodel, Methods of targets characterization, in: *EPJ Web of Conferences*, Vol. 229, EDP Sciences, 2020, p. 02001.
- [11] P. Steinegger, Open questions on chemistry in the synthesis and characterization of superheavy elements, *Commun. Chem.* 4 (1) (2021) 1–4.
- [12] C.E. Düllmann, E. Artes, A. Dragoun, R. Haas, E. Jäger, B. Kindler, B. Lommel, K.-M. Mangold, C.-C. Meyer, C. Mokry, et al., Advancements in the fabrication and characterization of actinide targets for superheavy element production, *J. Radioanal. Nucl. Chem.* 332 (5) (2023) 1505–1514.
- [13] C.-C. Meyer, E. Artes, M. Bender, J. Brötz, C.E. Düllmann, C. Haese, E. Jäger, B. Kindler, B. Lommel, M. Major, M. Rapps, D. Renisch, C. Trautmann, A. Yakushev, Fabrication, swift heavy ion irradiation, and damage analysis of lanthanide targets, *Radiochim. Acta* 111 (11) (2023) 801–815.
- [14] K. Morita, SHE research at RIKEN/garis, *Nucl. Phys. A* 944 (2015) 30–61.

- [15] C. Stodel, J.F. Libin, C. Marry, F. Lutton, M.G. Saint-Laurent, B. Bastin, J. Piot, E. Clement, S. Le Moal, V. Morel, et al., High intensity targets stations for S 3, *J. Radioanal. Nucl. Chem.* 305 (2015) 761–767.
- [16] S. Dmitriev, M. Itkis, Y.T. Oganessian, Status and perspectives of the dubna superheavy element factory, in: *EPJ Web of Conferences*, Vol. 131, EDP Sciences, 2016, p. 08001.
- [17] H. Haba, A new period in superheavy-element hunting, *Nat. Chem.* 11 (1) (2019) 10–13.
- [18] C.E. Düllmann, M. Block, F.P. Heßberger, J. Khuyagbaatar, B. Kindler, J.V. Kratz, B. Lommel, G. Müntenberg, V. Pershina, D. Renisch, et al., Five decades of GSI superheavy element discoveries and chemical investigation, *Radiochim. Acta* 110 (6–9) (2022) 417–439.
- [19] E. Artes, C.E. Düllmann, C.-C. Meyer, D. Renisch, The process of molecular plating and the characteristics of the produced thin films—what we have learned in 60 years and what is still unknown, in: *EPJ Web of Conferences*, Vol. 285, EDP Sciences, 2023, p. 03001.
- [20] S. Hofmann, S. Heinz, R. Mann, J. Maurer, J. Khuyagbaatar, D. Ackermann, S. Antalic, W. Barth, M. Block, H. Burkhardt, et al., The reaction $^{48}\text{Ca} + ^{248}\text{Cm} \rightarrow ^{296}116^*$ studied at the GSI-SHIP, *Eur. Phys. J.* 48 (5) (2012) 1–23.
- [21] N. Brewer, V. Utyonkov, K.P. Rykaczewski, Y.T. Oganessian, F.S. Abdullin, R. Boll, D.J. Dean, S. Dmitriev, J.G. Ezold, L. Felker, et al., Search for the heaviest atomic nuclei among the products from reactions of mixed-Cf with a ^{48}Ca beam, *Phys. Rev. C: Nucl. Phys.* 98 (2) (2018) 024317.
- [22] A. Yakushev, J.M. Gates, A. Türler, M. Schädel, C.E. Düllmann, D. Ackermann, L.-L. Andersson, M. Block, W. Bröchle, J. Dvorak, et al., Superheavy element flerovium (element 114) is a volatile metal, *Inorg. Chem.* 53 (3) (2014) 1624–1629.
- [23] A. Yakushev, L. Lens, C.E. Düllmann, J. Khuyagbaatar, E. Jäger, J. Krier, J. Runke, H. Albers, M. Asai, M. Block, et al., On the adsorption and reactivity of element 114, flerovium, *Front. Chem.* 10 (2022) 976635.
- [24] D.M. Cox, A. Sămark-Roth, D. Rudolph, L.G. Sarmiento, R.M. Clark, J.L. Egido, P. Golubev, J. Heery, A. Yakushev, S. Åberg, H.M. Albers, M. Albertsson, M. Block, H. Brand, T. Calverley, R. Cantemir, B.G. Carlsson, C.E. Düllmann, J. Eberth, C. Fahlander, U. Forsberg, J.M. Gates, F. Giacoppo, M. Götz, S. Götz, R.-D. Herzberg, Y. Hrabar, E. Jäger, D. Judson, J. Khuyagbaatar, B. Kindler, I. Kojouharov, J.V. Kratz, J. Krier, N. Kurz, L. Lens, J. Ljungberg, B. Lommel, J. Louko, C.-C. Meyer, A. Mistry, C. Mokry, P. Papadakis, E. Parr, J.L. Pore, I. Ragnarsson, J. Runke, M. Schädel, H. Schaffner, B. Schausten, D.A. Shaughnessy, P. Thörle-Pospiech, N. Trautmann, J. Uusitalo, Spectroscopy along flerovium decay chains. II. Fine structure in odd- A ^{289}Fl , *Phys. Rev. C: Nucl. Phys.* 107 (2023) L021301.
- [25] D. Cox, A. Sămark-Roth, D. Rudolph, L. Sarmiento, C. Fahlander, U. Forsberg, P. Golubev, J. Heery, A. Yakushev, H. Albers, et al., Spectroscopic tools applied to flerovium decay chains, in: *J. Phys. Conf. Ser.*, Vol. 1643, IOP Publishing, 2020, 012125.
- [26] R. Haas, C.-C. Meyer, S. Böhlend, C.E. Düllmann, J. Mäder, K. Tinschert, ODIn - a setup for off-line deposit irradiations of thin layers for nuclear physics applications, *Nucl. Instrum. Methods Phys. Res. Sect. A* 957 (2020) 163366.
- [27] C.-C. Meyer, A. Dragoun, C.E. Düllmann, R. Haas, E. Jäger, B. Kindler, B. Lommel, A. Prosvetov, M. Rapps, D. Renisch, et al., Chemical conversions in lead thin films induced by heavy-ion beams at Coulomb barrier energies, *Nucl. Instrum. Methods Phys. Res. Sect. A* (2022) 166365.
- [28] K. Eberhardt, C.E. Düllmann, R. Haas, C. Mokry, J. Runke, P. Thörle-Pospiech, N. Trautmann, Actinide targets for fundamental research in nuclear physics, in: *AIP Conference Proceedings*, Vol. 1962, AIP Publishing LLC, 2018, 030009.
- [29] D. Mayorov, E. Tereshatov, T. Werke, M. Frey, C. Folden III, Heavy-ion beam induced effects in enriched gadolinium target films prepared by molecular plating, *Nucl. Instrum. Methods Phys. Res. Sect. B* 407 (2017) 256–264.
- [30] S. Cotton, Lanthanide and Actinide Chemistry, John Wiley & Sons, Ltd, 2013.
- [31] A. Vascon, S. Santi, A. Isse, T. Reich, J. Drebert, H. Christ, C.E. Düllmann, K. Eberhardt, Elucidation of constant current density molecular plating, *Nucl. Instrum. Methods Phys. Res. Sect. A* 696 (2012) 180–191.
- [32] J. Runke, C.E. Düllmann, K. Eberhardt, P. Ellison, K. Gregorich, S. Hofmann, E. Jäger, B. Kindler, J. Kratz, J. Krier, et al., Preparation of actinide targets for the synthesis of the heaviest elements, *J. Radioanal. Nucl. Chem.* 299 (2) (2014) 1081–1084.
- [33] P. Caro, J. Sawyer, L. Evning, The infrared spectra of rare earth carbonates, *Spectrochim. Acta A* 28 (6) (1972) 1167–1173.
- [34] D.E. Newbury, N.W. Ritchie, Performing elemental microanalysis with high accuracy and high precision by scanning electron microscopy/silicon drift detector energy-dispersive X-ray spectrometry (SEM/SDD-EDS), *J. Mater. Sci.* 50 (2) (2015) 493–518.
- [35] A. Gurbich, SigmaCalc recent development and present status of the evaluated cross-sections for IBA, *Nucl. Instrum. Methods Phys. Res. Sect. B* 371 (2016) 27–32.
- [36] N. Barradas, C. Jaynes, R. Webb, Simulated annealing analysis of rutherford backscattering data, *Appl. Phys. Lett.* 71 (2) (1997) 291–293.
- [37] L. Burgio, R.J. Clark, Library of FT-Raman spectra of pigments, minerals, pigment media and varnishes, and supplement to existing library of Raman spectra of pigments with visible excitation, *Spectrochim. Acta A* 57 (7) (2001) 1491–1521.
- [38] M. Wojdyr, Fityk: A general-purpose peak fitting program, *J. Appl. Crystallogr.* 43 (5–1) (2010) 1126–1128.
- [39] F. Menges, Spectragryph-optical spectroscopy software, version 1.2. 14, 2020, 2020.
- [40] N. Fairley, Casaxps VAMAS processing software, 2010, <http://www.casaxps.com>.
- [41] D.R. Baer, K. Artyushkova, H. Cohen, C.D. Easton, M. Engelhard, T.R. Gengenbach, G. Greczynski, P. Mack, D.J. Morgan, A. Roberts, XPS guide: Charge neutralization and binding energy referencing for insulating samples, *J. Vac. Sci. Technol. A* 38 (3) (2020) 031204.
- [42] C.D. Easton, C. Kinnear, S.L. McArthur, T.R. Gengenbach, Practical guides for x-ray photoelectron spectroscopy: Analysis of polymers, *J. Vac. Sci. Technol. A* 38 (2) (2020) 023207.
- [43] F. Kurth, J. Froemel, S. Tanaka, M. Esashi, T. Gessner, Electroplating of neodymium iron alloys, in: 2016 IEEE 11th Annual International Conference on Nano/Micro Engineered and Molecular Systems, NEMS, IEEE, 2016, pp. 405–408.
- [44] D. Liebe, K. Eberhardt, W. Hartmann, T. Häger, A. Hübner, J. Kratz, B. Kindler, B. Lommel, P. Thörle, M. Schädel, et al., The application of neutron activation analysis, scanning electron microscope, and radiographic imaging for the characterization of electrochemically deposited layers of lanthanide and actinide elements, *Nucl. Instrum. Methods Phys. Res. Sect. A* 590 (1–3) (2008) 145–150.
- [45] M.N. Torrico, R.A. Boll, M. Matos, Electrodeposition of actinide compounds from an aqueous ammonium acetate matrix: Experimental development and optimization, *Nucl. Instrum. Methods Phys. Res. Sect. A* 790 (2015) 64–69.
- [46] J.D. Burns, K.G. Myhre, N.J. Sims, D.W. Stracener, R.A. Boll, Effects of annealing temperature on morphology and thickness of samarium electrodeposited thin films, *Nucl. Instrum. Methods Phys. Res. Sect. A* 830 (2016) 95–101.
- [47] K.G. Myhre, J.D. Burns, N.J. Sims, D.W. Stracener, R.A. Boll, Effects of annealing on fission fragment release from electrodeposited cf-252 thin-films, *Nucl. Instrum. Methods Phys. Res. Sect. A* 955 (2020) 163282.
- [48] A. Vascon, S. Santi, A. Isse, A. Kühnle, T. Reich, J. Drebert, K. Eberhardt, C.E. Düllmann, Smooth crack-free targets for nuclear applications produced by molecular plating, *Nucl. Instrum. Methods Phys. Res. Sect. A* 714 (2013) 163–175.
- [49] J. Lodermeier, M. Multerer, M. Zistler, S. Jordan, H.J. Gores, W. Kipferl, E. Diaconu, M. Sperl, G. Bayreuther, Electroplating of dysprosium, electrochemical investigations, and study of magnetic properties, *J. Electrochem. Soc.* 153 (4) (2006) C242.
- [50] L. Benedik, G. Sibbens, A. Moens, R. Eykens, M. Nečemer, S. Škapin, P. Kump, Preparation of thick uranium layers on aluminium and stainless steel backings, *Appl. Radiat. Isot.* 87 (2014) 238–241.
- [51] L. Sanchez-Cupido, J.M. Pringle, A.L. Siritwardana, A. Unzurrunzaga, M. Hilder, M. Forsyth, C. Pozo-Gonzalo, Water-facilitated electrodeposition of neodymium in a phosphonium-based ionic liquid, *J. Phys. Chem. Lett.* 10 (2) (2019) 289–294.
- [52] J. Choi, Y.H. Chung, Preparation of lanthanum oxide and lanthanum oxycarbonate layers on titanium by electrodeposition with organic solution, *J. Nanomater.* 2016 (2016) 28.
- [53] K. Myhre, J. Burns, H. Meyer, N. Sims, R. Boll, Samarium electrodeposited acetate and oxide thin films on stainless steel substrate characterized by XPS, *Surf. Sci. Spectra* 23 (1) (2016) 70–81.
- [54] L. Spiridigiozzi, M. Bortolotti, G. Accardo, A. Vergara, D. Frattini, C. Ferone, R. Cioffi, G. Dell'Agli, An in-depth multi-technique characterization of rare earth carbonates- $\text{RE}_2(\text{CO}_3)_3 \cdot 2 \text{H}_2\text{O}$ —owning tenerite-type structure, *J. Rare Earths* 40 (8) (2022) 1281–1290.
- [55] F.A. Andersen, L. Brecevic, et al., Infrared spectra of amorphous and crystalline calcium carbonate, *Acta Chem. Scand.* 45 (10) (1991) 1018–1024.
- [56] U. Wehrmeister, A.L. Soldati, D. Jacob, T. Häger, W. Hofmeister, Raman spectroscopy of synthetic, geological and biological vaterite: A Raman spectroscopic study, *J. Raman Spectrosc.* 41 (2) (2010) 193–201.
- [57] M. Hämmer, H.A. Höpfe, Crystalline orthorhombic Ln $[\text{CO}_3][\text{OH}]$ (Ln=La, Pr, Nd, Sm, Eu, Gd) compounds hydrothermally synthesised with CO_2 from air as carbonate source, *Z. Naturforsch. B: Chem. Sci.* 74 (1) (2019) 59–70.
- [58] V. Kartha, S. Venkateswaran, Vibrational spectra and normal vibrations of rare earth formates, *Spectrochim. Acta A* 37 (11) (1981) 927–934.
- [59] M. Moura, A. Ayala, J. Mendes Filho, I. Guedes, C. Paschoal, A. Leyva, G. Polla, D. Vega, P. De Perazzo, H. Lanza, Thermal behavior in $\text{Pr}(\text{HCOO})_3$ crystals, *J. Raman Spectrosc.* 35 (2) (2004) 159–164.
- [60] E. Silva, M. Moura, A. Ayala, I. Guedes, G. Polla, D. Vega, D. Tobia, M. Saleta, Vibrational modes of rare-earth formates, *J. Raman Spectrosc.* 40 (8) (2009) 954–957.
- [61] G. Herzberg, Molecular Spectra and Molecular Structure, D. van Nostrand, 1945.
- [62] L. Song, M. Rong-jun, IR of hydrated rare Earth carbonates, *Sci. Technol. Eng.* 7 (7) (2007) 36.
- [63] L. Jin, Préparation de Cibles D'Uranium: compréhension Du Procédé D'Électroprécipitation Pour Optimiser Les Conditions Opératoires (Ph.D. thesis), Université Paris-Saclay, 2021.
- [64] S. Sadi, A. Paulenova, P. Watson, W. Loveland, Growth and surface morphology of uranium films during molecular plating, *Nucl. Instrum. Methods Phys. Res. Sect. A* 655 (1) (2011) 80–84.

- [65] G. Sibbens, M. Ernstberger, T. Gouder, M. Marouli, A. Moens, A. Seibert, D. Vanleeuw, M.V. Zúñiga, T. Wiss, M. Zampella, et al., Morphological and compositional study of ^{238}U thin film targets for nuclear experiments, in: AIP Conference Proceedings, Vol. 1962, AIP Publishing LLC, 2018, 030007.
- [66] A. Ölcer, J. Drebert, T. Reich, XPS-Oberflächenanalyse von elektrochemisch hergestellten Urantargets, Tech. rep., Institut für Kernchemie, Johannes Gutenberg-Universität Mainz (Germany), 2007.
- [67] T. Smirnova, V. Volodin, M. Lebedev, V. Belyi, Raman scattering spectroscopy of inclusions of carbon in Al_2O_3 films and its solid solutions with hfo_2 , Opt. Spectrosc. 110 (1) (2011) 55–59.
- [68] A.C. Ferrari, J. Robertson, Interpretation of Raman spectra of disordered and amorphous carbon, Phys. Rev. B: Condens. Matter 61 (20) (2000) 14095.
- [69] S. Belaya, V. Bakovets, A. Boronin, S. Koschchev, M. Lobzareva, I. Korolkov, P. Stabnikov, Terbium oxide films grown by chemical vapor deposition from terbium (III) dipivaloylmethanate, Inorg. Mater. 50 (4) (2014) 379–386.
- [70] J. Hodkiewicz, Characterizing graphene with Raman spectroscopy, Thermo Fish. Sci. (2010) 51946.
- [71] J.-C. Grivel, Thermal decomposition of $\text{Ln}(\text{C}_2\text{H}_3\text{CO}_2)_3 \cdot \text{H}_2\text{O}$ ($\text{Ln}=\text{Ho}$, Er , Tm and Yb), J. Therm. Anal. Calorim. 109 (1) (2012) 81–88.
- [72] P.E. Larson, M.A. Kelly, Surface charge neutralization of insulating samples in X-ray photoemission spectroscopy, J. Vac. Sci. Technol. A 16 (6) (1998) 3483–3489.
- [73] J. Cazaux, Mechanisms of charging in electron spectroscopy, J. Electron. Spectrosc. Relat. Phenom. 105 (2–3) (1999) 155–185.
- [74] G. Greczynski, L. Hultman, The same chemical state of carbon gives rise to two peaks in X-ray photoelectron spectroscopy, Sci. Rep. 11 (1) (2021) 1–5.
- [75] B.V. Crist, XPS database entry for Tm_2O_3 , 2022, <https://xpsdatabase.com/thulium-spectra-tm2o3-thulium-oxide/>. (Accessed 10 September 2024).
- [76] R. Bolotovskiy, A. Bulkin, G. Krutov, V. Kudryashev, V. Trunov, V. Ul'yanov, O. Antonov, P. Hiismäki, H. Pöyry, A. Tiitta, et al., Neutron diffraction study of the crystal structure of rare-earth and yttrium anhydrous deuterated formates, Solid State Commun. 76 (8) (1990) 1045–1049.
- [77] D. Zagorac, H. Müller, S. Ruehl, J. Zagorac, S. Rehme, Recent developments in the inorganic crystal structure database: Theoretical crystal structure data and related features, J. Appl. Crystallogr. 52 (5) (2019) 918–925.
- [78] B. Lommel, W. Brüchele, K. Eberhardt, W. Hartmann, A. Hübner, B. Kindler, J.V. Kratz, D. Liebe, M. Schädel, J. Steiner, Backings and targets for chemical and nuclear studies of transactinides with TASCAs, Nucl. Instrum. Methods Phys. Res. Sect. A 590 (1–3) (2008) 141–144.
- [79] S. Sadi, A. Paulenova, W. Loveland, P. Watson, J. Greene, S. Zhu, G. Zinkann, Surface morphology and phase stability of titanium foils irradiated with ^{136}Xe , Nucl. Instrum. Methods Phys. Res. Sect. B 328 (2014) 78–83.
- [80] K.G. Myhre, J.C. Delashmitt, N.J. Sims, S.M. Van Cleve, R.A. Boll, Samarium thin films molecular plated from N, N-dimethylformamide characterized by XPS, Surf. Sci. Spectra 25 (2) (2018) 024003.
- [81] T. Kutty, I. Mohamed, J. Tareen, Hydrothermal phase equilibria in Ln_2O_3 - H_2O - CO_2 systems for Tm, Yb and Lu, Mater. Chem. Phys. 10 (5) (1984) 425–441.
- [82] S. Bernal, G. Blanco, J. Gatica, J. Pérez-Omil, J. Pintado, H. Vidal, Chemical reactivity of binary rare earth oxides, in: Binary Rare Earth Oxides, Springer Netherlands, Dordrecht, 2004, pp. 9–55.
- [83] A. Orera, G. Larraz, M. Sanjuán, Spectroscopic study of the competition between dehydration and carbonation effects in La_2O_3 -based materials, J. Eur. Ceram. Soc. 33 (11) (2013) 2103–2110.
- [84] P.G. Hansen, The conditions for electrodeposition of insoluble hydroxides at a cathode surface: A theoretical investigation, J. Inorg. Nucl. Chem. 12 (1–2) (1959) 30–37.
- [85] M. Ramaniah, R. Singh, S. Awasthi, S. Prakash, Studies on electrodeposition of actinide elements from non-aqueous medium, Int. J. Radiat. Appl. Instrum. Part A 26 (11) (1975) 648–650.
- [86] M. Crespo, A review of electrodeposition methods for the preparation of alpha-radiation sources, Appl. Radiat. Isot. 70 (1) (2012) 210–215.
- [87] Y. He, L. Han, C. Wang, Q. Chen, M.M. Sartin, G. Li, R. Hu, J. Tu, X. Xie, Y. Yang, et al., Molecular plating of actinide compounds on wafer-scale aluminum substrate, J. Alloys Compd. 878 (2021) 160393.
- [88] K. Izutsu, Electrochemistry in Nonaqueous Solutions, John Wiley & Sons, Weinheim, 2009.
- [89] G. Geffcken, Beiträge zur Kenntnis der Löslichkeitsbeeinflussung, Z. Phys. Chem. 49 (1) (1904) 257–302.
- [90] O. Ustinov, A. Schadrin, O. Shmidt, O. Shudegova, Study of carbon dioxide solubility in nitric acid and metal nitrates solutions for estimation of carbon-14 distribution between gas phase and solution during dissolution of spent nuclear fuel, 17. Radiochem. Conf. Marian. Lazne, Bookl. Abstr. 17 (98) (2014) 11. - 16. May.
- [91] Y.I. Hori, Electrochemical CO_2 reduction on metal electrodes, in: Modern Aspects of Electrochemistry, Springer, New York, 2008, pp. 89–189.
- [92] M. König, J. Vaes, E. Klemm, D. Pant, Solvents and supporting electrolytes in the electrocatalytic reduction of CO_2 , IScience 19 (2019) 135–160.
- [93] G.A. Hussein, G.A. Mekhemer, B.A. Balboul, Formation and surface characterization of thulium oxide catalysts, PCCP 2 (9) (2000) 2033–2038.
- [94] R. Sagaidak, Effects of beam wobbling and target rotation on the target temperature in experiments with intense heavy ion beams, Phys. Rev. Accel. Beams 24 (8) (2021) 083001.
- [95] C.L. Tracy, M. Lang, F. Zhang, C. Trautmann, R.C. Ewing, Phase transformations in Ln_2O_3 materials irradiated with swift heavy ions, Phys. Rev. B: Condens. Matter 92 (17) (2015) 174101.
- [96] C.L. Tracy, M. Lang, J.M. Pray, F. Zhang, D. Popov, C. Park, C. Trautmann, M. Bender, D. Severin, V.A. Skuratov, et al., Redox response of actinide materials to highly ionizing radiation, Nat. Commun. 6 (1) (2015) 1–9.
- [97] C. Stodel, M. Toulemonde, C. Fransen, B. Jacquot, E. Clément, G. Fremont, M. Michel, C. Dufour, Thermal spike model applied to thin targets irradiated with swift heavy ion beams at few MeV/u, in: EPJ Web of Conferences, Vol. 229, EDP Sciences, 2020, p. 05001.

Chapter **5**

Publication IV: Preparation of lanthanide thin films for ion beam experiments and post irradiation characterization

The following article was published as full article in *Nuclear Instruments and Methods in Physics Research Section A: Accelerators, Spectrometers, Detectors and Associated Equipment*, volume 1075 in 2025. It describes the application of a new electrochemical deposition method via triflate salts for ion beam experiments and their chemical characterization after ion beam irradiation.

5.1 Own contributions

The thin films were self prepared. The ion beam experiments were planned. The post irradiation analysis at other institutes were organized and the data were evaluated. At last, the paper was written completely self-directed.

5.2 Publication



Contents lists available at ScienceDirect

Nuclear Inst. and Methods in Physics Research, A

journal homepage: www.elsevier.com/locate/nima

Full Length Article

Preparation of lanthanide thin films for ion beam experiments and post irradiation characterization

E. Artes ^{a,b,c}, D. Ackermann ^d, Ch.E. Düllmann ^{a,b,c}, T. Häger ^e, B. Kindler ^c, T. Lefrou ^d, B. Lommel ^c, A.T. Loria Basto ^{a,b}, C.-C. Meyer ^{a,b}, C. Mokry ^{a,b}, F. Munnik ^f, J. Piot ^d, L.E. Reed ^a, D. Renisch ^{a,b}, H. Rothard ^g, J. Runke ^{a,c}, H. Savajols ^d, C. Stodel ^d, T. Madi ^g, V. Urbanova ^a, V. Watt-Morel ^d, A. Yakushev ^c

^a Department Chemie - Standort TRIGA, Johannes Gutenberg-Universität Mainz, Fritz-Strassmann-Weg 2, 55128 Mainz, Germany

^b Helmholtz-Institut Mainz, Staudingerweg 18, 55128 Mainz, Germany

^c GSI Helmholtzzentrum für Schwerionenforschung GmbH, Planckstraße 1, 64291 Darmstadt, Germany

^d GANIL, CEA/DRF-CNRS/IN2P3, Bd. Henri Becquerel, BP 55027, F-14076 Caen, France

^e Institut für Geowissenschaften, Johannes Gutenberg-Universität Mainz, Johann-Joachim-Becher-Weg 2, 55128 Mainz, Germany

^f Helmholtz-Zentrum Dresden-Rossendorf, Bautzner Landstraße 400, 01328 Dresden, Germany

^g CIMAP, CEA-CNRS-ENSICAEN-UNICAEN Bd. Henri Becquerel, Caen, France

ARTICLE INFO

Keywords:

Triflate
Electrochemical deposition
Thin film deposition
Irradiation
Ion beam
Vibrational spectroscopy
Ion beam analysis

ABSTRACT

The heaviest elements in the periodic table have a low production yield. In order to increase the production yield of the superheavy elements, thicker targets are required than the present molecular plating technique can offer. Therefore, lanthanide thin films, as lighter homologues to the actinides, were prepared by a new electrodeposition method. The trifluoromethanesulfonates (triflates) of the lanthanide salts were dissolved in Dimethylformamide (DMF) and then electrochemically deposited onto substrates of different geometries. These thin films were irradiated with different swift heavy ion beams with energies of over 200 MeV. Thin films were analyzed spectroscopically by Raman and IR measurements before and after irradiation, to investigate chemical changes induced by irradiation.

1. Introduction

The heaviest elements in the periodic table, superheavy elements (SHE), are produced by nuclear fusion reactions induced by intense heavy-ion beams with energies around the Coulomb barrier [1,2]. In this process, a target, often a thin film of an actinide, is irradiated with ⁴⁸Ca [1]. The SHE production rate depends on the cross section of the nuclear reaction of the ion beam projectile and the target atom of the target layer. Additionally, the production rate also depends on the beam intensity and the target thickness and is small for the SHE. To increase the production rate, the intensity of the ion beam or the layer thickness of the target has to be increased. The cross section function limits the maximum layer thickness to roughly $1500 \frac{\mu\text{g}}{\text{cm}^2}$ [3]. Layer thicknesses above $1500 \frac{\mu\text{g}}{\text{cm}^2}$ would barely increase the production yield of SHE.

Nowadays, the standard method for the production of actinide films is molecular plating, which is an electrochemical deposition method [4–6]. However, the film thickness that can be reliably achieved with this method is limited to about $1000 \frac{\mu\text{g}}{\text{cm}^2}$ on the thin substrates [4,7].

Recently, however, a method using salts of the trifluoromethanesulfonic acid (triflic acid), which is a super acid, and dimethylformamide (DMF) in electrochemical deposition was reported. By dissolving the lanthanide oxides in triflic acid and dissolving the newly formed trifluoromethanesulfonate (triflate) salt in an aprotic organic solvent like DMF, layer thicknesses of up to $2000 \frac{\mu\text{g}}{\text{cm}^2}$ for lanthanides could be achieved. The first experiments with these lanthanide targets have already been proven to be stable in a ⁴⁸Ca ion beam with $6 \frac{\text{MeV}}{\text{u}}$ and an accumulated fluence of $3.9 \times 10^{14} \frac{\text{ions}}{\text{cm}^2}$ [8].

The aim of this work is to understand how these thin films change chemically in the ion beam, by characterization via infrared (IR) and Raman spectroscopy both before and after irradiation. Additionally, Rutherford backscattering (RBS) combined with proton-induced X-ray emission spectroscopy (PIXE) was used to analyze the elemental composition of the thin layers.

* Corresponding author at: Department Chemie - Standort TRIGA, Johannes Gutenberg-Universität Mainz, Fritz-Strassmann-Weg 2, 55128 Mainz, Germany.
E-mail address: erartes@uni-mainz.de (E. Artes).

<https://doi.org/10.1016/j.nima.2025.170403>

Received 12 December 2024; Received in revised form 3 March 2025; Accepted 3 March 2025

0168-9002/© 2025 The Authors. Published by Elsevier B.V. This is an open access article under the CC BY license (<http://creativecommons.org/licenses/by/4.0/>).

2. Experimental methods

2.1. Target production

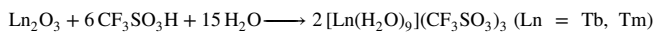
Commercially available trifluoromethanesulfonate (triflate) and self-produced triflates of terbium and thulium were used for the production of thin films.

The salts were dissolved in organic solvents and then deposited potentiostatically on titanium foils with different thicknesses.

Multiple targets were produced for different experiments, including ion beam irradiation conducted at the Grand Accélérateur National d'Ions Lourds (GANIL), France, and Transactinide Separator and Chemistry Apparatus (TASCA) at GSI Helmholtzzentrum für Schwerionenforschung, Germany, as well as for the Helmholtzzentrum Dresden Rossendorf (HZDR), Germany, where the Rutherford Backscattering and Proton Induced X-ray Emission (RBS/PIXE) measurements of the thin films were carried out.

2.1.1. Preparation of lanthanide stock solution

Lanthanide triflates were prepared as described in [8,9]. 15–50 mg lanthanide oxide were heated with a small stoichiometric excess of triflic acid and water was then evaporated to dryness. This way, the lanthanide triflate salts $[\text{Ln}(\text{H}_2\text{O})_9][\text{CF}_3\text{SO}_3]_3$ (Ln = Tb, Tm) were obtained.



In parallel, commercial anhydrous triflate salts $\text{Ln}(\text{TfO})_3$ (Ln = Tb, Tm), [Merck GmbH] were used.

The salts were dissolved in DMF to obtain a stock solution with varying concentrations between 500–1000 $\frac{\mu\text{g}}{\text{mL}}$.

2.1.2. Preparation of terbium targets for GANIL

An aliquot of the stock solution with the desired amount of terbium was diluted in DMF. The goal was to produce targets with a layer thickness of 1500–2000 $\frac{\mu\text{g}}{\text{cm}^2}$. For the production of the thin films two different electrochemical cells were used.

The cylindrical chimney cell (Fig. 1a) is constructed from a titanium block, with the substrate connected as the cathode. The cell wall, made of polyether ether ketone (PEEK), features a circular opening with a diameter of 10 mm, resulting in a deposition area of 0.785 cm². An ethylene propylene diene monomer (EPDM) gasket was used. The volume of the cell holds 10 mL. A palladium anode was used in these experiments. With the aim of quantitatively depositing 2000 $\frac{\mu\text{g}}{\text{cm}^2}$, 1570 μg of terbium were used.

The prepared solution was then deposited galvanostatically at a constant current and current density of $\approx 2.5 \frac{\text{mA}}{\text{cm}^2}$ for 2 h. Titanium foils with thicknesses of 2.1–2.3 μm and 10 μm were used as substrates for the deposition.

2.1.3. Preparation of thulium targets for TASCA

Since the triflate method uses DMF and DMSO as solvents, which are less viscous than the isobutanol/isopropanol mixture used in the molecular plating technique, the existing cell [10] used to produce the TASCA targets [11] was not leak-tight. The cell was slightly modified for this reason. The newly modified cell (Fig. 1b and c) consists of one block of PEEK, one wall with a 6 cm² banana-shaped opening that extends outwards along the edge to hold a gasket of the same shape, made of EPDM. At this position, the target substrate, which was glued to the TASCA frame with a silver epoxy glue, was mounted to the wall and fixed with a stainless steel back plate with five screws. This back plate also acted as a cathode. The anode was placed across the target in the cell with a crocodile clip. As the surface area of the cathode is relatively large, a rectangular graphite anode measuring 40 × 30 mm was used in these experiments. This consists of fewer parts than the standard version [7], therefore it is resistant to leakage.

The “TASCA cell” has a volume of 35 mL and the deposition area is banana-shaped with a deposition area of 6 cm² so that four segments form one target wheel with a diameter of 10 cm. This wheel was rotated in TASCA, to distribute the energy deposition of ion beam on a higher surface to prevent the destruction of targets [7].

With the aim of quantitatively depositing 2000 $\frac{\mu\text{g}}{\text{cm}^2}$ thickness layer, 1200 μg of thulium were used. Due to the different volumes and concentrations, which were chosen due to the deposition area and size of the anode compared to the chimney cell, the parameters had to be adjusted for the best deposition result. The adjusted solution was then galvanostatically deposited at a current density of approximately 3 $\frac{\text{mA}}{\text{cm}^2}$, for 5 h. From this solution, several depositions were made, each on a 2.1 μm thick titanium foil.

2.1.4. Preparation of thulium targets for measurements at HZDR

Commercial thulium triflate was deposited on 25 μm thick titanium foil. The chimney setup was used with an opening diameter of 6 mm, which results in a deposition area of 0.28 cm². A glassy carbon anode with 1 mm diameter and 5 cm length was used. With the aim of quantitatively depositing 2000 $\frac{\mu\text{g}}{\text{cm}^2}$, 560 μg of thulium were used.

Unlike the targets for GANIL and TASCA, the samples were prepared in argon atmosphere using dry solvents. The O₂ concentration in the box varied between 1 and 3 ppm, the H₂O concentration in the atmosphere was below 1 ppm. CO₂ concentration could not be measured.

The samples were then analyzed at the HZDR using Elastic Recoil Detection Analysis (ERDA), PIXE and RBS.

2.1.5. Tracer production of terbium and thulium

The electrochemical deposition yields were determined by the production of terbium and thulium tracers with neutron capture reactions. For this purpose terbium oxide and thulium oxide were irradiated in the TRIGA Mainz research reactor at a neutron flux of $7 \times 10^{11} \frac{\text{n}}{\text{cm}^2 \cdot \text{s}}$ for 1 h, producing ¹⁶⁰Tb and ¹⁷⁰Tm. These oxides were transformed to the triflate salts and deposition experiments were done, as described in 2.1.1 and 2.3.1, respectively.

2.2. Target irradiation

The manufactured targets were irradiated at GSI using the TASCA setup with ion beam provided by the UNiversal Linear ACcelerator (UNILAC) and at GANIL's D1-SME beamline using cyclotron beams. Different ion beams and energies were used in the respective facilities (Table 1).

2.2.1. Irradiation experiments at GSI TASCA

Self made thulium triflate thin films for TASCA irradiation were prepared on 2.1 μm titanium foils provided by the GSI target laboratory. One thin film was prepared with DMSO, while the others were prepared with DMF. Four targets were mounted on a wheel (Fig. 2) with a total target area of 24 cm².

This wheel was mounted in TASCA and the targets were irradiated with ⁴⁸Ca with an energy of 4.8 $\frac{\text{MeV}}{\text{u}}$ and a particle flux of 2.7×10^{12} pps for 40 min. The beam is collimated to 9 mm diameter just in front of the targets. The typical flux distribution is Gaussian with a FWHM of 8 mm. The ion beam passed through the titanium foil before hitting the thulium thin films, to keep the same layer sequence as in the production of superheavy elements. During irradiation, the targets were constantly rotated at 37.5 Hz [11] for even distribution of the ion beam on all the targets. This resulted in a fluence of $2.7 \times 10^{14} \frac{\text{ions}}{\text{cm}^2}$ for all targets.

2.2.2. Irradiation experiments at GANIL

Self-made terbium triflate was used to produce thin films on 2.1 μm thick titanium foils, which were provided by the GSI target laboratory. The thin films were produced in circular shape as previously described and glued afterwards on frames, provided by GANIL (Fig. 3). The wheel

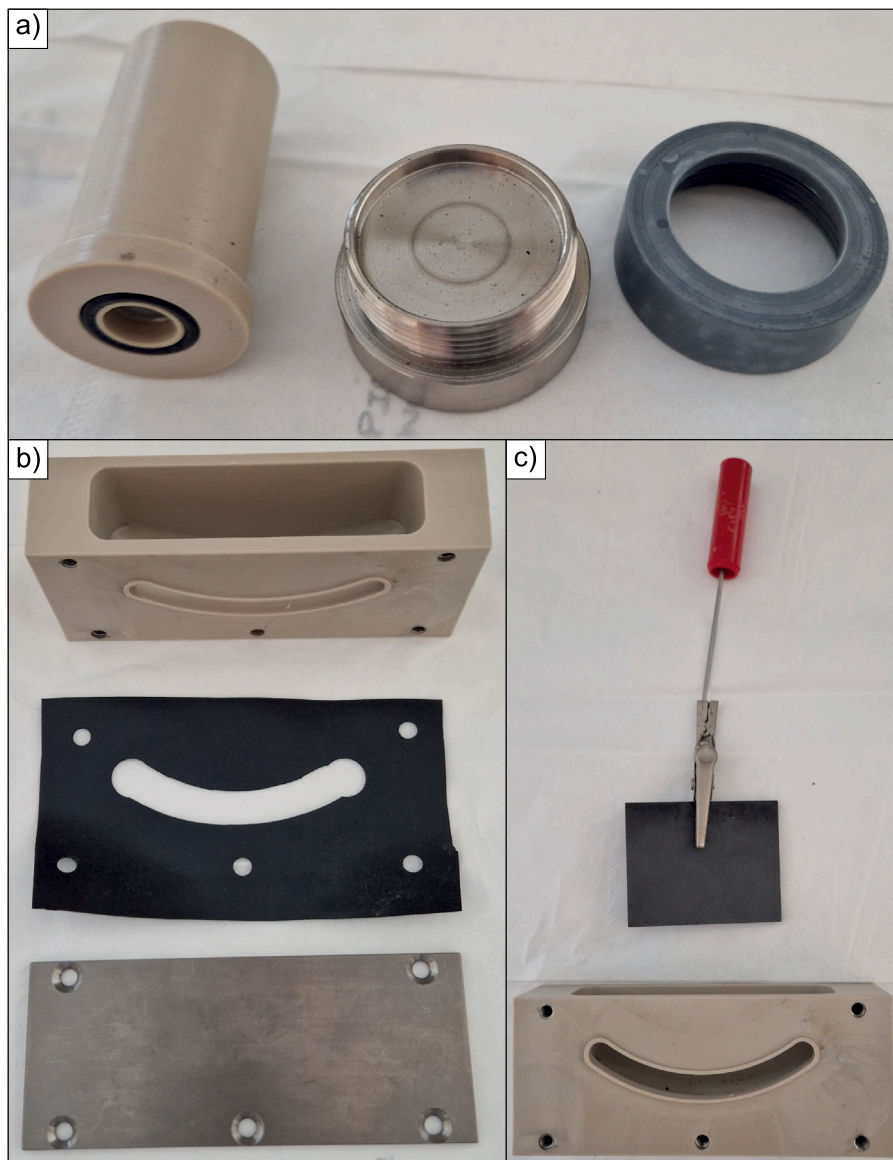


Fig. 1. The cells used for the preparation of targets. (a) The chimney cell used to prepare targets for GANIL and HZDR. It is also made out of PEEK. Next to it are the titanium base and a fixing nut made out of polypropylene. (b) The dismantled cell for TASCA targets. The cell used to prepare targets for TASCA is made out of PEEK. The sealing mat is made out of EPDM and the back is made out of stainless steel. (c) The TASCA cell with the used graphite anode.

Table 1

Overview of the different target irradiations. Three similar targets were irradiated at GANIL with an ^{70}Zn ion beam with an projectile energy of $9.3 \frac{\text{MeV}}{\text{u}}$. Each target received a different fluence. Four similar targets were irradiated at TASCA at GSI with an ^{48}Ca ion beam. The beam had an energy of $4.9 \frac{\text{MeV}}{\text{u}}$ and all targets received the same fluence. At HZDR three targets were irradiated with a ^{35}Cl beam. The energy was $1.2 \frac{\text{MeV}}{\text{u}}$. The aim was ERDA measurements with the Cl beam so no effort was made to keep the fluence identical.

Facility	Element	Target names	Target form	Beam	Projectile energy [$\frac{\text{MeV}}{\text{u}}$]	Fluence [$10^{13} \frac{\text{ions}}{\text{cm}^2}$]
GANIL	Terbium	GANIL-Tb-1	Circular 10 mm	^{70}Zn	9.3	1.0(1)
		GANIL-Tb-2				9.5(9)
		GANIL-Tb-3				100(10)
GSI	Thulium	GSI-Tm-1	Banana shaped	^{48}Ca	4.9	27(2)
		GSI-Tm-2				
		GSI-Tm-3				
		GSI-Tm-4				
HZDR	Thulium	HZDR-1	Circular 6 mm	^{35}Cl	1.2	4.7(5)
		HZDR-2				3.7(4)
-	Terbium	Control 1	Circular 6 mm	-	-	-

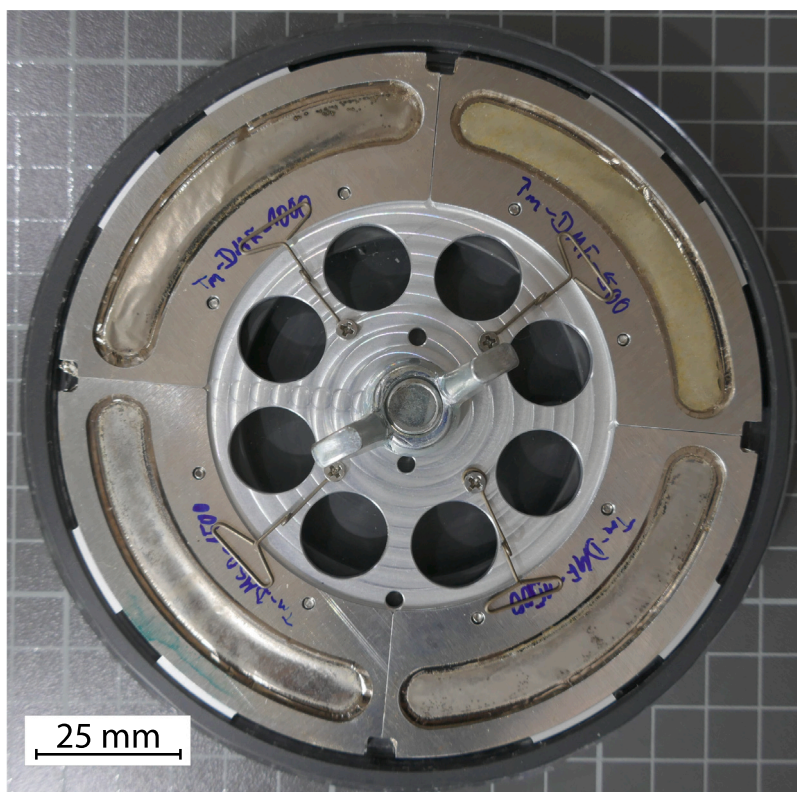


Fig. 2. The TASCA setup is made out of four targets arranged on a wheel with a diameter of 10 cm [11]. Each segment has an area of 6 cm². The wheel shown was mounted in TASCA and irradiated with an ⁴⁸Ca ion beam.

consists of three aluminum segments. Each segment supports up to four targets [12]. At GANIL the targets were irradiated with a ⁷⁰Zn ion beam an energy of 9.3 $\frac{\text{MeV}}{u}$ and a varying particle flux of $0.5\text{--}1.5 \times 10^{10}$ pps. The ion beam passed through the titanium foil before hitting the terbium thin films. The wheel was not rotated during the irradiation and each target was exposed to the beam for a defined period. A magnetic sweeping device is used to assure uniform irradiation on a rectangular irradiation field (defined by 4 movable slits) of up to 5 cm \times 5 cm. The diameter of the ion beam was 6 \times 7.5 mm² before sweeping. The ratio of the sweeping frequencies (horizontal frequency: ≈ 400 Hz; vertical frequency: ≈ 40 Hz) is chosen so, that no regular spatial structures such as Lissajous figures can occur. The projectile ion flux on the target is monitored during the irradiation by a secondary electron emission detector (stack of thin foils) allowing to measure the secondary electron current induced by the projectile. Prior to the target irradiation, a Faraday cup is inserted and the ratio of the secondary electron current and the projectile current is measured. This procedure allows a precise measurement of the projectile ion flux and the accumulated projectile fluence with an accuracy of $\approx 5\%$ [13]. The fluences deposited on the individual targets varied between 1×10^{13} and 1×10^{15} $\frac{\text{ions}}{\text{cm}^2}$. The fluence of the individual target is also noted in Table 1.

2.3. Target analysis

To determine the efficiency of the deposition, tests with radioactive terbium were carried out beforehand. This will be described in Section 2.3.1.

The films were also examined under a scanning electron microscope to determine the morphological changes.

To chemically characterize the films, IR and Raman spectra of the irradiated TASCA and GANIL films, as well as the non-irradiated ones; were obtained at the Institute of Geosciences institute of the Johannes Gutenberg University in Mainz.

2.3.1. Yields

The yield is the amount of lanthanide deposited on the surface, compared to the amount in the solution. A yield of 100% is achieved, if no lanthanide remains in the solution after deposition.

To determine the deposition yield, ¹⁶⁰Tb and ¹⁷⁰Tm tracers were produced by neutron activation at the TRIGA Mainz research reactor as described in Section 2.1.5.

An Aliquot of the supernatant solution was taken in order to make an indirect yield measurement via gamma spectroscopy. This was done before and after deposition. The gamma activity of the samples was measured in an HPGe detector from Ortec and the gamma spectra were evaluated with the Genie 2000 software from Canberra. The difference in the activities of the supernatant solution before and after deposition was determined by giving indirect information on the deposition yield, neglecting potential losses to sorption on the container walls. The experiment was replicated five times to assess reproducibility and facilitate error estimation. For the ion beam experiments, inactive targets were produced in the same way. Yields were assumed to be in the same order as in the tests with the radioactive isotopes.

2.3.2. Scanning electron microscopy (SEM)

To evaluate the quality of the films, the samples were examined by scanning electron microscopy (Philips XL30) using an accelerating voltage of 20 kV and detectors for secondary (SE) and back scattered electrons (BSE).

Pictures of the thin films were acquired after the irradiation. Fresh thin films were produced and compared to the irradiated ones, to see the impact of the ion beams on the morphology.

2.3.3. Infrared microscopy (IR)

The targets GANIL-Tb-2, DMF-1 and Control-1 were analyzed by infrared microscopy (Nicolet Continu μ m connected to a Nicolet 6700, THERMO SCIENTIFIC). A mercury cadmium telluride (short: MCT) detector was used. The increments were set to 0.1 nm and the acquisition

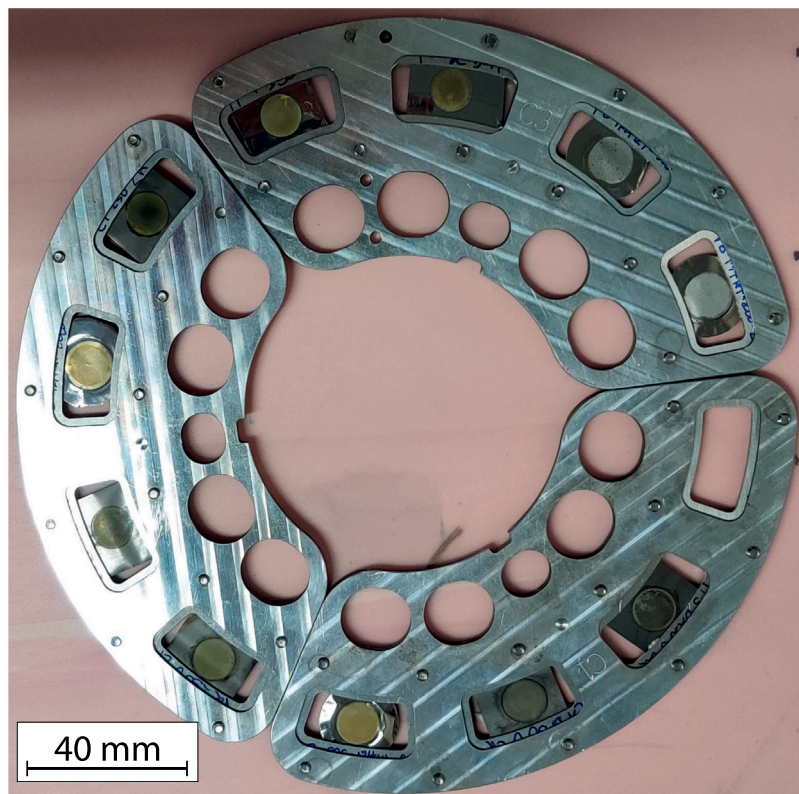


Fig. 3. Target wheel used for irradiation tests at GANIL. The wheel consists of three segments. Each segment supports up to four target. One position was left intentionally blank for the beam analysis.

time for each spectrum was set to 5 min. Infrared spectra from 500 cm^{-1} to 4000 cm^{-1} were collected in reflection on a gold mirror. IR spectra were recorded from three different locations from each thin film to exclude artifacts in the film. The reflection of IR radiation from the sample was measured.

2.3.4. Confocal Raman microscopy

The same targets, from Section 2.3.3 were also analyzed with a confocal Raman microscope (Horiba Jobin Yvon LabRAM HR 800 spectrometer). The microscope was equipped with a Si-based charge-coupled device (CCD) detector (Peltier-cooled), an integrated Olympus BX41 optical microscope and an automatized x-y stage. A 50x long-distance objective (numerical aperture 0.55), a frequency-doubled Nd:YAG laser with 532.21 nm emission wavelength, a grating with $1800\frac{\text{grooves}}{\text{mm}}$, and a slit width of $100\text{ }\mu\text{m}$ were used to acquire the data. The spectral resolution was 0.6 cm^{-1} . Raman spectra of the different thin films from 200 cm^{-1} to 3200 cm^{-1} were collected.

2.3.5. Elastic Recoil Detection Analysis (ERDA)

The samples HZDR-1, HZDR-2 and HZDR-3 were analyzed with Elastic Recoil Detection Analysis (ERDA) using a $43\text{ MeV }^{35}\text{Cl}^{7+}$ ion beam. The angle between the sample normal and the incoming beam was 75° , the scattering angle was 30° . The analyzed area was about $2 \times 2\text{ mm}^2$. The recoil atoms and scattered ions were detected with a Bragg Ionization Chamber (short BIC), which enables energy measurements and Z identification of the particles. H recoils were detected with a separate solid-state detector at a scattering angle of 40° . In front of this detector a $25\text{ }\mu\text{m}$ Kapton foil was mounted to stop scattered ions and heavy recoil ions. The depth resolution of this system is limited by the energy loss straggling in the foil. The ion-beam dose (in arbitrary units) was determined using a gold plated rotating (1 Hz) vane and a solid-state detector, which detected Cl backscattering from Au. Irradiation at the ERDA setup of the HZDR inflicted an ion dose per area of up to

$I = 1.6(2) \times 10^{14}\frac{\text{ions}}{\text{cm}^2}$ to the thin films. The aim was ERDA measurements with the Cl beam so no effort was made to keep the fluence for all targets identical. This induced changes in the sample surface visible to the naked eye. The changes in the thin films of the ERDA measurements could be characterized using μBeam , so irradiated and non-irradiated surfaces could be compared.

2.3.6. μBeam

The same samples analyzed by ERDA were also examined using Rutherford Backscattering Spectrometry (RBS) in combination with Particle Induced X-ray Emission (PIXE), employing a 3 MeV H^+ beam. The ion beam was focused to a spot size of $(7 \times 5)\text{ }\mu\text{m}^2$. Backscattered protons were detected at a scattering angle of 174° using a silicon strip detector, while a Ketek silicon drift detector with an $80\text{ }\mu\text{m}^2$ collimation was used to detect X-rays emitted from the sample. This detector was positioned outside the sample chamber, separated by a $1\text{ }\mu\text{m}$ silicon-nitride window, a 6 mm air layer, and a $25\text{ }\mu\text{m}$ Be window. Additionally, a $65\text{ }\mu\text{m}$ aluminum absorber was employed to minimize Ti-K X-ray contributions and block backscattered H^+ ions from entering the detector. RBS provided depth profiles for major elements, excluding hydrogen, which RBS cannot detect. For C, N, and O, evaluated cross-sections from SigmaCalc were applied [14]. For titanium, accurate data for the energy range and scattering angle of this study were unavailable, so a measurement on the Ti backing foil was used to obtain non-Rutherford cross-sections through the program ndf [15].

AFM measurements on the blank titanium foil revealed significant roughness with value of $\text{rms} = 39(8)\text{ nm}$. Consequently, the determined cross-section may not be universally applicable. The titanium foils used for the investigations at the HZDR correspond to the technical standard in target production, which includes their known surface roughness.

For the thulium thin films, initial large scans, with a size of $(260 \times 260)\text{ }\mu\text{m}^2$ or $(260 \times 205)\text{ }\mu\text{m}^2$, were performed, followed by point measurements with the size of the beam spot mentioned

Table 2
The desired deposition mass, yields and layer thicknesses of the described targets.

Target names	Desired layer thickness [$\mu\text{g}/\text{cm}^{-2}$]	Yield	Real layer thickness [$\mu\text{g}/\text{cm}^{-2}$]
GANIL-Tb-1	2000	78(5)%	1560(100)
GANIL-Tb-2		81(5)%	1620(100)
GANIL-Tb-3		82(5)%	1640(100)
GSI-Tm-1	2000	23(2)%	460(40)
GSI-Tm-2		26(2)%	520(40)
GSI-Tm-3		23(2)%	460(40)
GSI-Tm-4		25(2)%	500(40)
HZDR-1	2000	–	–
HZDR-2			
Control-1	2000	–	–

above in a homogeneously composed region. The μBeam analytics were performed on the irradiated samples with the ERDA procedure. The analysis area between the irradiated and non-irradiated regions of the sample surface was examined, allowing both areas to be analyzed within a single image to study the effects of ion radiation on the thin films.

3. Results

3.1. Yields

The yields were determined using tracer activation of terbium and subsequent gamma measurement of the supernatant solutions before and after deposition.

The aim was to produce thin films with an areal weight of 1500–2000 $\frac{\mu\text{g}}{\text{cm}^2}$.

The thin films of the TASCAs targets were produced with inactive thulium. Fig. 2 does not allow to infer details of the layer uniformity. There are a few smaller areas visible, where the layer is thinner (or even absent) compared to the average, but overall, uniformity is similar to that obtained in the classical MP method. After the deposition, the supernatant solution was activated, and after quantification, it was found that, that the residual concentration of thulium in this solution corresponds to a thin layer of a thickness of approximately 500 $\frac{\mu\text{g}}{\text{cm}^2}$. Further experiments with the TASCAs cell showed that thin films with $1600 \pm 100 \frac{\mu\text{g}}{\text{cm}^2}$ could also be produced with adjustments to higher current densities of 3 $\frac{\text{mA}}{\text{cm}^2}$ for 3 h in the deposition process, which corresponds to a yield of $(80 \pm 5)\%$.

For the circular targets, the parameters were optimized by adjusting the current density to 2.5 $\frac{\text{mA}}{\text{cm}^2}$ for 2 h and a constant yield of $(80 \pm 5)\%$ was also achieved. These settings were used to produce inactive targets for GANIL. The yields for all targets are listed in Table 2. The yields were not determined for HZDR-1, HZDR-2 and Control-1.

3.2. Irradiation results

All targets were able to mechanically withstand the conditions in the ion beams. The targets irradiated at TASCAs were radioactive afterwards, their final analytics were performed in non-radiation licensed laboratories after a waiting time of one year, at which time the activity had decayed sufficiently.

While the targets that were irradiated at TASCAs had completely decayed at the time of the analytical measurements, some targets that were irradiated in GANIL were still active. The highest fluence that one target experienced at GANIL was $1 \times 10^{15} \frac{\text{ions}}{\text{cm}^2}$. This target still had residual activity after irradiation, which is why no Raman and IR data could be collected from this target. Instead, targets with a fluence of $1 \times 10^{14} \frac{\text{ions}}{\text{cm}^2}$ were characterized. Table 3 is an overview, which shows the analytical methods used for the targets described in this work.

Table 3
Overview of the applied analytics on the specific target.

Target names	Lanthanide	Analytical method
GANIL-Tb-2	terbium	IR, Raman
GSI-Tm-1	thulium	IR, Raman
HZDR-1	thulium	μbeam
Control 1	terbium	IR, Raman

Table 4
Ion beam doses of different irradiations in Gray. ^{35}Cl was used at ERDA measurements at HZDR, ^{48}Ca was used at TASCAs and ^{70}Zn at GANIL for irradiation tests. dE/dx elec. stand for the energy loss due to electric interactions.

Isotope	^{35}Cl	^{48}Ca	^{70}Zn
Energy per nucleon [MeV/u]	1.2	4.90	9.28
dE/dx elec. [keV/nm]	7.8	8.9	12
Fluence [10^{14} ions/ cm^2]	2.0(2)	2.7(3)	1.0(1)
Energy dose [Gy]	$2.9(3) \times 10^8$	$4.5(5) \times 10^8$	$2.5(3) \times 10^8$

3.2.1. Normalization of irradiation effects of the different used beams

Different projectiles and energies were used to irradiate the targets. To be able to compare the irradiated targets to each other it is necessary to normalize the irradiation effect of the different ions beams. This can be done by calculating the energy dose deposition from the ion beams on the targets. The calculations were based on the stopping power of the ions through the thin films simulated by SRIM (version SRIM-2008.04). Necessary for the calculation is an assumption of the density and chemical composition of the target material, the energy of the projectile and fluence of the ion beam. It was assumed, that the target material had the density and chemical composition of the oxides Tm_2O_3 and Tb_4O_7 , since the ion beam has the highest energy deposition in the oxides and the actual composition and density are not well known. Furthermore, the energy loss of the ion beam due to the penetration of the titanium foil was taken into account in the calculation for the GSI-Tm-4 and GANIL-Tb-2 targets prior to the calculation of the dose for the target layer. For HZDR-1, however, this was not considered, as the ^{35}Cl beam directly struck the target layer without first penetrating the titanium layer.

The fluence and energy of the ion beam were known. The nuclear and electrical interaction of the projectile with the target material as well as the density were necessary for the calculation of the energy dose deposition. While the electrical interaction leads to an energy loss of the projectile in the target material of $\approx 8 - 12 \frac{\text{keV}}{\text{nm}}$, the nuclear interactions are in the order of $1.0 \times 10^{-2} \frac{\text{keV}}{\text{nm}}$ and have less than 1 % impact on the overall dose. The results are visible in Table 4.

3.2.2. Morphology

After irradiation, the targets were examined both with the naked eye and in the SEM. Photographs of the targets before and after their irradiation are shown in Fig. 4. The targets, which received a dose of 10^8 Gy show visible changes in their morphology. GSI-Tm-1 became darker, while HZDR-1 clearly shows a square spot, where the ion beam hit the thin film. GANIL-Tb-2 shows no significant change in the thin film.

SEM images are shown in Fig. 5. The image of the non-irradiated samples show the typical cracks from the electrodeposition procedure. These are similar to the “mudcracking” effect of the molecular plated thin films.

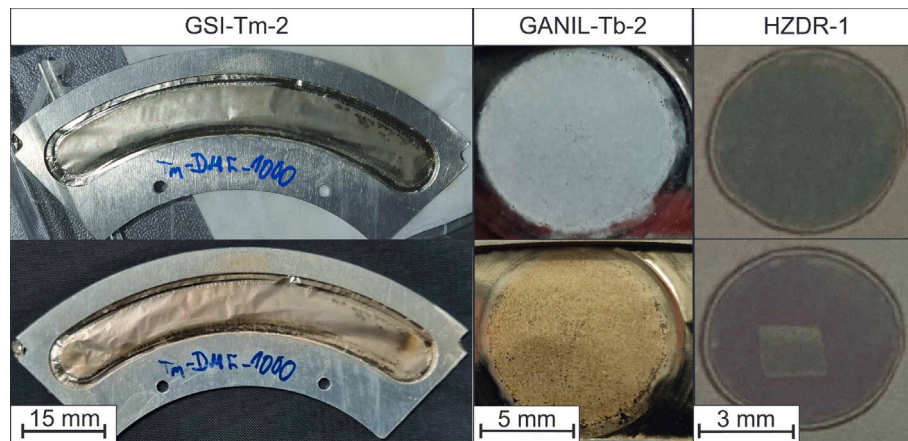


Fig. 4. The top row shows the targets before they were irradiated. The bottom row shows the same targets after irradiation. The detail to the irradiation can be found in Table 1. On the left GSI-Tm-2 before and after irradiation with 2.68×10^{14} ^{48}Ca $\frac{\text{ions}}{\text{cm}^2}$ at TASCA. This target is shown, since a part of GSI-Tm-1 was cut out on purpose for IR and Raman spectroscopy. In the middle GANIL-Tb-2, which was irradiated with 1×10^{14} ^{70}Zn $\frac{\text{ions}}{\text{cm}^2}$ at GANIL. On the right HZDR-1 which was irradiated with 2×10^{14} ^{35}Cl $\frac{\text{ions}}{\text{cm}^2}$ s.

The targets that were irradiated at TASCA show optical changes. There was a discoloration of the thin films to black. This is not observed with targets that were irradiated in GANIL. Optical changes were also observed after the irradiation with ^{35}Cl at the HZDR. The square irradiation spot is clearly visible on the target.

The thin films of the irradiated samples show the same structures in the SEM as the non-irradiated targets. Observable is the lack of notable alterations in the morphological composition of GANIL targets, manifesting at both macroscopic and microscopic scales. While TASCA targets exhibit discernible optical alterations, the corresponding changes in SEM imagery are relatively minor. Conversely, notable microstructural variations are evident in targets exposed to ^{35}Cl irradiation at HZDR, notably substantial tile shrinkage in SEM images within the irradiated zones.

3.3. Vibrational spectroscopy

The vibrational spectra of the different targets were measured at the Institute of Geoscience at JGU Mainz.

The Raman spectra of the non-irradiated and irradiated thin films are shown in Fig. 6. Oxides are visible at a Raman shift below 500 cm^{-1} [16]. These also remain visible after irradiation with a dose of $4.5(5) \times 10^8$ Gy of ^{48}Ca or $2.5(3) \times 10^8$ Gy of ^{70}Zn . Carbonate bands can be seen between 680 and 850 cm^{-1} , between 1050 and 1580 cm^{-1} , between 1310 and 1380 cm^{-1} , and between 1580 and 1610 cm^{-1} . These are still visible after irradiation [17,18], but decreased significantly. The bands at 2850 and 2960 cm^{-1} are consistent with the literature on formates and are therefore assigned to this functional group. Their intensity also decreases after irradiation and they become broader, so that only one band is visible after irradiation. The position and assignment of the bands are given in Table 5.

Fig. 7 displays the IR spectra of Control-1, GSI-Tm-1 and GANIL-Tb-2. In both cases, before and after irradiation terbium thin films exhibit a broad band around 3400 to 3550 cm^{-1} . This band is assigned to hydroxide. After the ^{48}Ca irradiation, this band disappears.

The bands within the 1300 to 1700 cm^{-1} range are identified as carbonates [18–20], including vibrations of formates observed in previous studies [21–24] on molecular plated thin films. Another carbonate band appears at 850 cm^{-1} [18–20]. With increasing irradiation intensity, these bands also decrease in intensity. At 2350 cm^{-1} a small band is visible which is a measurement artifact from the titanium background.

Table 5

Assignment of the chemical compounds to the vibrational bands in the IR (Fig. 7) and Raman spectra (Fig. 6) and their corresponding references.

Chemical species	Symbol	IR band [cm^{-1}]	Raman band [cm^{-1}]	Assignment references
Oxide	O	–	315 405–430	[16]
Carbonate	C	850 1300–1700	680–850 1050–1580 1310–1380 1580–1610	[17–20]
Formate	F	1300–1700	2850 2960	[21–24]
Residue water hydroxide	H	3400–3550	–	[25]

3.4. ERDA and μBeam

The fluence induced by ERDA almost corresponds to the fluence at the TASCA setup. Thin films made from commercial triflate under glovebox conditions of Section 2.1.4 changed their morphology (Fig. 8) under ERDA irradiation. Since for ERDA a clearly focused square beam spot has been used, which is visible even to the naked eye (Fig. 8a), the difference between analyzed (i.e., irradiated) and non-analyzed thin film was investigated using the μBeam setup. The PIXE image (Fig. 8b) shows the distribution of thulium in the thin film, the upper third shows the irradiated part, the lower two thirds the non-irradiated film. The image shows irradiation changes in the morphology. After irradiation, the thulium contained in the film is concentrated in smaller areas and substantial areas of the titanium backing are no longer covered with material. The SEM images (Fig. 8c) confirm these findings. The irradiation has caused the material to shrink.

The RBS (Fig. 9) allowed the elemental composition of the films as a function of layer depth to be determined. The non-irradiated films (Fig. 9a) are dominated by carbon and oxygen, thulium is rather a minor component of the deposits in atomic percentage. The RBS measurements are not sensitive enough to show low amounts of nitrogen or fluorine, however the ERDA measurements on the same samples did show some atomic percentage of nitrogen, from the solvent DMF, and low amounts of fluorine. No sulfur, present in the triflate, was detected, however, both RBS and ERDA, with these parameters are very sensitive to sulfur. The titanium signal scattered from measuring point to measuring point, indicating a heterogeneous distribution

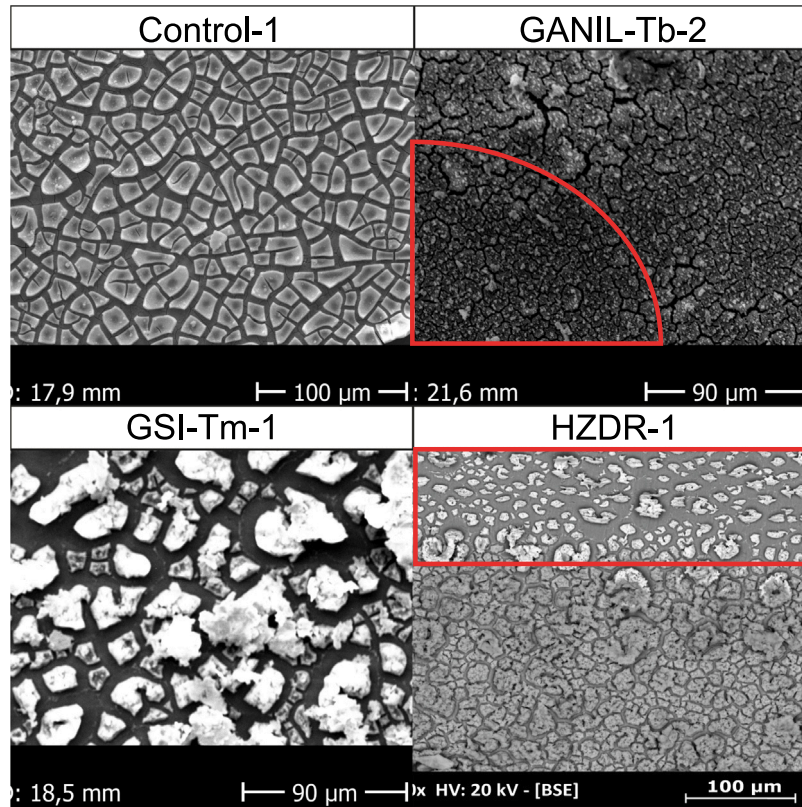


Fig. 5. SEM pictures of different targets are shown. Top left shows Control-1. Top right shows GANIL-Tb-2, which was irradiated at GANIL with 1×10^{14} ^{70}Zn $\frac{\text{ions}}{\text{cm}^2}$ and an energy dose of $2.5(3) \times 10^8$ Gy. The red outline shows the area that was hit by the ion beam. Bottom left shows GSI-Tm-1 with a fluence of 2.68×10^{14} ^{48}Ca $\frac{\text{ions}}{\text{cm}^2}$ and an energy dose of $4.5(5) \times 10^8$ Gy and bottom right shows HZDR-1 which was irradiated at HZDR with 2×10^{14} ^{35}Cl $\frac{\text{ions}}{\text{cm}^2}$ and an energy of $2.9(3) \times 10^8$ Gy. The red outline shows the area that was hit by the ion beam.

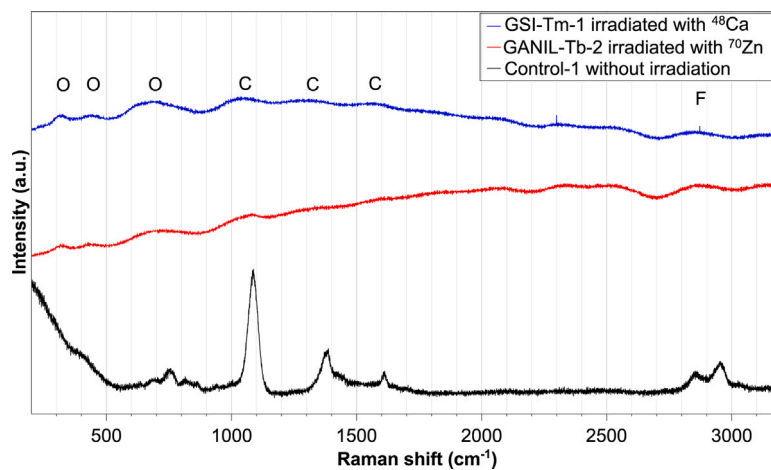


Fig. 6. The Raman spectra of the targets GSI-Tm-1, GANIL-Tb-2 and Control-1. The black spectrum shows a non-irradiated target. The red spectrum shows the vibrational bands after the irradiation with 1×10^{14} ^{70}Zn $\frac{\text{ions}}{\text{cm}^2}$ and the blue spectrum shows the vibrational bands after the irradiation with 2.7×10^{14} ^{48}Ca $\frac{\text{ions}}{\text{cm}^2}$. All spectra are normalized to their respective maximum value. Oxides (O), carbonates (C), and formates (F) could be identified in the spectra.

of the thulium film thickness, as also indicated by the PIXE image. With the exception of the titanium signal, the curves were otherwise reproducible for different measuring points.

Through irradiation (Fig. 9b), the carbon signal in the thin films decreases noticeably, while the relative oxygen and thulium content increases. In the layers near the surface of the deposition, the oxygen content is slightly increased compared to the non-irradiated sample area. It should be noted again that glassy carbon was chosen as the anode material in the preparation of these thin films.

The high carbon content could be due to the corrosion of the electrode material.

4. Discussion

4.1. Stability of thin films in ion beams

The thin films exhibited remarkable stability under diverse ion beams and doses, with negligible changes observed during irradiation with a fluence of 1×10^{14} ^{70}Zn $\frac{\text{ions}}{\text{cm}^2}$ and with a fluence of $2.68 \times$

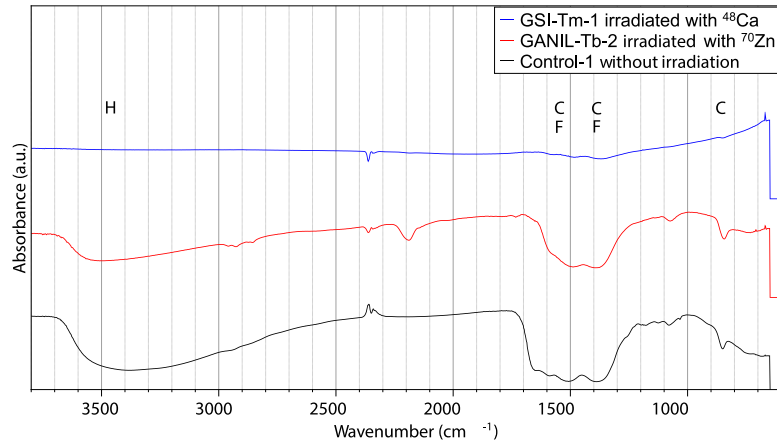


Fig. 7. The IR spectra of the targets GSI-Tm-1, GANIL-Tb-2 and Control-1. The black spectrum shows a non-irradiated target. The red spectrum shows the vibrational bands after the irradiation with $1 \times 10^{14} \frac{\text{ions}}{\text{cm}^2}$ ^{70}Zn ions and the blue spectrum shows the vibrational bands after the irradiation with $2.7 \times 10^{14} \frac{\text{ions}}{\text{cm}^2}$ ^{48}Ca ions. All spectra are normalized to their respective maximum value. Hydroxides (H), carbonates (C), and formates (F) could be identified in the spectra.

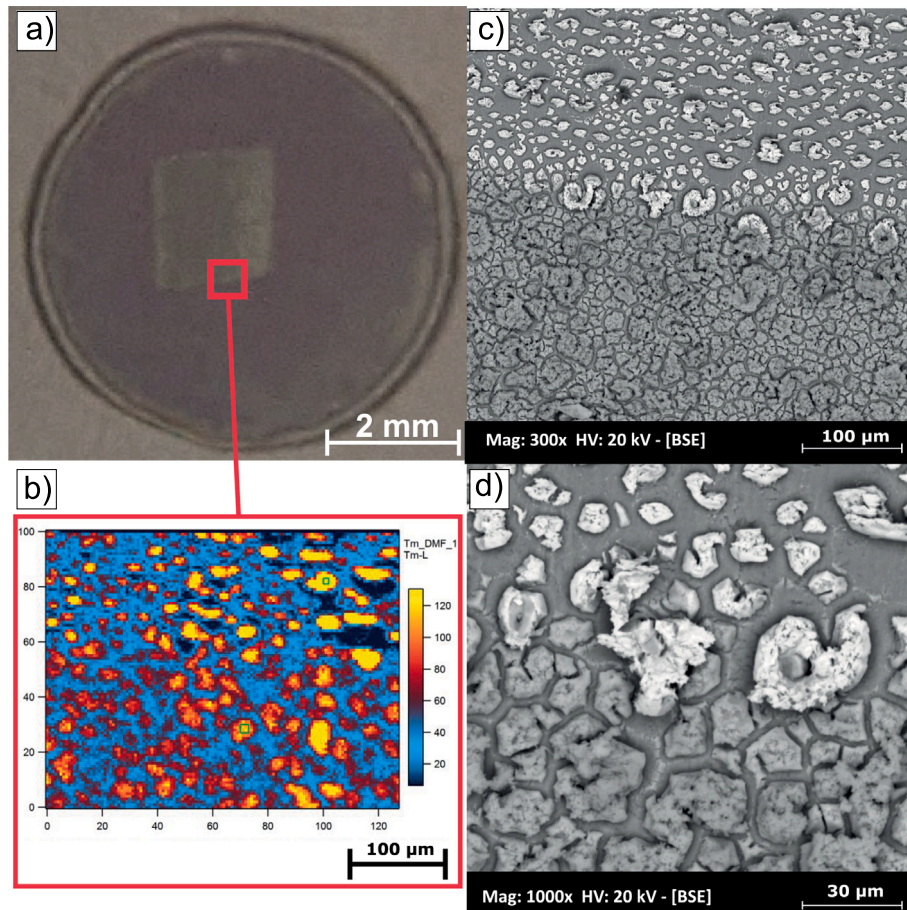


Fig. 8. Images of deposits from HZDR-1 with an estimated surface weight of $1800(200) \frac{\mu\text{g}}{\text{cm}^2}$ after irradiation at the HZDR. The estimation was done by pre-experiments with a radioactive tracer. (a) Photo of the sample after irradiation with $I = 2.0 \times 10^{14} \frac{\text{ions}}{\text{cm}^2}$ using a $4.9 \frac{\text{MeV}}{\text{u}} \text{ }^{35}\text{Cl}^{7+}$ ion beam, (b) PIXE image of the boundary between irradiated and non-irradiated thin film, (c) and (d) SEM images of the same region with 300x and 1000x magnification.

$10^{14} \frac{\text{ions}}{\text{cm}^2}$ ^{48}Ca . SEM images revealed only minor morphological changes, suggesting robust stability of the thin films.

The dose applied to all targets are in the same order of magnitude, varying only in a factor of 2–3. This makes every target well comparable to each other.

The ^{48}Ca beam at GSI and the ^{70}Zn beam at GANIL traversed the titanium backing of target sets before hitting the target layer. In

contrast, the ^{35}Cl beam was directed at targets HZDR-1, 2, and 3 without passing through the titanium backing. This difference may influence the irradiation damage done to the target thin films. It is noteworthy that variations in post-irradiation behavior of electrodeposited targets, including tile shrinkage [26] or thin film melting [27], have been observed, underscoring the incomplete understanding of these phenomena.

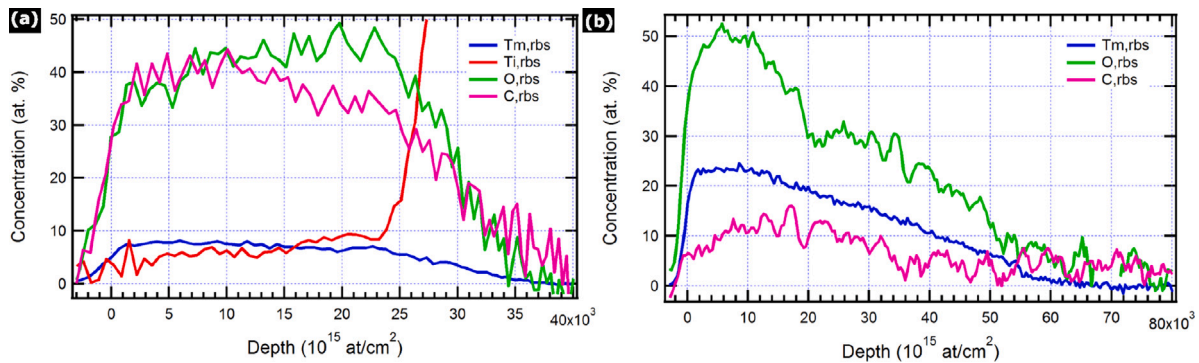


Fig. 9. RBS depth profile of the thin films produced from HZDR-1 under argon atmosphere with an estimated surface weight of $1800(200) \frac{\mu\text{g}}{\text{cm}^2}$. The estimation was done by pre-experiments with a radioactive tracer as explained in chapter 2.1.5. (a) before irradiation; (b) after irradiation with $I = 2.0 \times 10^{14} \frac{\text{ions}}{\text{cm}^2}$ ^{35}Cl .

Comparative analysis, particularly with irradiated MP targets [26, 27], suggests that targets produced via the triflate method hold promise to be at least as stable as those produced via the MP method, even though the fluences are 3 order of magnitude lower compared to typical SHE experiments which have a fluence in the order of magnitude of $1 \times 10^{17} \frac{\text{ions}}{\text{cm}^2}$ [28]

4.2. Spectroscopic changes of the thin films

The ERDA measurements did not produce useful results as the method-inherent irradiation with the ^{35}Cl beam led to changes in the layer morphology rather than in further information of the unaltered layer. The applied ion dose corresponded approximately to that of the TASCA experiment, so that the differences in irradiation could then be analyzed in an experiment using the μBeam setup.

PIXE and SEM (Fig. 8) clearly show that the individual tiles of the mudcracking of the thin films are strongly compressed by irradiation. After irradiation they cover significantly less titanium surface of the backing. PIXE and RBS spectra show that the relative amount of thulium in these compacted tiles had increased. RBS spectra (Fig. 9) show that mainly carbon and only little oxygen had been lost through irradiation. The irradiation had thus driven the carbon out of the films. However, it cannot be ruled out that the high carbon content of the non-irradiated thin films comes from corrosion of the anode (glassy carbon). Intercalated solvent (DMF) cannot be ruled out as a cause, since small amounts of nitrogen was observed in the ERDA data but not in the RBS data. Fluorine was visible in small amount in the ERDA measurements but sulfur was completely missing, so that co-deposition of the triflate can be excluded.

The IR and Raman measurements show that targets produced with this method also have organic residues, such as carbonates. Other chemical compounds like carboxylate [6] or formate [8] cannot be clearly detected, but cannot be ruled out either.

As with the MP targets, it can be observed that the carbon-containing species decrease with intensive ion irradiation and oxidic species remain.

Prior to irradiation, the precise chemical composition of the thin film remains unknown. However, as with MP targets, it is hypothesized that organic species, including carbonates, carboxylates and formates, are present in addition to oxide and hydroxide compounds. The irradiation process has been observed to reduce the carbon content, which suggests that the organic components are undergoing destruction and are likely to be escaping as CO_2 in the process. The RBS data from HZDR-1 demonstrate a general decline in carbon content, though it does not reach zero. Organic species, including carbonates and formates, also persist. Simultaneously, the relative oxide content in the RBS measurements for HZDR-1 increases following irradiation. The IR and Raman data of GSI-Tm-1 and GANIL-Tb-2 also demonstrate that the carbon species decrease, though they do not entirely disappear.

The Raman data additionally indicates that the oxidic bands remain present, suggesting a transformation of the layer into a purely oxidic film. With higher ion beam intensities, the carbon content is further reduced, indicating that the transformation into a pure oxidic film is not spontaneous but rather a process.

5. Conclusion

The results show that thin films with up to $1600 \pm 100 \frac{\mu\text{g}}{\text{cm}^2}$ could be produced consistently regardless of the shape and area of the deposition surface. The thin films have demonstrated promising initial results regarding their stability and suitability for use in ion beam experiments.

The targets showed gradual surface and chemical changes with different ion beams and doses. It can be observed that the fraction of carbon-containing species, which were present in the thin films after deposition, decreased after irradiation and the oxidic species became dominant. However, this change occurs relatively slowly. Carbon could still be observed in the film after the irradiation, indicating that this change depends on the energy and fluence of the ion beam. After irradiation with ^{70}Zn , there was an optical change in the GANIL-Tb-1 targets, but this was barely noticeable in SEM compared to the non-irradiated thin films. The structure of GANIL-Tb-1 did not change significantly after irradiation with a ^{70}Zn ion beam with a fluence of $1 \times 10^{14} \frac{\text{ions}}{\text{cm}^2}$ under the microscope.

From this it can be concluded that the described method is promising for the production of targets for the production of superheavy elements and that there are prospects that these thin films show stability in the ion beam similar to that of thin films produced using the MP technique.

CRediT authorship contribution statement

E. Artes: Writing – review & editing, Writing – original draft, Visualization, Validation, Project administration, Methodology, Investigation, Formal analysis, Data curation, Conceptualization. **D. Ackermann:** Resources, Investigation. **Ch.E. Düllmann:** Writing – review & editing, Supervision. **T. Häger:** Resources, Investigation. **B. Kindler:** Resources. **T. Lefrou:** Project administration, Investigation. **B. Lommel:** Resources. **A.T. Loria Basto:** Resources, Investigation. **C.-C. Meyer:** Project administration, Methodology, Investigation, Data curation, Conceptualization. **C. Mokry:** Writing – review & editing, Resources. **F. Munnik:** Writing – review & editing, Resources, Investigation, Formal analysis, Data curation. **J. Piot:** Resources, Project administration, Investigation, Data curation, Conceptualization. **L.E. Reed:** Writing – review & editing, Resources, Investigation, Formal analysis, Data curation, Conceptualization. **D. Renisch:** Writing – review & editing, Supervision, Project administration, Investigation, Funding acquisition, Data curation, Conceptualization. **H. Rothard:** Writing – review &

editing, Resources. **J. Runke**: Writing – review & editing, Methodology. **H. Savajols**: Software, Resources, Data curation, Conceptualization. **C. Stodel**: Resources, Project administration, Investigation, Formal analysis, Data curation, Conceptualization. **T. Madi**: Resources. **V. Urbanova**: Resources, Methodology, Investigation. **V. Watt-Morel**: Methodology. **A. Yakushev**: Methodology, Investigation.

Declaration of Generative AI and AI-assisted technologies in the writing process

During the preparation of this work the authors used [ChatGPT GPT-4o] in order to improve the readability and language. After using this tool, the authors reviewed and edited the content as needed and take full responsibility for the content of the published article.

Declaration of competing interest

The authors declare that they have no known competing financial interests or personal relationships that could have appeared to influence the work reported in this paper.

Acknowledgments

Our sincere thanks go to the mechanical workshop at the research reactor TRIGA Mainz for their local support and the financial support from the Helmholtz Institute Mainz. We acknowledge funding from the German Federal Ministry for Research and Education (project 05P21UMFN2). The results presented here are based on the experiment U327, which was performed at the beam line X8/TASCA at the GSI Helmholtzzentrum für Schwerionenforschung, Darmstadt (Germany) in the frame of FAIR Phase-0. The research leading to these results has received funding from the European Union's HORIZON EUROPE Program under grant agreement N° 101057511. We are grateful to the Ion Beam Center at Helmholtz-Zentrum Dresden-Rossendorf for their support in conducting the ion beam analysis of our samples. Some experiments were performed at the Grand Accélérateur National d'Ions Lourds (GANIL) by means of the CIRIL Interdisciplinary Platform, part of CIMAP laboratory, Caen, France. We thank the staff of CIMAP-CIRIL and GANIL for their invaluable support.

Data availability

Data will be made available on request.

References

- [1] O.R. Smits, Ch.E. Düllmann, P. Indelicato, W. Nazarewicz, P. Schwerdtfeger, The quest for superheavy elements and the limit of the periodic table, *Nat. Rev. Phys.* 6 (2) (2023) 86–98, <http://dx.doi.org/10.1038/s42254-023-00668-y>.
- [2] Y.Ts. Oganessian, Heaviest nuclei from ⁴⁸Ca-induced reactions, *J. Phys. G: Nucl. Part. Phys.* 34 (4) (2007) R165–R242, <http://dx.doi.org/10.1088/0954-3899/34/4/r01>.
- [3] Ch.E. Düllmann, et al., Advancements in the fabrication and characterization of actinide targets for superheavy element production, *J. Radioanal. Nucl. Chem.* 332 (5) (2023) 1505–1514, <http://dx.doi.org/10.1007/s10967-022-08631-4>.
- [4] E. Artes, Ch.E. Düllmann, C.-C. Meyer, D. Renisch, The process of molecular plating and the characteristics of the produced thin films – what we have learned in 60 years and what is still unknown, *EPJ Web Conf.* 285 (2023) 03001, <http://dx.doi.org/10.1051/epjconf/202328503001>.
- [5] W. Parker, R. Falk, Molecular plating: A method for the electrolytic formation of thin inorganic films, *Nucl. Instrum. Methods* 16 (1962) 355–357, [http://dx.doi.org/10.1016/0029-554x\(62\)90142-8](http://dx.doi.org/10.1016/0029-554x(62)90142-8).
- [6] A. Vascon, et al., Elucidation of constant current density molecular plating, *Nucl. Instrum. Methods Phys. Res. Sect. A* 696 (2012) 180–191, <http://dx.doi.org/10.1016/j.nima.2012.08.072>.
- [7] K. Eberhardt, et al., Preparation of targets for the gas-filled recoil separator TASCA by electrochemical deposition and design of the TASCA target wheel assembly, *Nucl. Instrum. Methods Phys. Res. Sect. A* 590 (1–3) (2008) 134–140, <http://dx.doi.org/10.1016/j.nima.2008.02.069>.
- [8] C.-C. Meyer, et al., Fabrication, swift heavy ion irradiation, and damage analysis of lanthanide targets, *Radiochim. Acta* 111 (11) (2023) 801–815, <http://dx.doi.org/10.1515/ract-2023-0197>.
- [9] M.E.M. Hamidi, J.-L. Pascal, Synthesis and structural characterization of some anhydrous Ln(OTf)₃ complexes (Ln=Sc, La, Nd, Sm, Gd and Er OTf=CF₃SO₃), *Polyhedron* 13 (11) (1994) 1787–1792, [http://dx.doi.org/10.1016/s0277-5387\(00\)80111-4](http://dx.doi.org/10.1016/s0277-5387(00)80111-4).
- [10] J. Runke, et al., Preparation of actinide targets for the synthesis of the heaviest elements, *J. Radioanal. Nucl. Chem.* 299 (2) (2013) 1081–1084, <http://dx.doi.org/10.1007/s10967-013-2616-6>.
- [11] E. Jäger, et al., High intensity target wheel at TASCA: target wheel control system and target monitoring, *J. Radioanal. Nucl. Chem.* 299 (2) (2013) 1073–1079, <http://dx.doi.org/10.1007/s10967-013-2645-1>.
- [12] C. Stodel, et al., High intensity targets stations for S3, *J. Radioanal. Nucl. Chem.* 305 (3) (2015) 761–767, <http://dx.doi.org/10.1007/s10967-015-3936-5>.
- [13] H. Rothard, CIRIL: Interdisciplinary research at GANIL, *Nucl. Phys. News* 32 (1) (2022) 29–33, <http://dx.doi.org/10.1080/10619127.2021.1990680>.
- [14] A. Gurbich, SigmaCalc recent development and present status of the evaluated cross-sections for IBA, *Nucl. Instrum. Methods Phys. Res. Sect. B* 371 (2016) 27–32, <http://dx.doi.org/10.1016/j.nimb.2015.09.035>.
- [15] N.P. Barradas, C. Jeynes, R.P. Webb, Simulated annealing analysis of Rutherford backscattering data, *Appl. Phys. Lett.* 71 (2) (1997) 291–293, <http://dx.doi.org/10.1063/1.119524>.
- [16] W.B. White, V.G. Keramidis, Vibrational spectra of oxides with the C-type rare earth oxide structure, *Spectrochim. Acta Part A* 28 (3) (1972) 501–509, [http://dx.doi.org/10.1016/0584-8539\(72\)80237-x](http://dx.doi.org/10.1016/0584-8539(72)80237-x).
- [17] R.L. Frost, et al., Effect of the lanthanide ionic radius on the Raman spectroscopy of lanthanide agardite minerals, *J. Raman Spectrosc.* 35 (11) (2004) 961–966, <http://dx.doi.org/10.1002/jrs.1243>.
- [18] R.L. Frost, A. López, R. Scholz, Y. Xi, F.M. Belotti, Infrared and Raman spectroscopic characterization of the carbonate mineral huanghoite – And in comparison with selected rare earth carbonates, *J. Mol. Struct.* 1051 (2013) 221–225, <http://dx.doi.org/10.1016/j.molstruc.2013.07.051>.
- [19] L. Spiridigliozzi, et al., An in-depth multi-technique characterization of rare earth carbonates Re₂(CO₃)₃·2H₂O owning tenerite-type structure, *J. Rare Earths* 40 (8) (2022) 1281–1290, <http://dx.doi.org/10.1016/j.jre.2021.09.020>.
- [20] R.L. Frost, M.J. Dickfos, Raman spectroscopy of halogen-containing carbonates, *J. Raman Spectrosc.* 38 (11) (2007) 1516–1522, <http://dx.doi.org/10.1002/jrs.1806>.
- [21] E.N. Silva, et al., Vibrational modes of rare-earth formates, *J. Raman Spectrosc.* 40 (8) (2009) 954–957, <http://dx.doi.org/10.1002/jrs.2207>.
- [22] V. Kartha, S. Venkateswaran, Vibrational spectra and normal vibrations of rare earth formates, *Spectrochim. Acta, Part A* 37 (11) (1981) 927–934, [http://dx.doi.org/10.1016/0584-8539\(81\)80017-7](http://dx.doi.org/10.1016/0584-8539(81)80017-7).
- [23] O.D. Saralidze, L.P. Shklover, K.I. Petrov, V.E. Plyushchev, Infrared absorption spectra of formates of the rare earth elements, *J. Struct. Chem.* 8 (1) (1967) 45–49, <http://dx.doi.org/10.1007/bf00741723>.
- [24] J. de Hosson, The infrared spectra of several rare-earth formates, *J. Inorg. Nucl. Chem.* 37 (11) (1975) 2350–2351, [http://dx.doi.org/10.1016/0022-1902\(75\)80753-6](http://dx.doi.org/10.1016/0022-1902(75)80753-6).
- [25] P.V. Klevtsov, R.F. Klevtsova, L.P. Sheina, Relationship between the infrared absorption spectra and crystal structure of the hydroxides of the rare earth elements and yttrium, *J. Struct. Chem.* 8 (2) (1967) 229–233, <http://dx.doi.org/10.1007/bf00745638>.
- [26] C.-C. Meyer, et al., Microscopic and spectroscopic analysis of ion-irradiated molecular-plated thin films for super-heavy element production, *Nucl. Instrum. Methods Phys. Res. Sect. A* (2024) accepted.
- [27] D. Mayorov, E. Tereshatov, T. Werke, M. Frey, C. Folden, Heavy-ion beam induced effects in enriched gadolinium target films prepared by molecular plating, *Nucl. Instrum. Methods Phys. Res. Sect. B* 407 (2017) 256–264, <http://dx.doi.org/10.1016/j.nimb.2017.07.012>.
- [28] J. Khuyagbaatar, et al., ⁴⁸Ca + ²⁴⁹Bk fusion reaction leading to element Z=117: Long-lived α-decaying ²⁷⁰Db and discovery of ²⁶⁶Lr, *Phys. Rev. Lett.* 112 (17) (2014) 172501, <http://dx.doi.org/10.1103/physrevlett.112.172501>.

Chapter 6

Conclusion and Outlook

This work involved further analysis of molecular plated thin films. A small review of the 60-year-old technique was written, to summarize what is known about the technique. Additionally, the influence of CO₂ and water was studied on the MP technique. Furthermore, the chemical changes within MP targets after the irradiation with an ion beam was studied.

To develop better targets a new electro deposition method, which utilizes aprotic, polar, organic solvents and inert anions for the lanthanide salts, was used and the chemical changes within the target layer after ion beam irradiation was studied.

First, the influence of CO₂ and water were studied to understand, why sometimes this technique seems to fail, without any obvious changes to previous successful attempts.

The study shows with γ -spectroscopy and SEM analysis, that water is necessary for the success of the production of thin films. Without additional water the yield is low. However, if the water concentration in the solution is above 1 vol-% the thin films start to become brittle and the adhesion of the target material to the backing decreases significantly. This is explained by the fact that molecular plating is a hydroxide precipitation. Due to the high voltages water is reduced to hydroxide and hydrogen. The lanthanides are precipitated and form hydroxide and oxidic layers. If the water content is too high, the hydrogen, which is formed hinders the hydroxides and oxides to form stable layers and therefore the molecular plating is not successful.

CO₂ does not contribute positively to the formation of the thin film. Due to the CO₂, high pH-value at the cathode and negative potential, carbonates and formates are formed and precipitated with the hydroxides and oxides. This is

shown by results of the Raman and infrared spectroscopy and are supported by the XPS-results. The carbonates and formates decrease the film quality due to increased number of different anions in the layer, decreasing potential crystallinity in the thin film.

The spectroscopic analysis of molecular plated thin films before the irradiation show, that no nitrogen is in the thin films, which shows, that no nitrates are in the thin films. Furthermore the spectroscopic analysis show the presence of carbonates and formates within the thin film. This is due the CO₂, which diffused into the solvent, before the plating.

PIXE and RBS studies show that the thin films loses carbon after irradiation. Most of the carbon is evaporated in form of CO₂. The remaining target material shrinks and the concentration of oxygen and lanthanide in the target material increases. Despite that, a small quantity of carbon still resides within the target layer after irradiation and form carbon clusters. These can be observed with Raman spectroscopy. This can be explained by the thermal spike model. It explains, that the temperature of targets rises instantaneously and falls of almost just as fast. Due to the high temperature, which remains for only a short time, carbonates and formates cannot be fully transformed into CO₂ and therefore forms also carbon clusters. The chemical changes in the thin films correlate with the sort and the energy of the ion-beam and the fluence on the target.

Lastly, similar studies were conducted with a different electro deposition technique. With the new technique targets with more than 1500 $\frac{\mu\text{g}}{\text{cm}^2}$. These targets show stability in ion beam irradiation with different ion beams and fluences at different institutes. The targets show similar chemical behaviour as molecular plated thin films. Formates and carbonates can be observed before irradiation and decreases after irradiation. The morphology changes similar to molecular plated thin films after irradiation. The tiles of of the mudcracking shrink, the amount of organic compounds in the film decreases and with that the concentration of the oxidic compositions increase.

This work shows, that organic compounds inside the produced thin films decrease the film quality. These organic compounds are produced, because CO₂ diffuses into the solvent. Other environmental aspects might influence the electro deposition technique as well and should be studied.

The electrodeposition from DMF and triflate salts, show promising results for the production of targets with a surface weight of 1500 $\frac{\mu\text{g}}{\text{cm}^2}$. These targets show promising results in ion-beam irradiation. The next steps should be first experiments with actinide materials like Americium instead of lanthanides.

List of Figures

1.1	Fusion cross sections of superheavy elements	3
1.2	The nuclide chart and the estimated position of the island of stability.	4
1.3	Different fusion reaction paths for SHE.	7
1.4	Schematic drawings of the molecular plating cells for different target shapes.	10
1.5	Typical mudcracking of molecular plated thin films.	10
1.6	Four Targets mounted together as a wheel for irradiation experiments at TASCAs.	12
1.7	The path of the ion beam through the target in TASCAs.	13
1.8	The path of the ion beam through the target in TASCAs.	15
1.9	Irradiation damage seen in SEM.	17
1.10	Alpha spectra before and after irradiation.	18
1.11	Principle of scanning electron microscopy.	24
1.12	Schematic illustration of a XPS spectrometer.	26

Acknowledgements

Ich möchte mich bei allen Bedanken, die mich im Laufe meines Studiums und meiner Promotion begleitet und unterstützt haben.

Ich möchte mich bei [REDACTED] für die Möglichkeit bedanken, sowohl meine Masterarbeit, als auch im Anschluss meine Doktorarbeit in seinem Arbeitskreis schreiben zu dürfen. Ich möchte mich für seine Unterstützung in während der gesamten Zeit bedanken. Aufgrund der COVID-19-Pandemie war es nicht immer einfach, dennoch hat er versucht sich die Zeit zu nehmen mir die nötige Aufmerksamkeit zu geben und im späteren Verlauf auch mir die Chance gegeben hat in den internationalen Austausch zu treten.

Weiter möchte ich speziell [REDACTED] meinen Dank aussprechen, der für viele wissenschaftlichen, technischen und organisatorischen Fragen eine Antwort hatte und auch in meiner Forschung ebenfalls unterstütz hat.

Es war mir eine Ehre die Arbeiten von [REDACTED] und [REDACTED] als Studentinnen betreuen zu dürfen.

Ebenfalls möchte ich mich bei [REDACTED] und [REDACTED] für die tolle Zusammenarbeit im Kernchemischen Praktikum bedanken. Ich möchte auch allen Kolleginnen und Kollegen für die tolle Zeit in der Kernchemie Mainz danken.

Besonderer Dank gilt allen Kolleginnen und Kollegen der Superheavies Gruppe sowohl in Mainz als auch an der GSI. Besonders möchte ich dabei [REDACTED] und [REDACTED] für die tolle Büroatmosphäre danken. [REDACTED]

[REDACTED] und [REDACTED] und [REDACTED] möchte ich ebenfalls für die tolle Zeit miteinander in der Gruppe danken. Die Zeit mit euch allen war geprägt von wissenschaftlichen Austausch, Freundschaften, und besonders Spaß. Die gemeinsamen Erfahrungen und Unternehmungen bleiben mir für immer in Erinnerung.

Ein besonderer Dank gilt [REDACTED], der meine Masterarbeit betreut hat und zu Beginn meiner Doktorarbeit ebenfalls zur Seite stand. Seine Arbeiten waren die Grundlage für meine Forschung.

Ich möchte mich auch bei allen Kooperationspartnern [REDACTED] vom Institut für Geowissenschaften in Mainz, [REDACTED] von der GSI Helmholtzzentrum für Schwerionenforschung, [REDACTED] vom Helmholtz-Zentrum Dresden-

Rosendorf, [REDACTED] vom Joint Research Center in Karlsruhe, [REDACTED] [REDACTED] und [REDACTED] in GANIL und [REDACTED] und [REDACTED] von der DECHEMA bedanken, die mir geholfen haben meine Forschung in diesem Maße umzusetzen.

Abschließend möchte ich mich bei allen meinen Freunden und meiner Familie bedanken, die mich all Zeit begleitet und bei allem erdenklichen unterstützt haben.

Ohne sie wäre das Studium und diese Arbeit nicht möglich gewesen.

Ich danke euch allen vom ganzen Herzen!

ERNST ARTES

Born on 13.09.1993 in Kostanay, Kazakhstan
Rudolf-Heilgers-Straße 59, 67549 Worms, Germany · +4915126790270
ernstartes@gmail.com



WORKING EXPERIENCE

MARCH 2025 – NOW

RADIATION PROTECTION ENGINEER, NUTEC GMBH, KRONBERG IM TAUNUS

IWRS-II planning for the decommissioning of the Biblis nuclear power plant for RWE Nuclear GmbH

SEPTEMBER 2020 – FEBRUARY 2025

SCIENTIFIC EMPLOYEE, JOHANNES GUTENBERG UNIVERSITY MAINZ, GERMANY

Scientific work to obtain a doctorate degree.

JULY 2020 – SEPTEMBER 2020

VACATION

Vacation time between achieving my master's degree and starting my position as a scientific employee to obtain my doctorate degree

SEPTEMBER 2019 – APRIL 2020

TUTOR FOR CHEMISTRY FOR PHYSICISTS AND GEOLOGISTS, JOHANNES GUTENBERG UNIVERSITY MAINZ, GERMANY

Part-time help for the corresponding lecture "chemistry for physicists and geologists"

SEPTEMBER 2016 – JUNE 2019

TUTOR FOR INORGANIC CHEMISTRY, JOHANNES GUTENBERG UNIVERSITY MAINZ, GERMANY

Part-time for the corresponding lecture "inorganic chemistry 2"

MARCH 2013 – SEPTEMBER 2013

ORIENTATION PHASE

Vacation time between achieving higher qualification for university entrance and attending university

EDUCATION

SEPTEMBER 2020 - TODAY

DOCTORATE DEGREE, JOHANNES GUTENBERG UNIVERSITY MAINZ, GERMANY

Doctorate thesis (working title): Optimierung elektrochemischer Verfahren für die Herstellung von f-Element Dünnschichten für kernchemische Anwendungen

SEPTEMBER 2017 - JULY 2020

MASTER OF SCIENCE IN CHEMISTRY, JOHANNES GUTENBERG UNIVERSITY
MAINZ, GERMANY

cumulative grade: 1.8

Master thesis: Herstellung von f-Element-Targets mit hohen Flächengewichten

thesis grade: **2.1**

SEPTEMBER 2013 - JANUARY 2018

BACHELOR OF SCIENCE IN CHEMISTRY, JOHANNES GUTENBERG UNIVERSITY
MAINZ, GERMANY

cumulative grade: 2.3

Bachelor thesis: Darstellung und Charakterisierung von Kohlenstoffnanopartikel

thesis grade: **1.7**

MARCH 2013

GENERAL HIGHER QUALIFICATION FOR UNIVERSITY ENTRANCE, ELEONOREN-
GYMNASIUM WORMS, GERMANY

QUALIFICATION

- Different inorganic synthesis methods
- Various spectroscopic methods (Raman, IR, XPS, XRD, Gamma, Alpha)
- Radiation protection planning (IWRS-II)
- Basic knowledge in electro chemistry
- Basic knowledge of ion beam experiments
- Handling open radioactive substances
- Fachkundeschein S4.2
- Experiences in project management
- MS Office knowledge
- Teaching experience
- Driver's license (B)

LANGUAGES

GERMAN, MOTHER TONGUE

ENGLISH, FLUENT (B2)

RUSSIAN, A1

SCIENTIFIC ACHIEVEMENTS

JULY 2025

PUBLICATION, RADIOCHIMICA ACTA

"Influence of carbon dioxide and water concentration on terbium thin films produced by Molecular Plating"

MARCH 2025

PUBLICATION, NULCEAR INSTR. AND METHODS IN PHYSICS REASEARCH, A

"Preparation of lanthanide thin films for ion beam experiments and post irradiation characterization"

FEBRUARY 2025

PUBLICATION, NULCEAR INSTR. AND METHODS IN PHYSICS REASEARCH, A

“Microscopic and spectroscopic analysis of ion-irradiated molecular-plated thin films for superheavy element production”

AUGUST 2024

CONFERENCE TALK, 31ST CONFERENCE OF THE INTERNATIONAL TARGET DEVELOPMENT SOCIETY (INTDS2024)

“Development of actinide targets for superheavy element production and assessment of their performance in intense heavy-ion beams”

DECEMBER 2023

WORKSHOP TALK, SANDA WORKSHOP

“Mainz actinide target production methods for applications in chemistry and physics”

NOVEMBER 2022

PUBLICATION, RADIOCHIMICA ACTA

“Fabrication, swift heavy ion irradiation, and damage analysis of lanthanide targets”

JUNE 2023

PUBLICATION, EPJ WEB OF CONFERENCES

“The process of molecular plating and the characteristics of the produced thin films – What we have learned in 60 years and what is still unknown”

JUNE 2023

CONFERENCE TALK, ACTINIDES CONFERENCE 2023

“Development of actinide targets for superheavy element production and assessment of their performance in intense heavy-ion beams”

MAY 2023

POSTER PRESENTATION, 3RD INTERNATIONAL CONFERENCE ON RADIOANALYTICAL AND NUCLEAR CHEMISTRY (RANC2023)

“The influence of water and carbon dioxide on terbium thin films produced by molecular plating”

DECEMBER 2022

WORKSHOP TALK, GANIL WORKSHOP

“Development of actinide targets for superheavy element production and assessment of their performance in intense heavy-ion beams”

NOVEMBER 2022

PUBLICATION, JOURNAL OF RADIOANALYTICAL AND NUCLEAR CHEMISTRY

“Advancements in the fabrication and characterization of actinide targets for superheavy element production”

SEPTEMBER 2022

CONFERENCE TALK, 30TH CONFERENCE OF THE INTERNATIONAL TARGET DEVELOPMENT SOCIETY (INTDS2022)

“The influence of water and carbon dioxide on lanthanide thin films produced by molecular plating”